UNICAMP

UNIVERSIDADE ESTADUAL DE CAMPINAS
Faculdade de Engenharia Mecânica

VINICIUS ERLER DE SOUSA RAMOS

Analysis of thermoelastic problems of anisotropic material using the Boundary Element Method

Análise de problemas termoelásticos em materiais anisotrópicos utilizando o Método dos Elementos de Contorno

Campinas

2023

VINICIUS ERLER DE SOUSA RAMOS

Analysis of thermoelastic problems of anisotropic material using the Boundary Element Method

Análise de problemas termoelásticos em materiais anisotrópicos utilizando o Método dos Elementos de Contorno

Tese de Doutorado apresentada à Faculdade de Engenharia Mecânica da Universidade Estadual de Campinas como parte dos requisitos exigidos para a obtenção do título de Doutor em Engenharia Mecânica, na Área de Mecânica dos Sólidos e Projeto Mecânico.

Thesis presented to the Faculty of Mechanical Engineering of the University of Campinas in partial fulfillment of the requirements for the degree of Doctor, in the area of Solid Mechanics and Mechanical Design.

Orientador: Prof. Dr. Paulo Sollero

Coorientador: Prof. Dr. Eder Lima de Albuquerque

ESTE TRABALHO CORRESPONDE À VERSÃO FINAL DA TESE DE DOUTORADO DEFENDIDA PELO ALUNO VINICIUS ERLER DE SOUSA RAMOS, E ORIENTADA PELO PROF. DR. PAULO SOLLERO.

Campinas

2023

Ficha catalográfica
Universidade Estadual de Campinas
Biblioteca da Área de Engenharia e Arquitetura
Rose Meire da Silva - CRB 8/5974

R147a

Ramos, Vinicius Erler de Sousa, 1986-
Analysis of thermoelastic problems of anisotropic material using the boundary element method / Vinicius Erler de Sousa Ramos. – Campinas, SP : [s.n.], 2023.

Orientador: Paulo Sollero.
Coorientador: Eder Lima de Albuquerque.
Tese (doutorado) – Universidade Estadual de Campinas, Faculdade de Engenharia Mecânica.

1. Termoelasticidade. 2. Método de elementos de contorno. 3. Tensões térmicas. 4. Anisotropia. I. Sollero, Paulo, 1950-. II. Albuquerque, Eder Lima de, 1972-. III. Universidade Estadual de Campinas. Faculdade de Engenharia Mecânica. IV. Título.

Informações Complementares

Título em outro idioma: Análise de problemas termoelásticos em materiais anisotrópicos utilizando o método dos elementos de contorno
Palavras-chave em inglês:
Thermoelasticity
Boundary element method
Thermal stresses
Anisotropy
Área de concentração: Mecânica dos Sólidos e Projeto Mecânico
Titulação: Doutor em Engenharia Mecânica
Banca examinadora:
Eder Lima de Albuquerque [Coorientador]
Andres Felipe Galvis Rodriguez
Carlos Friedrich Loeffler Neto
Josué Labaki Silva
Renato Pavanello
Data de defesa: 30-11-2023
Programa de Pós-Graduação: Engenharia Mecânica

Identificação e informações acadêmicas do(a) aluno(a)
- ORCID do autor: https://orcid.org/0000-0002-4560-7469
- Currículo Lattes do autor: http://lattes.cnpq.br/0388241038154975

UNIVERSIDADE ESTADUAL DE CAMPINAS
FACULDADE DE ENGENHARIA MECÂNICA

TESE DE DOUTORADO

Analysis of thermoelastic problems of anisotropic material using the Boundary Element Method

Análise de problemas termoelásticos em materiais anisotrópicos utilizando o Método dos Elementos de Contorno

Autor: Vinicius Erler de Sousa Ramos

Orientador: Prof. Dr. Paulo Sollero
Coorientador: Prof. Dr. Eder Lima de Albuquerque

A Banca Examinadora composta pelos membros abaixo aprovou esta Tese de Doutorado:

Prof. Dr. Eder Lima de Albuquerque
DEM/UnB/Brasília, Presidente

Prof. Dr. Andres Felipe Galvis Rodriguez
School of Mechanical and Design Engineering/University of Portsmouth

Prof. Dr. Carlos Friedrich Loeffler Neto
DEM/UFES

Prof. Dr. Josué Labaki Silva
DMC/FEM/Unicamp

Prof. Dr. Renato Pavanello
DMC/FEM/Unicamp

A Ata de Defesa com as respectivas assinaturas dos membros encontra-se no SIGA/Sistema de Fluxo de Dissertação/Tese e na Secretaria do Programa da Unidade.

Campinas, 30 de Novembro de 2023

DEDICATION

This thesis is dedicated to my parents José Luiz de Sousa and Ozélia de Lurdes Erler de Sousa who always dedicated themselves to educating me to life; to my beloved wife Leilane Silva da Vitória who supported the distance and my absence; to my friend Luciane Freitas da Silva (*in memorian*) which example of perseverance inspired me in many difficulties moments; to Celina de Paula Azevedo Sollero (*in memorian*) who will always be in our hearts.

Esta tese é dedicada aos meus pais José Luiz de Sousa e Ozélia de Lurdes Erler de Sousa que sempre se dedicaram a me educar para a vida; à minha esposa Leilane Silva da Vitória que suportou a distância e minha ausência; à minha amiga Luciane Freitas da Silva (*in memorian*) cujo exemplo de perseverança me inspirou em muitos momentos de dificuldades; à Celina de Paula Azevedo Sollero (*in memorian*) que sempre estará em nossos corações.

ACKNOWLEDGEMENTS

This work would never exist if it weren't for the many heads and hands contributions. The author recognizes it and is very grateful to:

- Prof. Dr. Paulo Sollero for accepting me to develop this thesis. Your few words always provoked great meditation and adjustments in my actions;
- Prof. Dr. Eder Lima de Albuquerque, whose technical assistance enlightened the path to follow;
- my colleagues of IFES campus Vitória, who released me from my daily activities to have full dedication to this thesis;
- Amadeus and Caio Moura, the laboratory friends that, apart from distance, were always ready to help and hear my lamentations, and also ready to share some funny moments;
- Caio Rocha, whose notes on BESLE were essential tools for me to understand BESLE code;
- Prof. Andres Galvis, who never stepped aside every time I asked some question on the BESLE code;
- my volleyball friends, for inviting me to train and matches, being my mental relief;
- Nunes, the mechanical who always took great care of my Fusca, releasing me time to focus on studies;

This study was financed in part by the Coordenação de Aperfeiçoamento de Pessoal de Nível Superior – Brazil (CAPES) – Finance Code 001.

The Air Force Office of Scientific Research (AFOSR) of the United States has supported this study through the acquisition of hardware (FA9550-18-1-0113 and FA9550-20-1-0133) available at Unicamp.

If I saw so far, it was because I was standing on giant's shoulders.
If I came this far, it's because I followed the steps of those who came before.
(BEM Group - On the giant's shoulders - *free translation*)
Se eu vi tão longe, foi porque estava apoiado em ombros de gigantes.
Se eu vim tão longe, foi porque segui os passos de quem veio antes.
(Grupo BEM - Sobre ombros de gigantes)

RESUMO

Este trabalho apresenta uma formulação de termoelasticidade do Método dos Elementos de Contorno (MEC) aplicável a materiais isotrópicos e anisotrópicos em problemas tridimensionais. A solução fundamental do problema de elasticidade utiliza o tensor de Barnett-Lothe representado por série Dupla de Fourier, permitindo generalidade de aplicação no que concerne ao tipo de material elástico. A formulação termoelástica introduz uma integral de domínio na Equação Integral de Contorno (EIC) do problema de elasticidade que é resolvida utilizando o Método da Dupla Reciprocidade (MDR), de modo que apenas o campo de temperaturas é necessário, dispensando o uso dos valores de derivadas do problema de potencial, especialmente no domínio. Considerações sobre o uso de pontos internos e subregiões para melhorar a interpolação de temperaturas pelo MDR são apresentadas por meio da solução de alguns exemplos, bem como o efeito de diferentes funções de base radial empregadas no MDR. Rotinas de solução do campo de temperaturas para materiais iso e anisotrópicos são apresentadas bem como adaptações para a solução de problemas bidimensionais em formulação tridimensional. O cálculo de tensões e deformações no contorno é feito pelo uso das funções de forma e dos valores dos deslocamentos e *tractions* dos nós. Os resultados demonstram que o bom funcionamento pode exigir o uso de pontos internos em alguns casos e que a precisão deles pode ser menor quando são utilizadas subregiões.

Palavras–chave: Termoelasticidade, Método dos Elementos de Contorno, Método da Dupla Reciprocidade, Anisotropia.

ABSTRACT

This work presents a thermoelasticity formulation of the Boundary Element Method (BEM) applicable to isotropic and anisotropic materials in three-dimensional problems. The fundamental solution of the elasticity problem uses the Barnett-Lothe tensor represented by the Double Fourier series, allowing generality of application concerning the type of elastic material. The thermoelastic formulation introduces a domain integral in the Boundary Integral Equation (BIE) of the elasticity problem which is solved using the Dual Reciprocity Method (DRM), so that only the temperature field is necessary, dismissing the use of derivative values of the potential problem, especially inside the domain. Considerations on the use of internal points and subregions to improve temperature interpolation by DRM are presented by solving some examples, as well as the effect of different radial basis functions used by DRM. Temperature field solution routines for iso- and anisotropic materials are presented as well as adaptations for solving two-dimensional problems in three-dimensional formulation. The calculation of stresses and deformations at the boundary uses the shape functions and the values of the displacements and tractions of the nodes. The results demonstrate that proper functioning may require the use of internal points in some cases and that the accuracy may be lower when subregions are used.

Keywords: Thermoelasticity, Boundary Element Method, Dual Reciprocity Method, Anisotropy.

LIST OF FIGURES

LIST OF TABLES

CONTENTS

1 INTRODUCTION

1.1 Overview

The Boundary Elements Method (BEM) is an attractive technique to solve boundary value problems since it is only necessary to discretize the boundary, reducing the dimensionality of the problem by one, making the mesh generation problem easier than the domain methods (Brebbia; Dominguez, 1992). This also makes BEM very suitable to solve problems of infinite or semi-infinite domains, like acoustic problems, and those with moving boundaries, like fracture propagation (Gaul *et al.*, 2003).

Boundary Elements make use of the fundamental solution which consists of an analytical solution of a pontual action in an infinite domain concerning the governing equation, improving the accuracy of the method, especially at problems with high gradients like stress concentration. BEM also calculates the variable solution together with its derivative being particularly strong on the accuracy of the second one (Katsikadelis, 2002).

If a problem does not have a fundamental solution, interpolation methods are used to approximate it which can reduce the accuracy of the BEM. The singular nature of the fundamental solutions requires special formulations for thin geometries, like plates and shell theories (Aliabadi, 2002).

The matrices generated by FEM are banded and symmetrical allowing it to take advantage of optimized linear system solvers, while BEM matrices are fully populated and non-symmetrical. To overcome this drawback, techniques like Adaptative Cross Approximation (Bebendorf, 2000) and Fast Multipole (Liu, 2009) were developed to reduce the size of the linear system generated by BEM. Another strategy consists of speeding up the calculations by using parallelization with distributed memory, allowing the code to be used at supercomputers, by means of the Message Passage Interface (MPI).

Fundamental solutions for isotropic 2D and 3D elasticity problems are simple and well established and can be found in many books, for example in Kane (1994). Different formulations were developed for anisotropic materials. Concerning bidimensional domains, Rizzo and Shippy (1970) developed a fundamental solution based on Green (1943) using real variables while Cruse and Swedlow (1971) used complex variables. Green and Zerna (1968) presented Airy's stress functions, and Dumir and Mehta (1987) used them to develop another fundamental solution. Airy's functions combined with Lekhnitskii (1963) formalism generates a complex fundamental solution used by Sollero and Aliabadi (1993) to analyze fracture mechanics of anisotropic plates.

Vogel and Rizzo (1973) were the first to present a fully anisotropic fundamental solution for tridimensional domains and Wilson and Cruse (1978) optimized it using interpolation and storing some calculated matrices in this procedure to be reused. But this solution is not in a closed form like isotropic expressions, being expressed by means of an integral to be solved, which is very time-consuming. This has driven researchers to develop many different solutions, some of them limited to particular cases. For example, Pan and Chou (1976) presented a closed form to transversely isotropic materials that was expanded by Pan and Amadei (1995) to conditions of transverse isotropy at any direction. Loloi (2000) revised the formulation on Pan and Chou (1976) to adjust bad conditioning that could happen to some points at integration, and Noritomi (2005) applied it to analyze superficial bone remodeling.

To avoid integration of Vogel and Rizzo (1973) solution for fully anisotropic materials, Brebbia and Dominguez (1992) proposed but did not implement the use of the isotropic fundamental solution with an iterative procedure to solve the displacements, and Schclar and Partridge (1993) used the DRM to solve the derivatives of displacements with no need of iteration procedure.

Based on a residue calculation, Sales and Gray (1998) proposed a technique that proved to be faster than Wilson and Cruse (1978) but had instabilities solved by Phan *et al.* (2004) adjustments. Another procedure based on residue and integral representation was proposed by Wang (1997) and implemented by Tonon *et al.* (2001), but the derivatives are difficult to obtain, and degenerated cases need to be treated carefully.

Gaul *et al.* (2003) presented a fundamental solution developed using Radon transformation that was used by Cravo (2008) to develop a multi-region analysis, and by Souza (2009) on bonded joints of composite material. Wang and Denda (2007) also used Radon transform but first expressed Green's functions as a line integral over a semicircle, allowing analytical integration.

An explicit form of displacements fundamental solution was presented by Ting and Lee (1997), in terms of Stroh's eigenvalues. Its derivatives were obtained by Lee (2003) and Lee (2009), but Shiah *et al.* (2010) showed explicit expressions for them, while Shiah *et al.* (2008) calculated the Stroh's eigenvalues using real coefficients, avoiding the complex values.

The solution of Ting and Lee (1997) was implemented for transversely isotropic materials by Távara *et al.* (2007) and for full anisotropy by Tan *et al.* (2009). However, this solution needs considerable programming efforts overcome by Shiah *et al.* (2012) proposal, who approximated the Stroh's eigenvalues by double Fourier series. This proposal was revised by Tan *et al.* (2013) to reduce the terms and to become numerically more efficient. Moreover, the derivatives can be easily obtained since it is expressed in terms of the double Fourier series. Another advantage is that the terms of the Fourier series depend only on the material, so they are calculated only once. Galvis *et al.* (2021) implemented the formulation adjusted by Tan *et al.* (2013) and built a parallel open-source Fortran code using Message Passage Interface (MPI) for 3D elastostatic and elastodynamic problems, named BESLE. It can deal with heterogeneous materials employing subregions divisions, iso- or anisotropic, since the formulation of this fundamental solution does not degenerate for the various symmetries.

In engineering, the specimens are subjected to temperature variation inducing dilation that may cause considerable stresses and strains. Most machines generate heat when working like automotive engines, airplane turbines, electronic chips, and electrical engines. Other materials are cooled, like aircraft fuselage, 3D printed parts, and tempered steel. In these cases, the state of stress and strains can only be accurately calculated by thermoelasticity formulation. For the general case, equations related to thermal and displacement fields are coupled and need to be solved together. Some simplifications may apply depending on the problem conditions, and for the simplest cases, the elastic displacements do not affect the thermal field. Then, the temperature field can be calculated first and its effect is added to the elastic governing equation which is solved next. The type of problems that can be solved in this way are the stationary thermoelasticity and the uncoupled quasi-static thermoelasticity (UQT) (Gaul *et al.*, 2003).

The first 3D work to analyze thermoelastic problems with Boundary Elements is credited to Rizzo and Shippy (1977) who showed that the thermal effects appear at Somigliana's boundary identity as a volume integral and can be interpreted as a body force. In their work, known functions for temperature distributions with their Laplacian being a constant value were used. So, the volume integrals were easily transformed into surface integrals. Henry and Banerjee (1988) used the particular integrals technique to evaluate the domain integral, although they also used only known distribution temperature. Deb and Henry (1991) extended this technique and calculated stresses using a multi-region approach.

The DRM was used by Matsumoto *et al.* (2005) to analyze isotropic material with properties varying with temperature. A few years before, Gaul *et al.* (2003) used DRM as a general technique able to solve coupled and uncoupled thermoelasticity cases, for iso- or anisotropic materials. Alternatively, Gao (2003) solved stationary thermoelasticity using the Radial Integration Method (RIM), applying the formulation to isotropic materials and temperature fields described by known functions.

Using a transverse isotropic material, Shiah and Tan (2012) proposed an analytical transformation of the volume integral using the Direct Domain Mapping (DDM) technique developed by themselves (Shiah; Tan, 2004), but a numerical procedure is necessary to evaluate additional terms used in this formulation. Shiah and Tan (2014) extended this technique to general anisotropic elasticity using the fundamental solution expressed by double Fourier series of Tan *et al.* (2013) , although they only presented the evaluation of the domain integral. The expressions for stresses at points inside the boundary would appear later, (Shiah; Tan, 2016a) as well as an application of this procedure to an anisotropic thermoelastic problem with variable temperature (Shiah; Tan, 2016b).

Another UQT application using BEM was done by Ubero-Martínez *et al.* (2022) on studying an orthotropic friction condition considering a non-linear thermal interface and the frictional thermal effects, but the bodies in contact are isotropic.

The use of the anisotropic elasticity fundamental solution with double Fourier series on thermoelasticity is still a problem to be exploited. This thesis uses it together with the Dual Reciprocity Method to solve the thermal body force, investigating the behavior of the solutions at isotropic and anisotropic problems under different conditions.

1.2 Objectives

The main objective of this thesis is to use the Boundary Element Method to solve uncoupled thermoelasticity problems by means of the general elasticity anisotropy functions expressed in terms of a double Fourier series, along with the Dual Reciprocity Method to compute the volume integral of thermals effects. The fundamental solution is already implemented at BESLE, then, adding the thermoelasticity formulation with modules at the BESLE code will also increase the capacities of this free and open-source software available to the scientific community. Secondary objectives are listed:

- Evaluation of thermoelastic stresses and strains as a secondary response, based on displacements and tractions results, using the element shape functions;

- Implementation of a generic potential Boundary Element solver in BESLE for isotropic and anisotropic materials to compute the temperature field as input for the thermoelastic problem, as well as a tool to enter a known function for the potential field;
- Investigate the performance of different particular solutions on thermal field interpolation for DRM in an attempt to find a function that can be reliable to be used for all problems.

1.3 Thesis organization

Chapter One presented the most relevant advancements concerning anisotropic fundamental solutions applied to the Boundary Element Method, along with some formulations developed for thermoelasticity problems.

Chapter Two presents the thermoelasticity formulation to general anisotropic material, the elasticity fundamental solution used, the discretization used by BESLE, the Dual Reciprocity Method formulation to solve domain integral generated by thermoelasticity, the Radial Basis Functions used, and the calculations of boundary stresses and strains using the shape functions and the primary response (displacements and tractions).

Chapter Three shows the formulation of the BEM for potential problems and the Direct Domain Mapping technique applied to anisotropic potential problems.

Chapter Four is reserved for the numerical tests, with validation and convergence tests, variation of interpolation functions for temperature, and division of problems into subregions.

The final Chapter Five presents the conclusions based on the results obtained in Chapter Four, as well as proposals for future works.

2 THERMOELASTIC BOUNDARY ELEMENT METHOD

2.1 Thermoelastic Boundary Integral Equation

The Hooke's law considering the thermal effects (Equation 2.1) and equilibrium equation (Equation 2.2) may be written as (Gaul *et al.*, 2003):

$$\sigma_{ij} = C_{ijkl}\epsilon_{kl} - \gamma_{ij}\theta \tag{2.1}$$

$$\sigma_{ji,j} + \rho b_i = 0 \tag{2.2}$$

Repeated subscripts mean summation. Equation 2.1 is valid for isotropic and anisotropic material and two or three-dimensional problems. In these Equations, C_{ijkl} is the material elasticity tensor, γ_{ij} is the thermoelastic tensor given by the product of elasticity tensor and thermal expansion tensor α_{ij}, θ is the temperature difference of temperature analysis T and reference temperature T_0, σ_{ij} are the stresses, ϵ_{kl} are the strains, ρ is the density of the body and b_i is the body force. In mathematical language:

$$\gamma_{ij} = C_{ijkl}\alpha_{kl} \tag{2.3}$$

$$\theta = T - T_0 \tag{2.4}$$

From elasticity:

$$\epsilon_{kl} = \frac{1}{2}\left(u_{k,l} + u_{l,k}\right) \tag{2.5}$$

Applying Equations 2.5 and 2.1 into 2.2:

$$C_{ijkl}u_{k,lj} = \gamma_{ij}\theta_{,j} - \rho b_i \tag{2.6}$$

A differential operator is defined as:

$$\mathcal{L}_{ik} = C_{ijkl}\frac{\partial^2}{\partial x_l \partial x_j} \tag{2.7}$$

It can be used to rewrite Equation 2.6, to obtain:

$$\mathcal{L}_{ik}u_k = f_i^{el} \tag{2.8}$$

where

$$f_i^{el} = -\rho b_i + \gamma_{ij}\theta_{,j} \tag{2.9}$$

Using an interpolation function u^*_{mi}, commonly known in BEM as the fundamental solution, and integrating over the domain, Equation 2.8 can be written as:

$$\int_\Omega \left(\mathcal{L}_{ik} u_k - f^{el}_i\right) u^*_{mi} d\Omega = 0 \tag{2.10}$$

To obtain an inverse statement, the last equation is integrated by parts followed by the application of the Betti's reciprocal theorem. This sequence is well detailed in books (Gaul *et al.*, 2003; Brebbia; Dominguez, 1992; Banerjee, 1994), where one obtains:

$$\int_\Gamma C_{ijkl} u^*_{mi} u_{k,l} n_j d\Gamma - \int_\Gamma C_{ijkl} u^*_{mi,j} n_l u_k d\Gamma + \int_\Omega C_{ijkl} u_k u^*_{mi,jl} d\Omega = \int_\Omega f^{el}_i u^*_{mi} d\Omega \tag{2.11}$$

Some definitions can be applied to the previous Equation. First, tractions at the boundary are given by:

$$t_i = \sigma_{ij} n_j = C_{ijkl} u_{k,l} n_j - \gamma_{ij} \theta n_j \tag{2.12}$$

which can be rearranged as:

$$C_{ijkl} u_{k,l} n_j = t_i + \gamma_{ij} \theta n_j \tag{2.13}$$

Similar consideration can be done for derivatives of fundamental solution (subscript k is changed with i for convenience, without loss of formality, given the symmetry of the C_{ijkl} tensor):

$$C_{ijkl} u^*_{mi,j} n_l = C_{ijkl} u^*_{mk,j} n_l = t^*_{mi} \tag{2.14}$$

As the fundamental solution is the effect of a pontual action at a source point, it can be written as:

$$C_{ijkl} u^*_{mi,jl} = \mathcal{L}_{ik} u^*_{mk} = -\delta_{mi} D(\xi, x) \tag{2.15}$$

where δ_{mi} means the Kronecker delta, $D(\xi, x)$ is the Dirac delta, ξ is the source point and x is any point in the domain problem. So, the domain integral on the left-hand side of Equation 2.11 can be evaluated under the sense of Cauchy Principal Value, resulting in:

$$\int_\Omega C_{ijkl} u_k u^*_{mi,jl} d\Omega = \int_\Omega -\delta_{mi} D(\xi, x) u_k d\Omega = -\delta_{mi} c(\xi) u_i(\xi) \tag{2.16}$$

with $c(\xi) = 0.5$ for source points at smooth boundary and $c(\xi) = 1.0$ for points inside the domain. Combining Equations 2.16, 2.14 and 2.13 into 2.11, the Boundary Integral Equation for stationary thermoelasticity comes out:

$$\delta_{mi} c(\xi) u_i(\xi) + \int_\Gamma t^*_{mi} u_i d\Gamma = \int_\Gamma u^*_{mi} t_i d\Gamma + \int_\Gamma u^*_{mi} \gamma_{ij} n_j \theta d\Gamma - \int_\Omega f^{el}_i u^*_{mi} d\Omega \tag{2.17}$$

The left-hand side of Equation 2.17 plus the first integral on its right-hand side compose the BIE of elasticity problems in the absence of body forces. The second boundary integral on the right side is a coupling term of thermal effects over displacements, easily solved by BEM since it is a boundary integral.

The domain integral has the term f_i^{el}, which contains body forces from elasticity and temperature gradient effect. Many techniques involving domain integrals were developed to avoid solving it by discretizing the domain. When the Laplacian of domain actions is null, the Galerkin Vector Approach may be applied (Partridge *et al.*, 1992), but it can be quite a complicated expression depending on the fundamental solution used since it is integrated twice. The Radial Integration Method (RIM) (Gao, 2002; Gao, 2003) is quite interesting when the temperature field can be expressed as a function of spatial coordinates, with a more general application than the Galerkin Vector. However, if the temperature field is unknown, it will have to be interpolated, increasing the complexity of RIM. The Dual Reciprocity Method (Partridge *et al.*, 1992) or the Direct Integration Method (Loeffler *et al.*, 2015) are considered general techniques since they approximate any kernel of the integration using the Radial Basis Functions (RBF). Considering the possibility of generalizing the application on different problems and that DRM is already implemented in BESLE, DRM was chosen for this work.

2.2 Elasticity Fundamental Solution

Different fundamental solutions for anisotropic medium were developed for BEM, especially the ones based on the analytical evaluation of u_{mi}^* by Lifshitz and Rozenzweig (1947). It uses the Barnett-Lothe tensor $\boldsymbol{H}[\boldsymbol{x}]$ shown in Equation 2.18, which depends only on the spherical coordinates and can deal with degenerated cases (works for isotropic and any anisotropic material). Later, it allowed the fundamental solution to be explicitly expressed in a full algebraic expression (Ting; Lee, 1997).

$$\boldsymbol{U}(\boldsymbol{x}) = \frac{1}{4\pi r}\boldsymbol{H}[\boldsymbol{x}] \tag{2.18}$$

where $\boldsymbol{U}(\boldsymbol{x})$ is the fundamental solution u_{mi}^* written on a tensor form. The computer code uses the fundamental solution as proposed by Tan *et al.* (2013), representing $\boldsymbol{U}(\boldsymbol{x})$ by Double Fourier series which can be directly differentiated to obtain the derivative of the fundamental solution. Equation 2.18 can be rewritten in terms of a spherical coordinate system as:

$$\boldsymbol{U}(r,\theta,\phi) = \frac{1}{4\pi r}\boldsymbol{H}(\theta,\phi) \tag{2.19}$$

where r is the cartesian distance from source point ξ and field point $\boldsymbol{x}$, while spherical coordinates are shown in Figure 2.1. A unit vector $\boldsymbol{n}^* = \boldsymbol{x}/r$ and two tangent vectors $\boldsymbol{n}$ and $\boldsymbol{m}$ form a right-hand triad $[\boldsymbol{n}, \boldsymbol{m}, \boldsymbol{n}^*]$, expressed by:

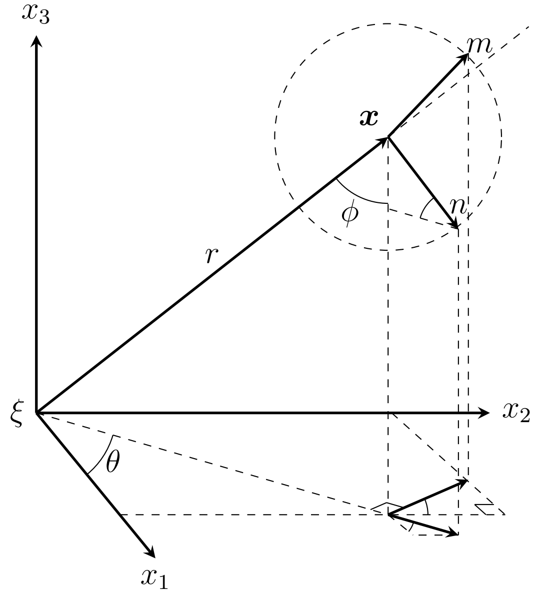

Figure 2.1 – The unit circle on an oblique plane at the field point.

$$\boldsymbol{n} = (\cos\phi\cos\theta, \cos\phi\sin\theta, -\sin\phi) \tag{2.20}$$

$$\boldsymbol{m} = (-\sin\theta, \cos\theta, 0) \tag{2.21}$$

$$\boldsymbol{n}^* = \boldsymbol{x}/r \tag{2.22}$$

with $0 \leq \theta < 2\pi$ and $0 \leq \phi \leq \pi$. First, it is necessary to write down the Barnett-Lothe tensor as done by Ting and Lee (1997):

$$\boldsymbol{H}(\theta, \phi) = \frac{1}{|\boldsymbol{\kappa}|} \sum_{n=0}^{4} q_n \hat{\boldsymbol{\Gamma}}^{(n)} \tag{2.23}$$

where q_n is calculated through Equations 2.24 and 2.25. It is given in terms of Stroh's eigenvalues which are three pairs of complex conjugates $p_t = \alpha_t + \mathbf{i}\beta_t$, with $t = 1, 2, 3$, $\bar{p}_t$ meaning the conjugate eigenvalue, $\beta_t > 0$ and $\mathbf{i} = \sqrt{-1}$. For $n = 0, 1, 2$:

$$q_n = \frac{-1}{2\beta_1\beta_2\beta_3} \left[\mathbf{Re} \left\{ \sum_{t=1}^{3} \frac{p_t^n}{(p_t - \bar{p}_{t+1})(p_t - \bar{p}_{t+2})} \right\} - \delta_{n2} \right] \tag{2.24}$$

and for $n = 3, 4$:

$$q_n = \frac{-1}{2\beta_1\beta_2\beta_3} \left[\mathbf{Re} \left\{ \sum_{t=1}^{3} \frac{p_t^{n-2}\bar{p}_{t+1}\bar{p}_{t+2}}{(p_t - \bar{p}_{t+1})(p_t - \bar{p}_{t+2})} \right\} \right] \tag{2.25}$$

Tensor $\hat{\mathbf{\Gamma}}^{(n)}$, with $(i, j = 1, 2, 3)$, is given by:

$$\hat{\Gamma}_{ij}^{(n)} = \tilde{\Gamma}_{(i+1)(j+1)(i+2)(j+2)}^{(n)} - \tilde{\Gamma}_{(i+1)(j+2)(i+2)(j+1)}^{(n)} \tag{2.26}$$

The adjoint of matrix $\mathbf{\Gamma}(p)$ is defined as:

$$\mathbf{\Gamma}(p) = \boldsymbol{Q} + p\boldsymbol{V} + p^2\boldsymbol{\kappa} \tag{2.27}$$

with

$$\boldsymbol{V} = (\boldsymbol{R} + \boldsymbol{R}^T) \tag{2.28}$$

and

$$\boldsymbol{\kappa} = \kappa_{ik} = C_{ijkl} m_j m_l \tag{2.29}$$

$$\boldsymbol{Q} = Q_{ik} = C_{ijkl} n_j n_l \tag{2.30}$$

$$\boldsymbol{R} = R_{ik} = C_{ijkl} n_j m_l \tag{2.31}$$

The eigenvalues p_t are calculated by making $|\mathbf{\Gamma}(p)| = 0$. With algebraic manipulation, tensor $\tilde{\mathbf{\Gamma}}^{(n)}$ can be written in a reduced form:

$$\tilde{\mathbf{\Gamma}}_{pqrs}^{(0)} = Q_{pq} Q_{rs} \tag{2.32}$$

$$\tilde{\mathbf{\Gamma}}_{pqrs}^{(1)} = V_{pq} Q_{rs} + V_{rs} Q_{pq} \tag{2.33}$$

$$\tilde{\mathbf{\Gamma}}_{pqrs}^{(2)} = \kappa_{pq} Q_{rs} + \kappa_{rs} Q_{pq} + V_{pq} V_{rs} \tag{2.34}$$

$$\tilde{\mathbf{\Gamma}}_{pqrs}^{(3)} = V_{pq} \kappa_{rs} + \kappa_{pq} V_{rs} \tag{2.35}$$

$$\tilde{\mathbf{\Gamma}}_{pqrs}^{(4)} = \kappa_{pq} \kappa_{rs} \tag{2.36}$$

Now, there are enough elements to write the Barnett-Lothe tensor in Equation 2.23. The displacement fundamental solution is obtained expressing $\boldsymbol{H}(\theta, \phi)$ as a double Fourier series:

$$H_{uv}(\theta, \phi) = \sum_{m=-\alpha}^{\alpha} \sum_{n=-\alpha}^{\alpha} \lambda_{uv}^{(m,n)} e^{i(m\theta + n\phi)} \tag{2.37}$$

with $(u, v) = 1, 2, 3$, α is an integer large enough to make the Fourier series converge, and $\lambda_{uv}^{(m,n)}$ are the unknown Fourier coefficients evaluated by:

$$\lambda_{uv}^{(m,n)} = \frac{1}{4\pi^2} \int_{-\pi}^{\pi} \int_{-\pi}^{\pi} H_{uv}(\theta, \phi) e^{-i(m\theta + n\phi)} d\theta d\phi \tag{2.38}$$

The calculated coefficients can be written with their real $R_{uv}^{(m,n)}$ and imaginary part $I_{uv}^{(m,n)}$, as:

$$\lambda_{uv}^{(m,n)} = R_{uv}^{(m,n)} + \mathbf{i} I_{uv}^{(m,n)} \tag{2.39}$$

To get rid of the imaginary part of Equation 2.37, it is rewritten as:

$$H_{uv}(\theta,\phi) = \sum_{m=-\alpha}^{\alpha}\sum_{n=-\alpha}^{\alpha} h_{uv}^{(m,n)}(\theta,\phi) \tag{2.40}$$

Using Equation 2.39 and Euler formula, it is possible to define $h_{uv}^{(m,n)}(\theta,\phi)$ as:

$$h_{uv}^{(m,n)}(\theta,\phi) = R_{uv}^{(m,n)}\cos(m\theta+n\phi) - I_{uv}^{(m,n)}\sin(m\theta+n\phi) \tag{2.41}$$

As $\lambda_{uv}^{(m,n)}$ and $\lambda_{uv}^{(-m,-n)}$ are conjugated, Equation 2.40 becomes:

$$\begin{aligned} H_{uv}(\theta,\phi) = 2\sum_{m=1}^{\alpha}\left\{\sum_{n=1}^{\alpha} h_{uv}^{(m,n)}(\theta,\phi) + \sum_{n=-\alpha}^{-1} h_{uv}^{(m,n)}(\theta,\phi)\right\} \\ + 2\sum_{n=1}^{\alpha} h_{uv}^{(0,n)}(\theta,\phi) + 2\sum_{m=1}^{\alpha} h_{uv}^{(m,0)}(\theta,\phi) + R_{uv}^{(0,0)} \end{aligned} \tag{2.42}$$

Substituting Equation 2.41 into 2.42, and then into 2.19, the displacement fundamental solution appears:

$$\begin{aligned} U_{uv} = \frac{1}{2\pi r}\Bigg\{\sum_{m=1}^{\alpha}\sum_{n=1}^{\alpha}\Big[(\tilde{R}_{uv}^{(m,n)}\cos m\theta - \tilde{I}_{uv}^{(m,n)}\sin m\theta)\cos n\phi \\ - (\hat{R}_{uv}^{(m,n)}\sin m\theta + \hat{I}_{uv}^{(m,n)}\cos m\theta)\sin n\phi\Big] \\ + \sum_{m=1}^{\alpha}\left[R_{uv}^{(0,m)}\cos m\phi - I_{uv}^{(0,m)}\sin m\phi + R_{uv}^{(m,0)}\cos m\phi - I_{uv}^{(m,0)}\sin m\phi\right] + \frac{R_{uv}^{(0,0)}}{2}\Bigg\} \end{aligned} \tag{2.43}$$

where

$$\tilde{R}_{uv}^{(m,n)} = R_{uv}^{(m,n)} + R_{uv}^{(m,-n)} \tag{2.44}$$

$$\hat{R}_{uv}^{(m,n)} = R_{uv}^{(m,n)} - R_{uv}^{(m,-n)} \tag{2.45}$$

$$\tilde{I}_{uv}^{(m,n)} = I_{uv}^{(m,n)} + I_{uv}^{(m,-n)} \tag{2.46}$$

$$\hat{I}_{uv}^{(m,n)} = I_{uv}^{(m,n)} - I_{uv}^{(m,-n)} \tag{2.47}$$

The first-order derivatives are obtained employing the chain rule as follows:

$$\boldsymbol{U}' = U_{uv,l} = \frac{\partial U_{uv}}{\partial r}\frac{\partial r}{\partial x_l} + \frac{\partial U_{uv}}{\partial \theta}\frac{\partial \theta}{\partial x_l} + \frac{\partial U_{uv}}{\partial \phi}\frac{\partial \phi}{\partial x_l} \tag{2.48}$$

The differentiation with respect to the spherical coordinates reintroduces complex numbers. To avoid that, the spatial differentiations are represented by:

$$\omega_l(\theta,\phi) = r\frac{\partial r}{\partial x_l} \tag{2.49}$$

$$\omega'_l(\theta,\phi) = r\frac{\partial \theta}{\partial x_l} \tag{2.50}$$

$$\omega''_l(\theta,\phi) = r\frac{\partial \phi}{\partial x_l} \tag{2.51}$$

For $l = 1$, one have:

$$\omega_1(\theta,\phi) = \sin\phi\cos\theta \tag{2.52}$$

$$\omega'_1(\theta,\phi) = -\sin\theta/\sin\phi \tag{2.53}$$

$$\omega''_1(\theta,\phi) = \cos\phi\cos\theta \tag{2.54}$$

For $l = 2$:

$$\omega_2(\theta,\phi) = \sin\phi\sin\theta \tag{2.55}$$

$$\omega'_2(\theta,\phi) = \cos\theta/\sin\phi \tag{2.56}$$

$$\omega''_2(\theta,\phi) = \cos\phi\sin\theta \tag{2.57}$$

For $l = 3$:

$$\omega_3(\theta,\phi) = \cos\phi \tag{2.58}$$

$$\omega'_3(\theta,\phi) = 0 \tag{2.59}$$

$$\omega''_3(\theta,\phi) = -\sin\phi \tag{2.60}$$

This allows the derivative to be written as:

$$\begin{aligned} &U_{uv,l} \\ &= \frac{1}{2\pi r^2}\Bigg\{-\omega_l(\theta,\phi)\left[\sum_{m=1}^{\alpha}\sum_{n=1}^{\alpha}((\widehat{\Gamma}_{uv}^{(m,n)}(\theta)\cos n\phi - \breve{\Gamma}_{uv}^{(m,n)}(\theta)\sin n\phi) + \sum_{m=1}^{\alpha}(\widehat{\gamma}_{uv}^{m}(\theta) + \breve{\gamma}_{uv}^{m}(\phi)) + \frac{R_{uv}^{(0,0)}}{2}\right] \\ &\quad - \omega'_l(\theta,\phi)\left[\sum_{m=1}^{\alpha}\sum_{n=1}^{\alpha} m(\tilde{\Gamma}_{uv}^{(m,n)}(\theta)\cos n\phi - \hat{\Gamma}_{uv}^{(m,n)}(\theta)\sin n\phi) + \sum_{m=1}^{\alpha} m\tilde{\gamma}_{uv}^{m}(\theta)\right] \\ &\quad - \omega''_l(\theta,\phi)\left[\sum_{m=1}^{\alpha}\sum_{n=1}^{\alpha} n(\widehat{\Gamma}_{uv}^{(m,n)}(\theta)\sin n\phi + \breve{\Gamma}_{uv}^{(m,n)}(\theta)\cos n\phi) + \sum_{m=1}^{\alpha} m\hat{\gamma}_{uv}^{m}(\phi)\right]\Bigg\} \end{aligned} \tag{2.61}$$

where

$$\widehat{\Gamma}_{uv}^{(m,n)}(\theta) = \tilde{R}_{uv}^{(m,n)} \cos m\theta - \tilde{I}_{uv}^{(m,n)} \sin m\theta \tag{2.62}$$

$$\breve{\Gamma}_{uv}^{(m,n)}(\theta) = \hat{R}_{uv}^{(m,n)} \sin m\theta + \hat{I}_{uv}^{(m,n)} \cos m\theta \tag{2.63}$$

$$\tilde{\Gamma}_{uv}^{(m,n)}(\theta) = \tilde{R}_{uv}^{(m,n)} \sin m\theta + \tilde{I}_{uv}^{(m,n)} \cos m\theta \tag{2.64}$$

$$\hat{\Gamma}_{uv}^{(m,n)}(\theta) = \hat{R}_{uv}^{(m,n)} \cos m\theta - \hat{I}_{uv}^{(m,n)} \sin m\theta \tag{2.65}$$

$$\widehat{\gamma}_{uv}^{m}(\theta) = R_{uv}^{(m,0)} \cos m\theta - I_{uv}^{(m,0)} \sin m\theta \tag{2.66}$$

$$\breve{\gamma}_{uv}^{m}(\phi) = R_{uv}^{(0,m)} \cos m\phi - I_{uv}^{(0,m)} \sin m\phi \tag{2.67}$$

$$\tilde{\gamma}_{uv}^{m}(\theta) = R_{uv}^{(m,0)} \sin m\theta + I_{uv}^{(m,0)} \cos m\theta \tag{2.68}$$

$$\hat{\gamma}_{uv}^{m}(\phi) = R_{uv}^{(0,m)} \sin m\phi + I_{uv}^{(0,m)} \cos m\phi \tag{2.69}$$

Now, the traction fundamental solution can be evaluated by:

$$t_{mi}^{*} = (\sigma_{mk} n_k)_i \tag{2.70}$$

with σ_{mk} being the generalized stresses and n_k the outward surface normal vector at the field point. Generalized Hooke's law allows writing stresses employing the Double Fourier series first-order derivative as:

$$(\sigma_{mk})_i = C_{mkjn} \frac{(U_{ji,n} + U_{ni,j})}{2} \tag{2.71}$$

A singularity occurs when source and field points are on the x_3 axis ($\phi = 0$ or $\phi = \pi$) for $l = 1$ and $l = 2$ because angle θ becomes ill-conditioned. To remove this singularity, Tan *et al.* (2013) suggestion is applied, introducing a small perturbation for ϕ, such as $\phi = 10^{-6}$, and $\theta = 0$ for $l = 1$, while $\theta = \pi/2$ for $l = 2$.

Resuming, Equation 2.43 is the displacement fundamental solution u_{mi}^{*} (only with different indexes) and Equation 2.70, with the help of Equations 2.71 and 2.61, is the traction fundamental solutions.

2.3 Dual Reciprocity Method for Thermoelasticity

The Dual Reciprocity Method is well exposed in Partridge *et al.* (1992) and its application in fully coupled thermoelasticity is shown in Gaul *et al.* (2003). In this thesis, these presentations are combined and simplified to uncoupled thermoelasticity. Domain integral of Equation 2.17 can be solved with classical DRM formulation. First, f_i^{el} is approximated with a summation of functions:

$$f_i^{el} \approx \sum_{q=1}^{N+L} f_{in}^q \alpha_n^q \tag{2.72}$$

with N being the number of boundary nodes and L being the number of internal points used for interpolation, as shown in Figure 2.2. For simplicity, they generally coincide with source points on the boundary and, if chosen, internal points of interest.

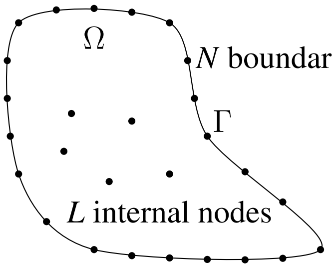

Figure 2.2 – Boundary and internal interpolation nodes for DRM.

The interpolation functions f_{in}^q are calculated from interpolation point n to field point i, while α_n^q are the coefficients of interpolation associated with each interpolation point. Applying this approximation in the domain integral of Equation 2.17, one has:

$$I = \int_\Omega f_i^{el} u_{mi}^* d\Omega \approx \int_\Omega u_{mi}^* \sum_{q=1}^{N+L} f_{in}^q \alpha_n^q d\Omega \tag{2.73}$$

The interpolation coefficients are constants and leave the integral. To transform it to Boundary Integrals, the differential operator of Equation 2.8 is applied:

$$\mathcal{L}_{ik} u_{kn}^q = f_{in}^q \tag{2.74}$$

Resulting in:

$$I \approx \int_\Omega \left\{ u_{mi}^* \sum_{q=1}^{N+L} C_{ijkl} u_{kn,jl}^q d\Omega \right\} \alpha_n^q \tag{2.75}$$

Integrating by parts and using the Divergence Theorem, the domain integrals vanish:

$$I \approx \sum_{q=1}^{N+L} \left\{ \int_\Gamma u_{mi}^* t_{in}^q d\Gamma - \int_\Gamma t_{mi}^* u_{in}^q d\Gamma - \delta_{mi} c(\xi) u_{in}^q(\xi) \right\} \alpha_n^q \tag{2.76}$$

Applying Equation 2.76 into Equation 2.17, the Boundary Integral Equation for thermoelasticity with DRM appears:

$$\begin{aligned} \delta_{mi} c(\xi) u_i(\xi) + \int_\Gamma t_{mi}^* u_i d\Gamma = & \int_\Gamma u_{mi}^* t_i d\Gamma + \int_\Gamma u_{mi}^* \gamma_{ij} n_j \theta d\Gamma \\ & + \sum_{q=1}^{N+L} \left\{ \delta_{mi} c(\xi) u_{in}^q(\xi) + \int_\Gamma t_{mi}^* u_{in}^q d\Gamma - \int_\Gamma u_{mi}^* t_{in}^q d\Gamma \right\} \alpha_n^q \end{aligned} \tag{2.77}$$

where u^q_{in} is the particular solution of Equation 2.74. BESLE uses the following RBF (Rodríguez, 2019):

$$u^q_{in} = \delta_{in}(r^2 + r^3) \tag{2.78}$$

and its derivatives:

$$u^q_{in,l} = \delta_{in}(2r + 3r^2)r_{,l} \tag{2.79}$$

$$u^q_{in,lm} = \delta_{in}[(2 + 3r)\delta_{lm} + 3rr_{,l}r_{,m}] \tag{2.80}$$

The other particular solution is calculated by:

$$t^q_{in} = C_{ijkl}u^q_{kn,j}n_l \tag{2.81}$$

The coefficients α^q_n are evaluated based on the total body force f^{el}_i. Remembering Equation 2.9, the body force for thermoelasticity is composed of an elastic component and a thermal effect. The first one is directly evaluated, but the thermal effect needs special treatment as presented by Gaul *et al.* (2003): the temperature field is approximated by a series of given functions ψ^q and unknown coefficients ζ^q, as:

$$\theta \approx \sum_{q=1}^{N+L} \psi^q \zeta^q \tag{2.82}$$

This approximation method is analogous to the DRM approach (Equation 2.72), but functions f^q_{in} and ψ^q are different, as coefficients α^q_n and ζ^q. Equation 2.82 is solved to evaluate coefficients ζ^q, and then, the gradient field can be interpolated by differentiation of the Equation 2.82 with respect to the cartesian coordinates:

$$\theta_{,j} \approx \sum_{q=1}^{N+L} \psi^q_{,j} \zeta^q \tag{2.83}$$

The functions ψ^q and $\psi^q_{,j}$ used by Gaul *et al.* (2003) are:

$$\psi^q = 1 + r^2 + r^3 \tag{2.84}$$

$$\psi^q_{,j} = (2r + 3r^2)r_{,j} \tag{2.85}$$

These are similar expressions used for f^q_{in}. Since no study concerning their use in thermoelastic applications was found, convergence analysis of different functions is an object of study in this work.

2.4 Radial Basis Functions

The main idea of the Dual Reciprocity Method is to use a function to approximate the kernel of an integral, whatever the name is given to this function. When Brebbia and Nardini (1983) proposed this technique, they used the function $1+r$, with r being the Euclidean distance. Over the decades, DRM was studied by many researchers, and several interpolation functions were tested, using the r distance. This type of function was named Radial Basis Functions, some of them listed in Table 2.1.

Table 2.1 – Common Radial Basis Functions types.

Type of function	Radial function	comments
	Piecewise smooth RBF	
Polyharmonic spline (PHS)	r^m	$m = 1, 3, 5, ...$
	$r^m \ln(r)$	$m = 2, 4, 6, ...$
Linear	r	particular PHS case
Cubic	r^3	particular PHS case
Thin plate spline (TPS)	$r^2 \ln(r)$	particular PHS case
	Infinitely smooth RBF	
Gaussian (GA)	$e^{-(\epsilon r)^2}$	$\epsilon > 0$
Multiquadric (MQ)	$\sqrt{1 + (\epsilon r)^2}$	$\epsilon > 0$
Inverse Quadratic (IQ)	$[1 + (\epsilon r)^2]^{-1}$	$\epsilon > 0$
Inverse Multiquadric (IMQ)	$\left[\sqrt{1 + (\epsilon r)^2}\right]^{-1}$	$\epsilon > 0$

The matrix generated by the RBF needs to be inverted to calculate the interpolation coefficients and it may become ill-conditioned when the interpolation points become close to each other. Karur and Ramachandran (1994) studied the convergence and the conditioning of this matrix on bidimensional domains using a linear function, a TPS, and a linear with a constant, but they could not find any relationship among them.

Considering Poisson problems, the TPS function should be preferred for bidimensional domains and the polynomial function (first PHS of the Table 2.1) should be reserved for tridimensional problems (Goldberg *et al.*, 1998). Thin plate spline showed better interpolation than cubic function despite both of them having linear convergence rate while the multiquadric (MQ) has exponential convergence (Goldberg *et al.*, 1996).

The infinitely smooth RBF are named this way because their derivatives always exist. The parameter ϵ, increasing from zero, increases the accuracy of the interpolation until an optimal value, and then, the accuracy decreases fast, together with the ill-conditioning of the interpolation matrix. Searching for the optimal ϵ, Goldberg *et al.* (1996) used cross-validation, while a list of recent methodologies in this matter can be found in Pooladi and Larsson (2023), some claiming to be computationally more efficient than others, but all of them mean extra computational cost.

The Method of Fundamental Solutions (MFS) and other meshless methods make great use of the interpolation functions and some important advancements were achieved. The interpolation is generally done using all interpolation nodes, meaning that a global interpolation is done, but Tolstykh and Shirobokov (2003) proposed a local interpolation by using a stencil built by a few points around an interpolation node. This produces a sparse interpolation matrix instead of a full matrix, taking advantage of the numerical techniques developed for sparse matrices, and this technique was named RBF-FD.

Flyer *et al.* (2016a) augmented the thin plate spline RBF-FD with polynomials of various orders and improved the accuracy to a certain level. A rule concerning the maximum order of the augmented polynomial, the stencil size used, and the accuracy in interpolation was presented by Flyer *et al.* (2016b). The augmented polynomials were used by BEM long before, but until Goldberg *et al.* (1999), only the first-order polynomials were used obtaining the same effect of increasing accuracy that was obtained in RBF-FD.

On using interpolation functions into thermoelasticity to interpolate the derivative of the temperature field as proposed by Gaul *et al.* (2003), particular situations appear and some care must be taken. Mai-Duy and Tran-Cong (2003) demonstrated that a good primitive interpolant function may be not so good interpolant for the derivative. So, considering the PHS of Table 2.1, its derivative can be calculated resulting in:

$$\psi_{,j} = mr^{m-2}r_j \tag{2.86}$$

with r_j being the component of r vector in j-th direction. If $m = 1$, a singularity occurs when r goes to 0. For $m > 1$, the literature recommends that only odd values should be used. The singularity also appears in derivatives of the logarithmic function of Table 2.1 for any value of m, as shown in Equation 2.87.

$$\psi_{,j} = [m\ln(r) + 1]r^{m-2}r_j \tag{2.87}$$

To avoid this singularity, a small change in this function is proposed:

$$\psi = r^m \ln(r + 1) \tag{2.88}$$

which leads to the derivative

$$\psi_{,j} = \left[m r^{m-2} \ln(r+1) + \frac{r^{m-1}}{r+1} \right] r_j \tag{2.89}$$

With this function, the singularity is avoided for $m > 1$. Together with the polynomial and the function of Equation 2.84, they will be explored in this work. The search for an optimal shape parameter is not in the scope of this thesis and for this reason, the infinitely smooth RBF of Table 2.1 will not be used.

2.5 BESLE notes

BESLE is a Boundary Elements software created by Galvis *et al.* (2021) composed of a Mesh Generator module, a Material processing module, and the BESLE solver module that uses as input the data generated from the first two modules.

The Mesh Generator module is divided into three submodules. Simple rectangular prisms can be generated by the Box submodule, built in a MATLAB code, which also defines the mesh refinement and it is able to split the geometry into subregions. Only the mesh is processed, and boundary conditions are set in the configuration file of the BESLE solver module.

Another mesh submodule named General is built in a Fortran code which reads **.obj* files exported from 3DSMax Autodesk software. The advantage against the Box submodule is the possibility to create any geometry, although the refinement mesh degree has to be defined at the 3DSMax, as well as the elements with boundary conditions, which may be quite a difficult task depending on the user's skills on this software.

The General submodule reads the **.obj* files and organizes the data in a format ready for the BESLE solver module, including boundary conditions, so the last module only reads this data. The BESLE solver module also considers that all elements without boundary conditions set are free elements, or else, they are imposed null tractions. By doing this, only displacements or non-zero tractions boundary conditions need to be defined at the General submodule.

There is another Mesh Generator submodule named Polycrystal developed in C++ language dedicated to generating materials with several crystals or grains with their own crystalline orientation and planes, but it is not used in this work.

The Material module is a serial Fortran code responsible for evaluating the Fourier coefficients used at the fundamental solution. The material is defined as iso- or anisotropic and its properties are set in the configuration file for the Material module. The code is capable of evaluating properties by the rotation on the cartesian axes and it can deal with some lattices of crystal morphologies. If multiple materials are used, the properties are set in separate files and the configuration file only sets which files must be read. This early evaluation of the Fourier coefficients saves time for the main code and also allows the creation of a materials library that can be reused at any other simulation.

The BESLE solver module is the main code built in Fortran language with parallelization using Message Passage Interface (MPI), a communication protocol for distributed memory allowing its use at parallel computers or supercomputers (clusters). It has scalable parallelism, and the user just needs to have more threads available and set them to be used at the run start. In other words, BESLE aims to solve problems with a large degree of freedom.

The parallelization at BESLE is reserved for the high computational cost tasks. If multiregions are defined, BESLE automatically identifies the interfaces by comparing the coordinates of the geometric nodes of each element to all elements of different regions. This task is divided among the total number of processes, reducing the necessary time to identify the interfaces.

The evaluation of the boundary integrals is divided among the threads by the number of the elements of the mesh, in a very balanced division, providing great speed up as the number of processes is increased for a fixed number of elements.

The Dual Reciprocity Method computation is another parallelized task divided among the threads by the total number of points used for interpolation (boundary plus domain points). The interpolation matrix of the DRM is inverted by using the block matrix inversion, a procedure that subdivides the matrix which needs to be inverted into four submatrices and using the Schur complement of a block matrix. The implementation in BESLE recursively subdivides the matrix into blocks three times to make better use of parallelization and memory use.

To solve the linear system, BESLE uses MUMPS, a parallel sparse direct solver for large linear systems, which is able to deal with general unsymmetric or sparse matrices, with parallel factorization using libraries such as BLAS, BLACS, and ScaLAPACK. There are some different ways of sending the coefficients matrix of the linear system to MUMPS, and BESLE sends only the non-zero values. By doing this, MUMPS reduces memory usage and also speeds up the calculation of solutions by reducing the number of calculations done. This is particularly strong for sparse matrices, as it happens for the subregion procedure, shown in Section 2.7.

The results calculated by the MUMPS are the displacements and tractions of the nodal points. The evaluation of stresses and strains is done by using the shape functions as presented in Section 2.8.

All of these features were implemented by Galvis *et al.* (2021). The author of this thesis implemented more tools to improve the capabilities of BESLE. The 3DSMax has the drawbacks of not being available for Linux systems and its license is very expensive. For this reason, the free and open-source Blender software was used instead of 3DSMax, and the General module was updated to be able to read Blender **.obj* exported files, since there are small differences between the exported files of each software.

The thermoelastic formulation requires the evaluation of an extra boundary integral and a volume integral. The boundary integral is evaluated together with the integration of the ordinary boundary integrals of the elasticity problems. Some conditionals for thermoelastic problems were included at many points of the code to make use of the elasticity results of integration, speeding up the calculations.

The volume integral is evaluated using the Dual Reciprocity Method. Several specific calculations are necessary for thermoelasticity, so many conditionals were added to do them, as well as to use the particular interpolation functions for the thermperature. The use of internal points was added to BESLE as a new feature, but the coordinates of the internal points are not computed automatically: the user has to manually calculate them and put their coordinates in a file that is read by BESLE.

The stresses and strains evaluation for thermoelasticity problems needs to consider the thermal effects, so another conditional was added to compute them adequately.

The high computational cost tasks were kept parallelized, increasing the performance of the thermoelastic implemented tools.

2.6 Discretization

To use Boundary Integral of Equation 2.77, the geometry must be split into elements where integration applies. Then, boundary integral becomes the summation of the integration over all elements, given in Equation 2.90.

$$\begin{aligned}
&\delta_{mi}c(\xi)u_i(\xi) + \sum_{EL=1}^{NEL}\left(\int_{\Gamma_{EL}} t^*_{mi}h^{(k)}u_i^{(k)}d\Gamma\right) \\
&= \sum_{EL=1}^{NEL}\left(\int_{\Gamma_{EL}} u^*_{mi}h^{(k)}t_i^{(k)}d\Gamma\right) + \sum_{EL=1}^{NEL}\left(\int_{\Gamma_{EL}} u^*_{mi}\gamma_{ij}n_jh^{(k)}\theta^{(k)}d\Gamma\right) \\
&\quad + \sum_{q=1}^{N+L}\left\{\delta_{mi}c(\xi)u^q_{in}(\xi) + \sum_{EL=1}^{NEL}\left(\int_{\Gamma_{EL}} t^*_{mi}h^{(k)}u^q_{in}d\Gamma\right) - \sum_{EL=1}^{NEL}\left(\int_{\Gamma_{EL}} u^*_{mi}h^{(k)}t^q_{in}d\Gamma\right)\right\}\alpha^q_n
\end{aligned} \tag{2.90}$$

where EL is the element index, NEL is the number of elements, $h^{(k)}$ are the shape functions for the variable interpolation at the element, with the superscript (k) identifying the *k*-th node of the element.

BESLE uses discontinuous linear three-node triangular boundary elements as shown in Figure 2.3, with $\lambda = 0.155$ (Galvis *et al.*, 2021), meaning that $k = 1, 2, 3$ in Equation 2.90. The discontinuous element simplifies the multidomain formulation, while the triangular elements reproduce a general geometry better than the rectangular ones and can easily be generated by the software mentioned in Section 2.5. Also, the linear interpolation implies a reduction in the total degree of freedom compared to the high-order interpolation with the same amount of elements.

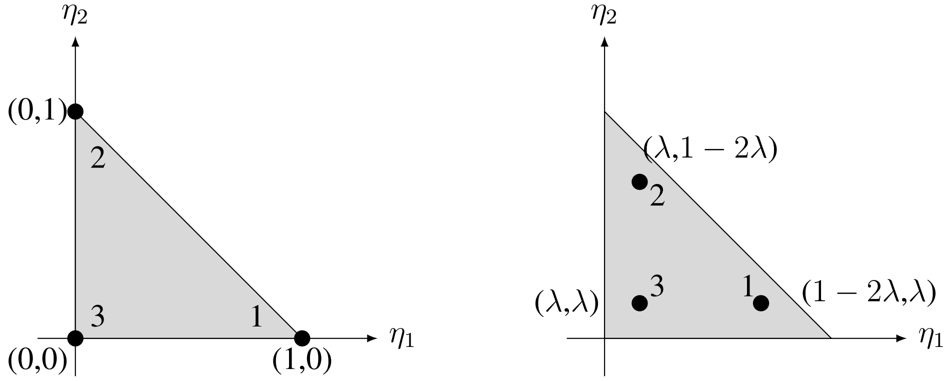

Figure 2.3 – Linear three-node continuous (left) and discontinuous (right) element. Values between parenthesis mean intrinsic coordinates while the number alone means the node sequence.

The integral over a surface element using two intrinsic coordinates (η_1 and η_2)

means that a double integral must be solved, and for the triangular element it becomes:

$$\begin{aligned}\delta_{mi}c(\xi)u_i(\xi) &+ \sum_{EL=1}^{NEL}\left(\int_0^1\int_0^{1-\eta_2} t^*_{mi}h^{(k)}u_i^{(k)}Jd\eta_1 d\eta_2\right)\\
&= \sum_{EL=1}^{NEL}\left(\int_0^1\int_0^{1-\eta_2} u^*_{mi}h^{(k)}t_i^{(k)}Jd\eta_1 d\eta_2\right) + \sum_{EL=1}^{NEL}\left(\int_0^1\int_0^{1-\eta_2} u^*_{mi}\gamma_{ij}n_j h^{(k)}\theta^{(k)}Jd\eta_1 d\eta_2\right)\\
&+ \sum_{q=1}^{N+L}\Bigg\{\delta_{mi}c(\xi)u^q_{in}(\xi) + \sum_{EL=1}^{NEL}\left(\int_0^1\int_0^{1-\eta_2} t^*_{mi}h^{(k)}u^q_{in}Jd\eta_1 d\eta_2\right)\\
&\qquad - \sum_{EL=1}^{NEL}\left(\int_0^1\int_0^{1-\eta_2} u^*_{mi}h^{(k)}t^q_{in}Jd\eta_1 d\eta_2\right)\Bigg\}\alpha^q_n\end{aligned} \tag{2.91}$$

with J being the Jacobian of the transformation from global coordinates to intrinsic coordinates. The evaluation of the integrals by standard Gaussian Quadrature would require double summation, but the combination of the intrinsic coordinate points and weights allows each integral to be evaluated by a simple sum (see Kane (1994) for more details). Applying this concept to the Equation 2.91, it is written as:

$$\begin{aligned}\delta_{mi}c(\xi)u_i(\xi) &+ \sum_{EL=1}^{NEL}\left(\sum_{n=1}^{NGP} t^{*(n)}_{mi}h^{(kn)}u_i^{(k)}J\omega^{(n)}\right)\\
&= \sum_{EL=1}^{NEL}\left(\sum_{n=1}^{NGP} u^{*(n)}_{mi}h^{(kn)}t_i^{(k)}J\omega^{(n)}\right) + \sum_{EL=1}^{NEL}\left(\sum_{n=1}^{NGP} u^{*(n)}_{mi}\gamma_{ij}n_j h^{(kn)}\theta^{(k)}J\omega^{(n)}\right)\\
&+ \sum_{q=1}^{N+L}\Bigg\{\delta_{mi}c(\xi)u^q_{in}(\xi) + \sum_{EL=1}^{NEL}\left(\sum_{n=1}^{NGP} t^{*(n)}_{mi}h^{(kn)}u^q_{in}J\omega^{(n)}\right)\\
&\qquad - \sum_{EL=1}^{NEL}\left(\sum_{n=1}^{NGP} u^{*(n)}_{mi}h^{(kn)}t^q_{in}J\omega^{(n)}\right)\Bigg\}\alpha^q_n\end{aligned} \tag{2.92}$$

where the superscripts (n) indicates the values related to the *n*-th Gauss point.

At each element, displacements and tractions surface response are interpolated by the discontinuous shape functions $h^{(k)}$. Let $V^{(k)}$ be a generalized field at the *k*-th element node. The interpolated field v and first derivatives at a (η_1, η_2) point are given by:

$$v(\eta_1,\eta_2) = \sum_{k=1}^{3} h^{(k)}(\eta_1,\eta_2)V^{(k)} \tag{2.93}$$

$$\frac{\partial v(\eta_1,\eta_2)}{\partial \eta_1} = \sum_{k=1}^{3} \frac{\partial h^{(k)}(\eta_1,\eta_2)}{\partial \eta_1}V^{(k)} \tag{2.94}$$

$$\frac{\partial v(\eta_1,\eta_2)}{\partial \eta_2} = \sum_{k=1}^{3} \frac{\partial h^{(k)}(\eta_1,\eta_2)}{\partial \eta_2}V^{(k)} \tag{2.95}$$

The discontinuous shape functions $h^{(k)}$ are obtained numerically following the generic matricial procedure presented by Kane (1994). Consider the continuous shape functions below:

$$N^{(1)} = \eta_1 \tag{2.96}$$

$$N^{(2)} = \eta_2 \tag{2.97}$$

$$N^{(3)} = 1 - \eta_1 - \eta_2 \tag{2.98}$$

The interpolated field in terms of continuous functions is:

$$v(\eta_1, \eta_2) = \sum_{k=1}^{3} N^{(k)}(\eta_1, \eta_2) V^{(k)} \tag{2.99}$$

Or in matrix form:

$$\{\boldsymbol{v}\} = [\boldsymbol{N}]\{\boldsymbol{V}\} \tag{2.100}$$

Let $\{\boldsymbol{w}_j\}$ be the nodal values at j-th node for the discontinuous element shown in Figure 2.3:

$$\{\boldsymbol{w}_j\} = \sum_{k=1}^{3} N^{(k)}(\eta_1, \eta_2) V^{(k)} \tag{2.101}$$

Explicit matrices for this equation are:

$$\left\{ \begin{array}{c} w_1 \\ w_2 \\ w_3 \end{array} \right\} = \left[\begin{array}{ccc} N^{(1)}(1-2\lambda, \lambda) & N^{(2)}(1-2\lambda, \lambda) & N^{(3)}(1-2\lambda, \lambda) \\ N^{(1)}(\lambda, 1-2\lambda) & N^{(2)}(\lambda, 1-2\lambda) & N^{(3)}(\lambda, 1-2\lambda) \\ N^{(1)}(\lambda, \lambda) & N^{(2)}(\lambda, \lambda) & N^{(3)}(\lambda, \lambda) \end{array} \right] \left\{ \begin{array}{c} V^{(1)} \\ V^{(2)} \\ V^{(3)} \end{array} \right\} \tag{2.102}$$

Or in a compact form:

$$\{\boldsymbol{w}\} = [\boldsymbol{L}]\{\boldsymbol{V}\} \tag{2.103}$$

where $[L]$ has the values of the continuous shape functions at the discontinuous nodes. The inversion of Equation 2.103 turns out an expression for the values on continuous nodes expressed in terms of discontinuous nodes:

$$\{\boldsymbol{V}\} = [\boldsymbol{L}]^{-1}\{\boldsymbol{w}\} \tag{2.104}$$

Applying Equation 2.104 into 2.100, values at any point within the element are interpolated in terms of values of discontinuous elements.

$$\{\boldsymbol{v}\} = [\boldsymbol{N}][\boldsymbol{L}]^{-1}\{\boldsymbol{w}\} = [\boldsymbol{D}]\{\boldsymbol{w}\} \tag{2.105}$$

So, the discontinuous shape functions are evaluated by:

$$[\boldsymbol{D}] = [\boldsymbol{N}][\boldsymbol{L}]^{-1} \tag{2.106}$$

where $[\boldsymbol{D}] = [h^{(1)}\ h^{(2)}\ h^{(3)}]$ are the discontinuous shape function values calculated for each node. Derivatives of the discontinuous shape functions with respect to η_1 and η_2 are obtained by derivation of the Equation 2.105:

$$\frac{\partial v_j(\eta_1,\eta_2)}{\partial \eta_1} = \sum_{k=1}^{3} \frac{\partial N^{(k)}(\eta_1,\eta_2)}{\partial \eta_1} V_j^{(k)} = [\boldsymbol{N}]_{,\eta_1}[\boldsymbol{L}]^{-1}\{\boldsymbol{w}\} = [\boldsymbol{D}]_{,\eta_1}\{\boldsymbol{w}\} \tag{2.107}$$

$$\frac{\partial v_v(\eta_1,\eta_2)}{\partial \eta_2} = \sum_{k=1}^{3} \frac{\partial N^{(k)}(\eta_1,\eta_2)}{\partial \eta_2} V_j^{(k)} = [\boldsymbol{N}]_{,\eta_2}[\boldsymbol{L}]^{-1}\{\boldsymbol{w}\} = [\boldsymbol{D}]_{,\eta_2}\{\boldsymbol{w}\} \tag{2.108}$$

with $[\boldsymbol{D}]_{,\eta_1}$ and $[\boldsymbol{D}]_{,\eta_2}$ being the derivatives of discontinuous shape functions.

The Jacobian of Equation 2.91 is calculated by following the transformation of differential surface area $d\Gamma$ (Figure 2.4) at global coordinates to the differential surface area $d\gamma$ at intrinsic coordinates. The cross-product is used to evaluate $d\Gamma$:

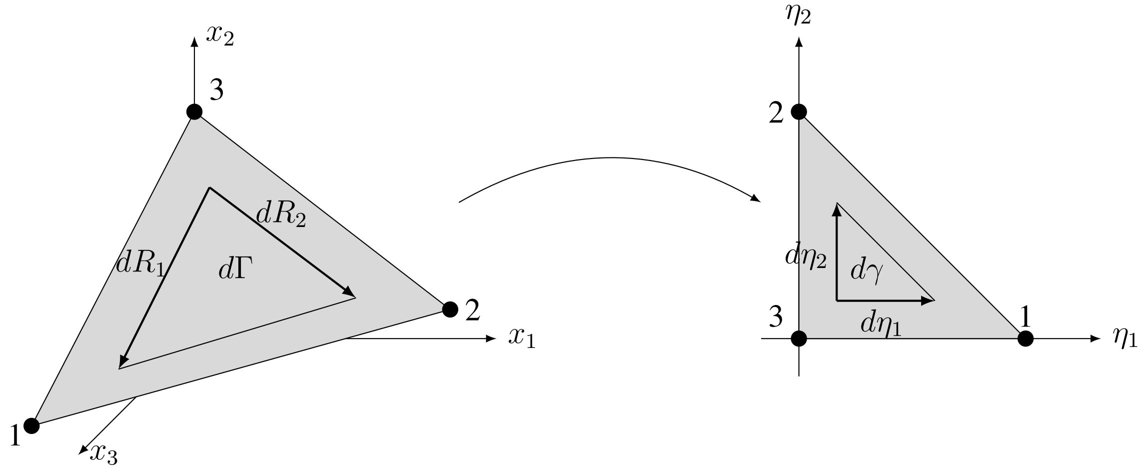

Figure 2.4 – Mapping of the triangular element from global cartesian coordinates to intrinsic coordinates for Gauss integration.

$$d\Gamma = \frac{1}{2}\left\|d\vec{R}_1 \times d\vec{R}_2\right\| = \frac{1}{2}\left\|\frac{\partial \vec{R}}{\partial \eta_1} \times \frac{\partial \vec{R}}{\partial \eta_2}\right\| d\eta_1 d\eta_2 \tag{2.109}$$

where

$$\vec{R} = x_k \vec{e}_k \tag{2.110}$$

This leads to:

$$\frac{\partial \vec{R}}{\partial \eta_1} = \frac{\partial x_k}{\partial \eta_1}\vec{e}_k \tag{2.111}$$

$$\frac{\partial \vec{R}}{\partial \eta_2} = \frac{\partial x_k}{\partial \eta_2} \vec{e}_k \tag{2.112}$$

Applying Equations 2.111 and 2.112 into 2.109 produces

$$J_1 = \frac{\partial x_2}{\partial \eta_1}\frac{\partial x_3}{\partial \eta_2} - \frac{\partial x_3}{\partial \eta_1}\frac{\partial x_2}{\partial \eta_2} \tag{2.113}$$

$$J_2 = \frac{\partial x_3}{\partial \eta_1}\frac{\partial x_1}{\partial \eta_2} - \frac{\partial x_1}{\partial \eta_1}\frac{\partial x_3}{\partial \eta_2} \tag{2.114}$$

$$J_3 = \frac{\partial x_1}{\partial \eta_1}\frac{\partial x_2}{\partial \eta_2} - \frac{\partial x_2}{\partial \eta_1}\frac{\partial x_1}{\partial \eta_2} \tag{2.115}$$

The Jacobian can be calculated as:

$$J = \frac{1}{2}\sqrt{J_1^2 + J_2^2 + J_3^2} \tag{2.116}$$

Normal vectors are defined by:

$$n_k = J_k J^{-1} \tag{2.117}$$

Applying the shape functions for the linear elements, the interpolation is given by:

$$x_k = \eta_1 x_k^{(1)} + \eta_2 x_k^{(2)} + (1 - \eta_1 - \eta_2) x_k^{(3)} \tag{2.118}$$

with the superscripts meaning the element node. The derivatives are:

$$\frac{\partial x_k}{\partial \eta_1} = x_k^{(1)} - x_k^{(3)} \tag{2.119}$$

$$\frac{\partial x_k}{\partial \eta_2} = x_k^{(2)} - x_k^{(3)} \tag{2.120}$$

This means that the derivatives are constant along the entire element. Applying to Equations 2.113 to 2.115:

$$J_1 = (x_3^{(2)} - x_3^{(3)})(x_2^{(1)} - x_2^{(3)}) - (x_2^{(2)} - x_2^{(3)})(x_3^{(1)} - x_3^{(3)}) \tag{2.121}$$

$$J_2 = (x_1^{(2)} - x_1^{(3)})(x_3^{(1)} - x_3^{(3)}) - (x_3^{(2)} - x_3^{(3)})(x_1^{(1)} - x_1^{(3)}) \tag{2.122}$$

$$J_3 = (x_2^{(2)} - x_2^{(3)})(x_1^{(1)} - x_1^{(3)}) - (x_1^{(2)} - x_1^{(3)})(x_2^{(1)} - x_2^{(3)}) \tag{2.123}$$

Equations 2.121 to 2.123 are used in Equation 2.116 to calculate the Jacobian, which depends only on the global coordinates of the vertices of the triangle element, being a constant value along the element.

Table 2.2 – Gauss points and respective weights used at BESLE.

$I = \int_0^1 \int_0^{1-\eta_2} f(\eta_1, \eta_2) d\eta_1 d\eta_2 \approx \sum_{k=1}^{NGP} f(\eta_1^{(k)}, \eta_2^{(k)}) \omega^{(k)}$			
NGP	$\eta_1^{(k)}$	$\eta_2^{(k)}$	$\omega^{(k)}$
7	0.3333333333	0.3333333333	0.2550000000
	0.7974269853	0.1012865073	0.1259391805
	0.1012865073	0.7974269853	0.1259391805
	0.1012865073	0.1012865073	0.1259391805
	0.0597158717	0.4701420641	0.1323941527
	0.4701420641	0.0597158717	0.1323941527
	0.4701420641	0.4701420641	0.1323941527
13	0.0651301029	0.0651301029	0.0533472356
	0.8697297941	0.0651301029	0.0533472356
	0.0651301029	0.8697297941	0.0533472356
	0.3128654960	0.0486903154	0.0771137608
	0.6384441885	0.3128654960	0.0771137608
	0.0486903154	0.6384441885	0.0771137608
	0.6384441885	0.0486903154	0.0771137608
	0.3128654960	0.6384441885	0.0771137608
	0.0486903154	0.3128654960	0.0771137608
	0.2603459660	0.2603459660	0.1756152574
	0.4793080678	0.2603459660	0.1756152574
	0.2603459660	0.4793080678	0.1756152574
	0.3333333333	0.3333333333	-0.1495700444

The number of Gauss points used in Equation 2.92 depends on the configurations set at BESLE and on the location of the source point. BESLE is ready to use the rule of 7 or 13 Gauss points for a single triangle, as given by Table 2.2.

BESLE can increase this number of points by splitting the element into sub-triangles and applying the Gauss points to each one. BESLE can split the element into 4, 8, or 16 subtriangles as shown in Figure 2.5. So, the 7 Gauss points rule becomes 28, 56, or 112 points, and the 13 Gauss points rule becomes 52, 104, or 208 points.

When the source point lies outside the integrated element, the integration is regular and it is evaluated using the configuration just explained. When the source point is inside the integrated element, singularities of the fundamental solution appear. A special Gaussian integral scheme for singular integration exists but BESLE solves the singular integration by increasing the amount of Gauss points around the singularity. First, the element is split as shown in Figure 2.6, depending on the location of the source point. Red quadrilaterals and blue triangles use 16 Gauss points each, while green triangles use 13 points each. The blue triangles are always around the source point and they are the closest to the singularity, being

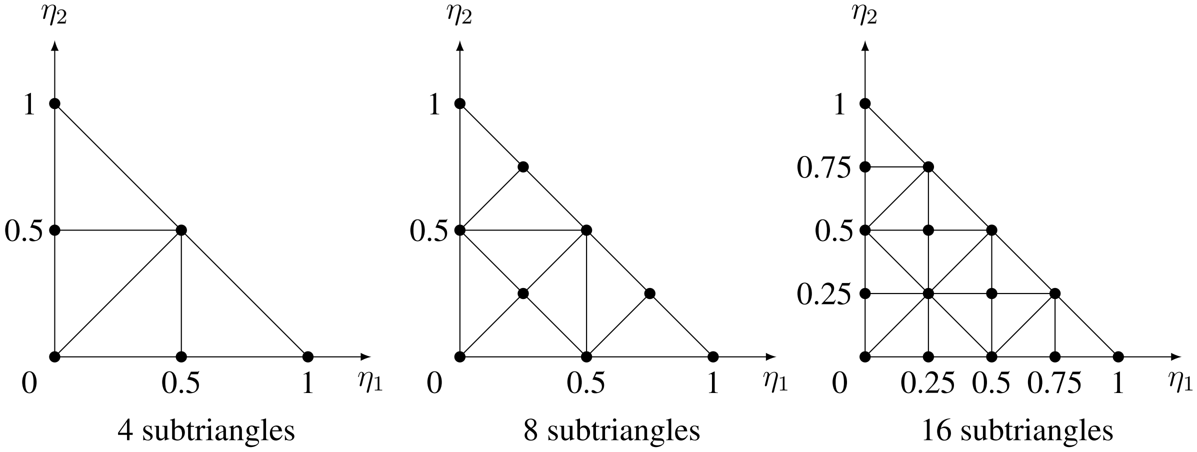

Figure 2.5 – Triangle element subdivision into subtriangles.

quadrilaterals degenerated into triangles, by forcing two nodes of the quadrilateral coincide at the source point. In total, 109 Gauss points are used for cases (a) and (b), and 128 points for the case (c). The subdivision into triangles does not apply to the singular integration.

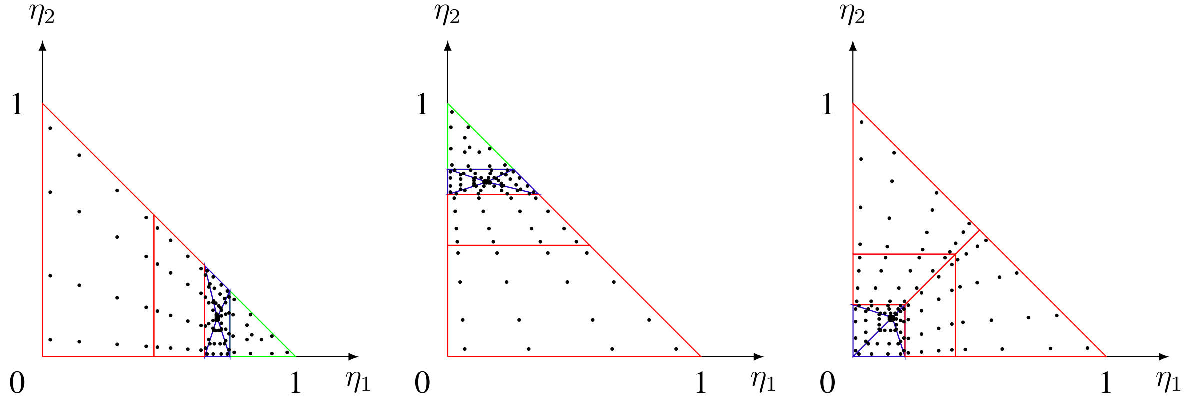

Figure 2.6 – Triangle subdivision and distribution of Gauss points for the integration of singular kernels for source points at coordinates: left $(1-2\lambda, \lambda)$, center $(\lambda, 1-2\lambda)$, and right (λ, λ).

For each source point integrated over an element, the terms in Equations 2.92 can be expressed by the following matricial form:

$$\sum_{n=1}^{NGP} t_{mi}^{*(n)} J\omega^{(n)} = [\boldsymbol{T}^{*}]^{T} = \begin{bmatrix} t_{11} & t_{21} & t_{31} \\ t_{12} & t_{22} & t_{32} \\ t_{13} & t_{23} & t_{33} \end{bmatrix} \tag{2.124}$$

$$\sum_{n=1}^{NGP} u_{mi}^{*(n)} J\omega^{(n)} = [\boldsymbol{U^*}]^T = \begin{bmatrix} u_{11} & u_{21} & u_{31} \\ u_{12} & u_{22} & u_{32} \\ u_{13} & u_{23} & u_{33} \end{bmatrix} \tag{2.125}$$

$$h^{(kn)} = [\boldsymbol{h}] = \begin{bmatrix} h^{(1)} & 0 & 0 & h^{(2)} & 0 & 0 & h^{(3)} & 0 & 0 \\ 0 & h^{(1)} & 0 & 0 & h^{(2)} & 0 & 0 & h^{(3)} & 0 \\ 0 & 0 & h^{(1)} & 0 & 0 & h^{(2)} & 0 & 0 & h^{(3)} \end{bmatrix} \tag{2.126}$$

$$u_i^{(k)} = \{\boldsymbol{u}\}^{el} = \begin{bmatrix} u_1^{(1)} & u_2^{(1)} & u_3^{(1)} & u_1^{(2)} & u_2^{(2)} & u_3^{(2)} & u_1^{(3)} & u_2^{(3)} & u_3^{(3)} \end{bmatrix}^T \tag{2.127}$$

$$t_i^{(k)} = \{\boldsymbol{t}\}^{el} = \begin{bmatrix} t_1^{(1)} & t_2^{(1)} & t_3^{(1)} & t_1^{(2)} & t_2^{(2)} & t_3^{(2)} & t_1^{(3)} & t_2^{(3)} & t_3^{(3)} \end{bmatrix}^T \tag{2.128}$$

$$\theta^{(k)} = \{\boldsymbol{\theta}\}^{el} = \begin{bmatrix} \theta^{(1)} & \theta^{(1)} & \theta^{(1)} & \theta^{(2)} & \theta^{(2)} & \theta^{(2)} & \theta^{(3)} & \theta^{(3)} & \theta^{(3)} \end{bmatrix}^T \tag{2.129}$$

$$\gamma_{ij} = [\boldsymbol{\Gamma}]^{el} = \begin{bmatrix} \gamma_{11} & \gamma_{12} & \gamma_{13} \\ \gamma_{21} & \gamma_{22} & \gamma_{23} \\ \gamma_{31} & \gamma_{32} & \gamma_{33} \end{bmatrix} \tag{2.130}$$

$$n_j = [\boldsymbol{n}]^{el} = \begin{bmatrix} n_1 & 0 & 0 \\ 0 & n_2 & 0 \\ 0 & 0 & n_3 \end{bmatrix} \tag{2.131}$$

$$\delta_{mi} c(\xi) = [\boldsymbol{\delta}] = \begin{bmatrix} 0.5 & 0 & 0 \\ 0 & 0.5 & 0 \\ 0 & 0 & 0.5 \end{bmatrix} = 0.5[\boldsymbol{I}] \tag{2.132}$$

The source points ξ are placed by using the collocation method, making them coincide with the discontinuous nodes, producing a number of equations equal to the total degree of freedom of the mesh. Then, the terms of the Equations 2.124 to 2.132 become matrices as given by the Equations 2.133 to 2.137.

$$\delta_{mi} c(\xi) u_i(\xi) + \sum_{EL=1}^{NEL} \left(\sum_{n=1}^{NGP} t_{mi}^{*(n)} h^{(kn)} u_i^{(k)} J\omega^{(n)} \right) = \left(0.5[\boldsymbol{I}] + [\boldsymbol{T^*}]^T [\boldsymbol{h}] \right) \{\boldsymbol{u}\} = [\boldsymbol{H}]\{\boldsymbol{u}\} \tag{2.133}$$

$$\sum_{EL=1}^{NEL} \left(\sum_{n=1}^{NGP} u_{mi}^{*(n)} h^{(kn)} t_i^{(k)} J\omega^{(n)} \right) = \left([\boldsymbol{U^*}]^T [\boldsymbol{h}] \right) \{\boldsymbol{t}\} = [\boldsymbol{G}]\{\boldsymbol{t}\} \tag{2.134}$$

$$\sum_{EL=1}^{NEL} \left(\sum_{n=1}^{NGP} u_{mi}^{*(n)} \gamma_{ij} n_j h^{(kn)} \theta^{(k)} J\omega^{(n)} \right) = [\boldsymbol{U^*}]^T [\boldsymbol{\Gamma}][\boldsymbol{n}][\boldsymbol{h}]\{\boldsymbol{\theta}\} = \{\boldsymbol{b}^{t1}\} \tag{2.135}$$

$$\sum_{q=1}^{N+L} \delta_{mi} c(\xi) u_{in}^{q}(\xi) + \sum_{EL=1}^{NEL} \left(\sum_{n=1}^{NGP} t_{mi}^{*(n)} h^{(kn)} u_{in}^{q} J\omega^{(n)} \right) = \left(0.5[\boldsymbol{I}] + [\boldsymbol{T}^{*}]^{T}[\boldsymbol{h}]\right)[\hat{\boldsymbol{U}}] = [\boldsymbol{H}][\hat{\boldsymbol{U}}] \tag{2.136}$$

$$\sum_{q=1}^{N+L} \sum_{EL=1}^{NEL} \left(\sum_{n=1}^{NGP} u_{mi}^{*(n)} h^{(kn)} t_{in}^{q} J\omega^{(n)} \right) = \left([\boldsymbol{U}^{*}]^{T}[\boldsymbol{h}]\right)[\hat{\boldsymbol{T}}] = [\boldsymbol{G}][\hat{\boldsymbol{T}}] \tag{2.137}$$

where $[\hat{\boldsymbol{U}}]$ and $[\hat{\boldsymbol{T}}]$ are generated by the terms u_{in}^{q} and t_{in}^{q}. Also, α_{n}^{q} generates the vector of DRM coefficients of interpolation $\{\boldsymbol{\alpha}\}$. Then, the Boundary Integral Equation 2.77 takes the matricial form

$$[\boldsymbol{H}]\{\boldsymbol{u}\} = [\boldsymbol{G}]\{\boldsymbol{t}\} + \{\boldsymbol{b}^{t1}\} + \Big([\boldsymbol{H}][\hat{\boldsymbol{U}}] - [\boldsymbol{G}][\hat{\boldsymbol{T}}]\Big)\{\boldsymbol{\alpha}\} \tag{2.138}$$

The Equation 2.72 can be written in the matricial form:

$$\{\hat{\boldsymbol{b}}\} = [\boldsymbol{F}]\{\boldsymbol{\alpha}\} \tag{2.139}$$

where $[\boldsymbol{F}]$ is the matrix generated by f_{in}^{q} and $\{\hat{\boldsymbol{b}}\}$ is the body force f_{i}^{el}. Coefficients $\{\boldsymbol{\alpha}\}$ can be calculated using the inverse matrix $[\boldsymbol{F}]^{-1}$:

$$\{\boldsymbol{\alpha}\} = [\boldsymbol{F}]^{-1}\{\hat{\boldsymbol{b}}\} \tag{2.140}$$

As it was shown in Section 2.3, the total body force $\{\hat{\boldsymbol{b}}\}$ consists of an elastic component plus a thermal effect, given by Equation 2.9. Rewriting it into matricial form:

$$\{\hat{\boldsymbol{b}}\} = -\{\hat{\boldsymbol{b}}^{el}\} + \{\hat{\boldsymbol{b}}^{t2}\}, \tag{2.141}$$

The temperature field is interpolated by a sum of functions (Equation 2.82):

$$\{\boldsymbol{\theta}\} \approx [\boldsymbol{E}]\{\boldsymbol{\zeta}\} \tag{2.142}$$

The coefficients of interpolation $\{\boldsymbol{\zeta}\}$ are calculated by inverting matrix $[\boldsymbol{E}]$:

$$\{\boldsymbol{\zeta}\} = [\boldsymbol{E}]^{-1}\{\boldsymbol{\theta}\} \tag{2.143}$$

This allows the gradient thermal field to be evaluated (Equation 2.83):

$$\{\boldsymbol{\theta}'\} \approx [\boldsymbol{E}']\{\boldsymbol{\zeta}\} = [\boldsymbol{E}'][\boldsymbol{E}]^{-1}\{\boldsymbol{\theta}\} \tag{2.144}$$

To calculate $\{\hat{\boldsymbol{b}}^{t2}\}$, the tensor of γ_{ij} must be added to the previous Equation:

$$\{\hat{\boldsymbol{b}}^{t2}\} = [\boldsymbol{\Gamma}][\boldsymbol{E}'][\boldsymbol{E}]^{-1}\{\boldsymbol{\theta}\} \tag{2.145}$$

Combining Equations 2.145, 2.141, and 2.140 into 2.138, it can be fully explicited as:

$$[\boldsymbol{H}]\{\boldsymbol{u}\} = [\boldsymbol{G}]\{\boldsymbol{t}\} + \{\boldsymbol{b}^{t1}\} + \left([\boldsymbol{H}][\hat{\boldsymbol{U}}] - [\boldsymbol{G}][\hat{\boldsymbol{T}}]\right)[\boldsymbol{F}]^{-1}\left(-\{\hat{\boldsymbol{b}}^{el}\} + [\Gamma][\boldsymbol{E}'][\boldsymbol{E}]^{-1}\{\boldsymbol{\theta}\}\right) \tag{2.146}$$

Equation 2.146 is the matrix form of Equation 2.77, where $[\boldsymbol{H}]$ and $[\boldsymbol{G}]$ are the well-known matrices of coefficients related to the boundary values $\{\boldsymbol{u}\}$ and $\{\boldsymbol{t}\}$. All other values are known and will reduce to a single vector, as follows:

$$\{\boldsymbol{b}\} = \{\boldsymbol{b}^{t1}\} + \left([\boldsymbol{H}][\hat{\boldsymbol{U}}] - [\boldsymbol{G}][\hat{\boldsymbol{T}}]\right)[\boldsymbol{F}]^{-1}\left(-\{\hat{\boldsymbol{b}}^{el}\} + [\Gamma][\boldsymbol{E}'][\boldsymbol{E}]^{-1}\{\boldsymbol{\theta}\}\right) \tag{2.147}$$

This allows Equation 2.138 be written as

$$[\boldsymbol{H}]\{\boldsymbol{u}\} = [\boldsymbol{G}]\{\boldsymbol{t}\} + \{\boldsymbol{b}\} \tag{2.148}$$

Equation 2.146 also shows that uncoupled thermoelastic formulation with volume integral being computed by DRM dismisses computation of temperature gradient field in potential formulation since it is approximated by temperature field and derivatives of RBF.

To generate a linear system of equations to evaluate boundary values, columns of $[\boldsymbol{H}]$ and $[\boldsymbol{G}]$ are changed so that $[\boldsymbol{G}]$ remains only with coefficients related to nodal points with prescribed boundary conditions, being renamed as $[\bar{\boldsymbol{G}}]$, while $[\boldsymbol{H}]$ remains with the coefficients associated to unknown nodal values, and it is renamed as $[\boldsymbol{A}]$. Vector $\{\boldsymbol{t}\}$ becomes $\{\bar{\boldsymbol{x}}\}$ with all boundary conditions values, $\{\boldsymbol{u}\}$ turns into $\{\boldsymbol{x}\}$ which are the unknown nodal values to be calculated. Then, Equation 2.146 can be written as:

$$[\boldsymbol{A}]\{\boldsymbol{x}\} = [\bar{\boldsymbol{G}}]\{\bar{\boldsymbol{x}}\} + \{\boldsymbol{b}\} \tag{2.149}$$

To simplify this Equation, let $\{\boldsymbol{B}\}$ be the vector of known values:

$$\{\boldsymbol{B}\} = [\bar{\boldsymbol{G}}]\{\bar{\boldsymbol{x}}\} + \{\boldsymbol{b}\} \tag{2.150}$$

Finally, the following linear system is solved for $\{\boldsymbol{x}\}$:

$$[\boldsymbol{A}]\{\boldsymbol{x}\} = \{\boldsymbol{B}\} \tag{2.151}$$

2.7 Subregions

The Boundary Integral Equation 2.17 is evaluated through the entire domain. If different materials are used in a single body, like in a bimetallic shell, the different properties produce different values for the fundamental solutions. There are formulations developed to deal with variable properties along the domain, but they are outside the scope of this work. So, in order to solve problems of this nature, the domain is divided into subregions, each one with constant material properties values.

For simplicity, consider the 2D domain subdivided into three regions given in Figure 2.7 (the concepts exposed in this section are also valid for 3D domains). Each subregion interfaces with the other two. The Equation 2.17 is valid inside each subdomain, and then, the integration is solved for each of them. So, each subregion generates a matricial equation like Equation 2.148, which can be given by the Equations 2.152 to 2.154:

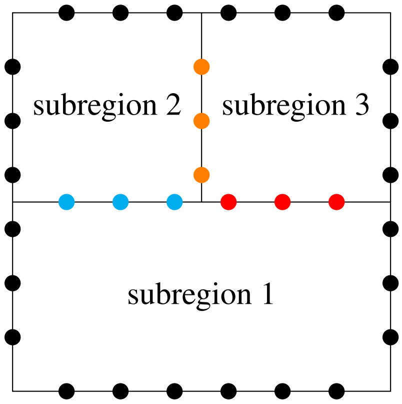

Figure 2.7 – Domain divided into subregions and nodes at boundary and interfaces.

$$[\boldsymbol{H}^1]\{\boldsymbol{u}^1\} = [\boldsymbol{G}^1]\{\boldsymbol{t}^1\} + \{\boldsymbol{b}^1\} \tag{2.152}$$

$$[\boldsymbol{H}^2]\{\boldsymbol{u}^2\} = [\boldsymbol{G}^2]\{\boldsymbol{t}^2\} + \{\boldsymbol{b}^2\} \tag{2.153}$$

$$[\boldsymbol{H}^3]\{\boldsymbol{u}^3\} = [\boldsymbol{G}^3]\{\boldsymbol{t}^3\} + \{\boldsymbol{b}^3\} \tag{2.154}$$

where the superscript denotes the subregion index. These equations form a matrix system of equations given by:

$$\begin{bmatrix} [\boldsymbol{H}^1] & 0 & 0 \\ 0 & [\boldsymbol{H}^2] & 0 \\ 0 & 0 & [\boldsymbol{H}^3] \end{bmatrix} \begin{Bmatrix} \{\boldsymbol{u}^1\} \\ \{\boldsymbol{u}^2\} \\ \{\boldsymbol{u}^3\} \end{Bmatrix} = \begin{bmatrix} [\boldsymbol{G}^1] & 0 & 0 \\ 0 & [\boldsymbol{G}^2] & 0 \\ 0 & 0 & [\boldsymbol{G}^3] \end{bmatrix} \begin{Bmatrix} \{\boldsymbol{t}^1\} \\ \{\boldsymbol{t}^2\} \\ \{\boldsymbol{t}^3\} \end{Bmatrix} + \begin{Bmatrix} \{\boldsymbol{b}^1\} \\ \{\boldsymbol{b}^2\} \\ \{\boldsymbol{b}^3\} \end{Bmatrix} \tag{2.155}$$

On a single region formulation, there is always a boundary condition known at each portion of the boundary, either a Dirichlet or a Neumann condition. On the other hand, at the interfaces, neither of them is known, increasing the amount of unknown values, and requiring more equations to solve the linear system. Moreover, Equation 2.155 shows that the regions are decoupled, showing no interdependence, as if they were separate and independent bodies.

In order to solve these matters, it is necessary to recall the colored nodes of Figure 2.7, placed at the subregions interfaces, representing a pair of coincident nodes belonging to two different regions. At these nodes, the continuity and the compatibility conditions apply. For the elasticity, the first condition establishes that the displacement at the coincident nodes must be equal (Kane, 1994):

$$\{\boldsymbol{u}^a_{ab}\} = \{\boldsymbol{u}^b_{ab}\} \tag{2.156}$$

where the superscripts mean the region to which the node belongs, and the subscripts mean the indexes of the two regions at the interface. This meaning will be followed until the end of this Section.

The continuity condition guarantees the integrity of the body, while the compatibility condition is a consequence of Newton's third law: each subregion can be seen as a single body and the action from the region *a* over the region *b* is followed by a reaction of the region *b* over the region *a*, of same intensity, and opposite direction. Mathematically:

$$\{\boldsymbol{t}^a_{ab}\} = \{-\boldsymbol{t}^b_{ab}\} \tag{2.157}$$

With the use of Equations 2.156 and 2.157, the subregions become now coupled. Also, they are used to reorder Equation 2.155, by considering that the submatrix $[\boldsymbol{H}^1]$ can be written as:

$$[\boldsymbol{H}^1] = \left[\begin{array}{ccc} [\boldsymbol{H}^1_{11}] & [\boldsymbol{H}^1_{12}] & [\boldsymbol{H}^1_{13}] \end{array} \right] \tag{2.158}$$

The submatrix $[\boldsymbol{H}^1_{11}]$ has the coefficients related to the black nodes in Figure 2.7 (nodes at the boundary of the subregion 1), while $[\boldsymbol{H}^1_{12}]$ are the coefficients related to the blue nodes at the interface of regions 1 and 2, and $[\boldsymbol{H}^1_{13}]$ concerns the coefficients of the red nodes at the interface of the regions 1 and 3. In other words, the values related to the nodes at the boundary and the same interface are placed together.

As a natural consequence, the subvector $\{\boldsymbol{u}^1\}$ becomes:

$$\{\boldsymbol{u}^1\} = \left\{ \begin{array}{c} \{\boldsymbol{u}^1_{11}\} \\ \{\boldsymbol{u}^1_{12}\} \\ \{\boldsymbol{u}^1_{13}\} \end{array} \right\} \tag{2.159}$$

The same organization is applied to regions 2 and 3:

$$[\boldsymbol{H}^2] = \left[\begin{array}{ccc} [\boldsymbol{H}^2_{12}] & [\boldsymbol{H}^2_{22}] & [\boldsymbol{H}^2_{23}] \end{array} \right] \tag{2.160}$$

$$\{\boldsymbol{u}^2\} = \left\{ \begin{array}{c} \{\boldsymbol{u}^2_{12}\} \\ \{\boldsymbol{u}^2_{22}\} \\ \{\boldsymbol{u}^2_{23}\} \end{array} \right\} \tag{2.161}$$

$$[\boldsymbol{H}^3] = \left[\begin{array}{ccc} [\boldsymbol{H}^3_{13}] & [\boldsymbol{H}^3_{23}] & [\boldsymbol{H}^3_{33}] \end{array} \right] \tag{2.162}$$

$$\{\boldsymbol{u}^3\} = \left\{ \begin{array}{c} \{\boldsymbol{u}^3_{13}\} \\ \{\boldsymbol{u}^3_{23}\} \\ \{\boldsymbol{u}^3_{33}\} \end{array} \right\} \tag{2.163}$$

Analogous results are achieved applying this concept to the submatrices $[\boldsymbol{G}^1]$, $[\boldsymbol{G}^2]$, and $[\boldsymbol{G}^3]$, and subvectors $\{\boldsymbol{t}^1\}$, $\{\boldsymbol{t}^2\}$, $\{\boldsymbol{t}^3\}$, $\{\boldsymbol{b}^1\}$, $\{\boldsymbol{b}^2\}$, and $\{\boldsymbol{b}^3\}$:

$$[\boldsymbol{G}^1] = \left[\begin{array}{ccc} [\boldsymbol{G}^1_{11}] & [\boldsymbol{G}^1_{12}] & [\boldsymbol{G}^1_{13}] \end{array} \right] \tag{2.164}$$

$$[\boldsymbol{G}^2] = \left[\begin{array}{ccc} [\boldsymbol{G}^2_{12}] & [\boldsymbol{G}^2_{22}] & [\boldsymbol{G}^2_{23}] \end{array} \right] \tag{2.165}$$

$$[\boldsymbol{G}^3] = \left[\begin{array}{ccc} [\boldsymbol{G}^3_{13}] & [\boldsymbol{G}^3_{23}] & [\boldsymbol{G}^3_{33}] \end{array} \right] \tag{2.166}$$

$$\{\boldsymbol{t}^1\} = \left\{ \begin{array}{c} \{\boldsymbol{t}^1_{11}\} \\ \{\boldsymbol{t}^1_{12}\} \\ \{\boldsymbol{t}^1_{13}\} \end{array} \right\} \tag{2.167}$$

$$\{\boldsymbol{t}^2\} = \left\{ \begin{array}{c} \{\boldsymbol{t}^2_{12}\} \\ \{\boldsymbol{t}^2_{22}\} \\ \{\boldsymbol{t}^2_{23}\} \end{array} \right\} \tag{2.168}$$

$$\{\boldsymbol{t}^3\} = \left\{ \begin{array}{c} \{\boldsymbol{t}^3_{13}\} \\ \{\boldsymbol{t}^3_{23}\} \\ \{\boldsymbol{t}^3_{33}\} \end{array} \right\} \tag{2.169}$$

$$\{\boldsymbol{b}^1\} = \left\{ \begin{array}{c} \{\boldsymbol{b}^1_{11}\} \\ \{\boldsymbol{b}^1_{12}\} \\ \{\boldsymbol{b}^1_{13}\} \end{array} \right\} \tag{2.170}$$

$$\{\boldsymbol{b}^2\} = \left\{ \begin{array}{c} \{\boldsymbol{b}^2_{12}\} \\ \{\boldsymbol{b}^2_{22}\} \\ \{\boldsymbol{b}^2_{23}\} \end{array} \right\} \tag{2.171}$$

$$\{\boldsymbol{b}^3\} = \left\{ \begin{array}{c} \{\boldsymbol{b}^3_{13}\} \\ \{\boldsymbol{b}^3_{23}\} \\ \{\boldsymbol{b}^3_{33}\} \end{array} \right\} \tag{2.172}$$

Now, Equation 2.155 can be explicited as:

$$\begin{aligned}
&\begin{bmatrix} [\boldsymbol{H}^1_{11}] & [\boldsymbol{H}^1_{12}] & [\boldsymbol{H}^1_{13}] & 0 & 0 & 0 & 0 & 0 & 0 \\ 0 & 0 & 0 & [\boldsymbol{H}^2_{12}] & [\boldsymbol{H}^2_{22}] & [\boldsymbol{H}^2_{23}] & 0 & 0 & 0 \\ 0 & 0 & 0 & 0 & 0 & 0 & [\boldsymbol{H}^3_{13}] & [\boldsymbol{H}^3_{23}] & [\boldsymbol{H}^3_{33}] \end{bmatrix} \left\{ \begin{array}{c} \{\boldsymbol{u}^1_{11}\} \\ \{\boldsymbol{u}^1_{12}\} \\ \{\boldsymbol{u}^1_{13}\} \\ \{\boldsymbol{u}^2_{12}\} \\ \{\boldsymbol{u}^2_{22}\} \\ \{\boldsymbol{u}^2_{23}\} \\ \{\boldsymbol{u}^3_{13}\} \\ \{\boldsymbol{u}^3_{23}\} \\ \{\boldsymbol{u}^3_{33}\} \end{array} \right\} \\
=& \\
&\begin{bmatrix} [\boldsymbol{G}^1_{11}] & [\boldsymbol{G}^1_{12}] & [\boldsymbol{G}^1_{13}] & 0 & 0 & 0 & 0 & 0 & 0 \\ 0 & 0 & 0 & [\boldsymbol{G}^2_{12}] & [\boldsymbol{G}^2_{22}] & [\boldsymbol{G}^2_{23}] & 0 & 0 & 0 \\ 0 & 0 & 0 & 0 & 0 & 0 & [\boldsymbol{G}^3_{13}] & [\boldsymbol{G}^3_{23}] & [\boldsymbol{G}^3_{33}] \end{bmatrix} \left\{ \begin{array}{c} \{\boldsymbol{t}^1_{11}\} \\ \{\boldsymbol{t}^1_{12}\} \\ \{\boldsymbol{t}^1_{13}\} \\ \{\boldsymbol{t}^2_{12}\} \\ \{\boldsymbol{t}^2_{22}\} \\ \{\boldsymbol{t}^2_{23}\} \\ \{\boldsymbol{t}^3_{13}\} \\ \{\boldsymbol{t}^3_{23}\} \\ \{\boldsymbol{t}^3_{33}\} \end{array} \right\} \\
&+ \left\{ \begin{array}{c} \{\boldsymbol{b}^1_{11}\} \\ \{\boldsymbol{b}^1_{12}\} \\ \{\boldsymbol{b}^1_{13}\} \\ \{\boldsymbol{b}^2_{12}\} \\ \{\boldsymbol{b}^2_{22}\} \\ \{\boldsymbol{b}^2_{23}\} \\ \{\boldsymbol{b}^3_{13}\} \\ \{\boldsymbol{b}^3_{23}\} \\ \{\boldsymbol{b}^3_{33}\} \end{array} \right\}
\end{aligned} \tag{2.173}$$

The Equations 2.156 and 2.157 allow to combine the unknown values at the interfaces, avoiding the increase of the order of the system of equations represented by Equation 2.173. For better organization, the traction values at the interfaces are all unknown and are moved to the left-hand side of the Equation 2.173:

$$\begin{bmatrix} [\boldsymbol{H}^1_{11}] & [\boldsymbol{H}^1_{12}] & [\boldsymbol{H}^1_{13}] & -[\boldsymbol{G}^1_{12}] & 0 & 0 & -[\boldsymbol{G}^1_{13}] & 0 & 0 \\ 0 & [\boldsymbol{H}^2_{12}] & 0 & [\boldsymbol{G}^2_{12}] & [\boldsymbol{H}^2_{22}] & [\boldsymbol{H}^2_{23}] & [\boldsymbol{G}^3_{13}] & -[\boldsymbol{G}^2_{23}] & 0 \\ 0 & 0 & [\boldsymbol{H}^3_{13}] & 0 & 0 & [\boldsymbol{H}^3_{23}] & 0 & -[\boldsymbol{G}^3_{23}] & [\boldsymbol{H}^3_{33}] \end{bmatrix} \begin{Bmatrix} \{\boldsymbol{u}^1_{11}\} \\ \{\boldsymbol{u}^1_{12}\} \\ \{\boldsymbol{u}^1_{13}\} \\ \{\boldsymbol{t}^2_{12}\} \\ \{\boldsymbol{u}^2_{22}\} \\ \{\boldsymbol{u}^2_{23}\} \\ \{\boldsymbol{t}^3_{13}\} \\ \{\boldsymbol{t}^3_{23}\} \\ \{\boldsymbol{u}^3_{33}\} \end{Bmatrix}$$

$$= \begin{bmatrix} [\boldsymbol{G}^1_{11}] & 0 & 0 & 0 & 0 & 0 & 0 & 0 & 0 \\ 0 & 0 & 0 & 0 & [\boldsymbol{G}^2_{22}] & 0 & 0 & 0 & 0 \\ 0 & 0 & 0 & 0 & 0 & 0 & 0 & 0 & [\boldsymbol{G}^3_{33}] \end{bmatrix} \begin{Bmatrix} \{\boldsymbol{t}^1_{11}\} \\ 0 \\ 0 \\ 0 \\ \{\boldsymbol{t}^2_{22}\} \\ 0 \\ 0 \\ 0 \\ \{\boldsymbol{t}^3_{33}\} \end{Bmatrix} + \begin{Bmatrix} \{\boldsymbol{b}^1_{11}\} \\ \{\boldsymbol{b}^1_{12}\} \\ \{\boldsymbol{b}^1_{13}\} \\ \{\boldsymbol{b}^2_{12}\} \\ \{\boldsymbol{b}^2_{22}\} \\ \{\boldsymbol{b}^2_{23}\} \\ \{\boldsymbol{b}^3_{13}\} \\ \{\boldsymbol{b}^3_{23}\} \\ \{\boldsymbol{b}^3_{33}\} \end{Bmatrix} \tag{2.174}$$

Finally, applying the boundary conditions to the Equation 2.174, the columns of submatrices $[\boldsymbol{H}^a_{aa}]$ and $[\boldsymbol{G}^a_{aa}]$ are changed in order to have only boundary known values at the subvectors $\{\boldsymbol{t}^a_{aa}\}$ and the coefficients related to them at the submatrices $[\boldsymbol{G}^a_{aa}]$. Then, the right-hand side of Equation 2.174 takes the form of Equation 2.149, being solved for the unknown values of the variables.

The use of the subregions can be quite advantageous for the Boundary Elements Method. The interfaces add elements to the mesh but reduce the number of elements of each region. Considering meshes of the same refinement degree, the total time required to compute the integral of the BIE (Equation 2.17) may reduce, depending on how the body is subdivided, since the fundamental solution for each source point is integrated over a smaller number of elements.

Another consequence of the subregions is clearly shown in Equation 2.174: the matrices become sparse. Then, the right-hand side can take advantage by multiplying less amount of numbers, and the left-hand side can take advantage of the sparse linear system solver methods. The MUMPS solver used at BESLE is particularly strong at this point, reducing the time to solve the linear system by operating only with the non-zero values.

2.8 Boundary Stresses and Strains

Solution of Equation 2.149 results in displacements and tractions known at all boundary nodes and constitute the set of primary response. Stresses and strains are the secondary responses calculated using the primary response. Kane (1994) transforms the global values of primary response calculated in global x_i coordinates to a local normal and tangential coordinate system for each node, and then, calculates stresses and strains in this local system, finally transforming the results to the global system. But Kane (1994) also presents a matricial formulation for 3D problems that dismiss coordinate transformations, and it is already implemented in BESLE. Consider Hooke's Law without thermal effects:

$$\sigma_{ij} = C_{ijkl}\epsilon_{kl} \tag{2.175}$$

With the aid of Equation 2.5, Hooke's law is explicited as:

$$\sigma_{ij} = C_{ijkl}\left[\frac{1}{2}(u_{k,l} + u_{l,k})\right] \tag{2.176}$$

It is important to note that tensor C_{ijkl} is symmetrical, what means:

$$C_{ijkl} = C_{jikl} = C_{ijlk} = C_{klji} \tag{2.177}$$

This allows the reduction of this fourth-order tensor to a simpler second-rank tensor C_{mn} combining the pair of indices ij and kl using Voigt notation, as shown in Table 2.3. Then, Equation 2.176 is written in matricial form:

Table 2.3 – Combination of indices for Voigt notation.

ij or kl	m or n
11	1
22	2
33	3
23	4
13	5
12	6

$$\begin{Bmatrix} \sigma_{11} \\ \sigma_{22} \\ \sigma_{33} \\ \sigma_{23} \\ \sigma_{13} \\ \sigma_{12} \end{Bmatrix} = \begin{bmatrix} C_{11} & C_{12} & C_{13} & 0.5C_{14} & 0.5C_{14} & 0.5C_{15} & 0.5C_{15} & 0.5C_{16} & 0.5C_{16} \\ C_{12} & C_{22} & C_{23} & 0.5C_{14} & 0.5C_{24} & 0.5C_{25} & 0.5C_{25} & 0.5C_{26} & 0.5C_{26} \\ C_{13} & C_{23} & C_{33} & 0.5C_{14} & 0.5C_{34} & 0.5C_{35} & 0.5C_{35} & 0.5C_{36} & 0.5C_{36} \\ C_{14} & C_{24} & C_{34} & 0.5C_{14} & 0.5C_{44} & 0.5C_{45} & 0.5C_{45} & 0.5C_{46} & 0.5C_{46} \\ C_{15} & C_{25} & C_{35} & 0.5C_{14} & 0.5C_{54} & 0.5C_{55} & 0.5C_{55} & 0.5C_{56} & 0.5C_{56} \\ C_{16} & C_{26} & C_{36} & 0.5C_{14} & 0.5C_{64} & 0.5C_{65} & 0.5C_{65} & 0.5C_{66} & 0.5C_{66} \end{bmatrix} \begin{Bmatrix} u_{1,1} \\ u_{2,2} \\ u_{3,3} \\ u_{2,3} \\ u_{3,2} \\ u_{1,3} \\ u_{3,1} \\ u_{1,2} \\ u_{2,1} \end{Bmatrix} \tag{2.178}$$

Boundary tractions are given by $t_i = \sigma_{ij} n_j$, or in matrix form:

$$\begin{Bmatrix} t_1 \\ t_2 \\ t_3 \end{Bmatrix} = \begin{bmatrix} \sigma_{11} & \sigma_{12} & \sigma_{13} \\ \sigma_{21} & \sigma_{22} & \sigma_{23} \\ \sigma_{31} & \sigma_{32} & \sigma_{33} \end{bmatrix} \begin{Bmatrix} n_1 \\ n_2 \\ n_3 \end{Bmatrix} \tag{2.179}$$

And displacements derivatives of Equation 2.178 can be written in terms of intrinsic element coordinates:

$$\begin{Bmatrix} u_{1,\eta_1} \\ u_{2,\eta_1} \\ u_{3,\eta_1} \end{Bmatrix} = \begin{bmatrix} u_{1,1} & u_{1,2} & u_{1,3} \\ u_{2,1} & u_{2,2} & u_{2,3} \\ u_{3,1} & u_{3,2} & u_{3,3} \end{bmatrix} \begin{Bmatrix} x_{1,\eta_1} \\ x_{2,\eta_1} \\ x_{3,\eta_1} \end{Bmatrix} \tag{2.180}$$

$$\begin{Bmatrix} u_{1,\eta_2} \\ u_{2,\eta_2} \\ u_{3,\eta_2} \end{Bmatrix} = \begin{bmatrix} u_{1,1} & u_{1,2} & u_{1,3} \\ u_{2,1} & u_{2,2} & u_{2,3} \\ u_{3,1} & u_{3,2} & u_{3,3} \end{bmatrix} \begin{Bmatrix} x_{1,\eta_2} \\ x_{2,\eta_2} \\ x_{3,\eta_2} \end{Bmatrix} \tag{2.181}$$

with u_{i,η_1} being calculated by:

$$u_{i,\eta_1} = \sum_{m=1}^{3} \frac{\partial N^{(m)}}{\partial \eta_1} u_i^{(m)} \tag{2.182}$$

where $\frac{\partial N^{(m)}}{\partial \eta_1}$ are the derivatives of discontinuous shape functions with respect to η_1 and $u_i^{(m)}$ are the displacements at each element node, with index i meaning cartesian coordinate. Same idea applies to calculate x_{i,η_1}:

$$x_{i,\eta_1} = \sum_{m=1}^{3} \frac{\partial N^{(m)}}{\partial \eta_1} x_i^{(m)} \tag{2.183}$$

Derivatives u_{i,η_2} and x_{i,η_2} are obtained by repeating the derivatives just done, but with respect to η_2. By doing this, Equations 2.178, 2.179, 2.180, and 2.181 form a system of 15 equations with σ_{ij} and $u_{i,j}$ as unknowns. This matricial system can be mounted with a series of submatrices as:

$$\begin{bmatrix} [\boldsymbol{I}]_{6\times6} & [\boldsymbol{C}]_{6\times9} \\ [\boldsymbol{N}]_{3\times6} & [\mathbf{0}]_{3\times9} \\ [\mathbf{0}]_{6\times6} & [\boldsymbol{D}]_{6\times9} \end{bmatrix} \left\{ \begin{array}{c} \{\boldsymbol{\sigma}\}_{6\times1} \\ \{\boldsymbol{\nabla}_a \boldsymbol{x}\}_{9\times1} \end{array} \right\} = \left\{ \begin{array}{c} \{\mathbf{0}\}_{6\times1} \\ \{\boldsymbol{t}\}_{3\times1} \\ \{\boldsymbol{\nabla}_a \boldsymbol{u}\}_{6\times1} \end{array} \right\} \tag{2.184}$$

where $[\boldsymbol{I}]$ is identity matrix, $[\mathbf{0}]$ are null matrices and $\{\mathbf{0}\}$ is a null vector. Also:

$$[\boldsymbol{C}] = \begin{bmatrix} -C_{11} & -C_{12} & -C_{13} & -0.5C_{14} & -0.5C_{14} & -0.5C_{15} & -0.5C_{15} & -0.5C_{16} & -0.5C_{16} \\ -C_{12} & -C_{22} & -C_{23} & -0.5C_{14} & -0.5C_{24} & -0.5C_{25} & -0.5C_{25} & -0.5C_{26} & -0.5C_{26} \\ -C_{13} & -C_{23} & -C_{33} & -0.5C_{14} & -0.5C_{34} & -0.5C_{35} & -0.5C_{35} & -0.5C_{36} & -0.5C_{36} \\ -C_{14} & -C_{24} & -C_{34} & -0.5C_{14} & -0.5C_{44} & -0.5C_{45} & -0.5C_{45} & -0.5C_{46} & -0.5C_{46} \\ -C_{15} & -C_{25} & -C_{35} & -0.5C_{14} & -0.5C_{54} & -0.5C_{55} & -0.5C_{55} & -0.5C_{56} & -0.5C_{56} \\ -C_{16} & -C_{26} & -C_{36} & -0.5C_{14} & -0.5C_{64} & -0.5C_{65} & -0.5C_{65} & -0.5C_{66} & -0.5C_{66} \end{bmatrix} \tag{2.185}$$

$$[\boldsymbol{N}] = \begin{bmatrix} n_1 & 0 & 0 & 0 & n_3 & n_2 \\ 0 & n_2 & 0 & n_3 & 0 & n_1 \\ 0 & 0 & n_3 & n_2 & n_1 & 0 \end{bmatrix} \tag{2.186}$$

$$[\boldsymbol{D}] = \begin{bmatrix} x_{1,\xi} & 0 & 0 & 0 & 0 & x_{3,\eta_1} & 0 & x_{2,\eta_1} & 0 \\ 0 & x_{2,\eta_1} & 0 & x_{3,\eta_1} & 0 & 0 & 0 & 0 & x_{1,\eta_1} \\ 0 & 0 & x_{3,\eta_1} & 0 & x_{2,\eta_1} & 0 & x_{1,\eta_1} & 0 & 0 \\ x_{1,\eta_2} & 0 & 0 & 0 & 0 & x_{3,\eta_2} & 0 & x_{2,\eta_2} & 0 \\ 0 & x_{2,\eta_2} & 0 & x_{3,\eta_2} & 0 & 0 & 0 & 0 & x_{1,\eta_2} \\ 0 & 0 & x_{3,\eta_2} & 0 & x_{2,\eta_2} & 0 & x_{1,\eta_2} & 0 & 0 \end{bmatrix} \tag{2.187}$$

$$\{\boldsymbol{t}\} = \{\ t_1 \quad t_2 \quad t_3\ \}^T \tag{2.188}$$

$$\{\boldsymbol{\nabla}_a \boldsymbol{u}\} = \{\ u_{1,\eta_1} \quad u_{2,\eta_1} \quad u_{3,\eta_1} \quad u_{1,\eta_2} \quad u_{2,\eta_2} \quad u_{3,\eta_2}\ \}^T \tag{2.189}$$

$$\{\boldsymbol{\nabla}_a\boldsymbol{x}\} = \{\ u_{1,1} \quad u_{2,2} \quad u_{3,3} \quad u_{2,3} \quad u_{3,2} \quad u_{1,3} \quad u_{3,1} \quad u_{1,2} \quad u_{2,1}\ \}^T \tag{2.190}$$

Stresses are obtained directly from Equation 2.184 while strains are calculated by equation 2.5 using the derivatives calculated in equation 2.184.

To consider the thermal effect, one may observe that only Hooke's law changes, as given by Equation 2.1. So, the only change in Equation 2.184 would be the substitution of the null vector on the right-hand side by a thermal vector effect:

$$\{\boldsymbol{bt}\} = \{\ -\gamma_{11}\theta \quad -\gamma_{22}\theta \quad -\gamma_{33}\theta \quad -\gamma_{23}\theta \quad -\gamma_{13}\theta \quad -\gamma_{12}\theta\ \}^T \tag{2.191}$$

and the system becomes:

$$\begin{bmatrix} [\boldsymbol{I}]_{6\times 6} & [\boldsymbol{C}]_{6\times 9} \\ [\boldsymbol{N}]_{3\times 6} & [\boldsymbol{0}]_{3\times 9} \\ [\boldsymbol{0}]_{6\times 6} & [\boldsymbol{D}]_{6\times 9} \end{bmatrix} \left\{ \begin{array}{c} \{\boldsymbol{\sigma}\}_{6\times 1} \\ \{\boldsymbol{\nabla}_a\boldsymbol{x}\}_{9\times 1} \end{array} \right\} = \left\{ \begin{array}{c} \{\boldsymbol{bt}\}_{6\times 1} \\ \{\boldsymbol{t}\}_{3\times 1} \\ \{\boldsymbol{\nabla}_a\boldsymbol{u}\}_{6\times 1} \end{array} \right\} \tag{2.192}$$

3 POTENTIAL BOUNDARY ELEMENT METHOD

3.1 Introduction

As shown in Chapter 2, it is necessary to know the temperature at nodal points to use thermoelastic formulation. In some situations, it may be a known value or known function through the entire domain. This may be more useful in cases in which an analytical solution is possible for validating codes (Gao, 2003) or some experiments with a controlled environment. So, a routine was implemented in BESLE to calculate the potential field as a function of cartesian coordinates.

Nevertheless, the temperature field may be unknown and it is necessary to solve the potential problem. For this reason, the potential formulation of Boundary Elements for tridimensional isotropic materials is described in this chapter. For anisotropic materials, it is used the general technique named Direct Domain Mapping (DDM), developed by Shiah and Tan (1997) for bidimensional problems, being extended for tridimensional domains (Shiah; Tan, 2004) and multiregions (Shiah *et al.*, 2006).

The 3D isotropic potential solver was implemented in BESLE together with a tool to make DDM calculations for any anisotropic material.

3.2 Potential Boundary Integral Equation

The temperature field problem is governed by Laplace equation (Brebbia; Dominguez, 1992) which may be written in indicial notation as:

$$u_{,ii} = 0 \tag{3.1}$$

Using the Weighted Residual Method, it is integrated with an interpolation function u^* also known as the fundamental solution:

$$\int_\Omega u_{,ii} u^* d\Omega = 0 \tag{3.2}$$

Using the Divergence theorem and integrating by parts, the inverse integral statement is obtained:

$$\int_\Omega u u^*_{,ii} d\Omega + \int_\Gamma u_{,i} u^* n_i d\Gamma - \int_\Gamma u u^*_{,i} n_i d\Gamma = 0 \tag{3.3}$$

where derivatives $u_{,i}$ and $u^*_{,i}$ combined with n_i (the normal vector at the boundary surface) represent the potential derivative and derivative of the fundamental solution at the normal direction, respectively. They can be rewritten as:

$$q = u_{,i} n_i \tag{3.4}$$

$$q^* = u^*_{,i} n_i \tag{3.5}$$

The fundamental solution for potential problems is analog of elasticity problems: a pontual thermal source action spreading its effects to the infinite. The fundamental solutions for 3D isotropic material presented by Brebbia and Dominguez (1992) are:

$$u^* = \frac{1}{4\pi r} \tag{3.6}$$

$$q^* = -\frac{1}{4\pi r^2} r_{,i} n_i \tag{3.7}$$

So, domain integral in Equation 3.3 is evaluated in the sense of Cauchy Principal Value, as it was done for elasticity, and can be solved as:

$$\int_\Omega u u^*_{,ii} d\Omega = c(\xi) u(\xi) \tag{3.8}$$

with $c(\xi) = 0.5$ for smooth boundaries and $c(\xi) = 1.0$ for points inside the domain. With these considerations, Equation 3.3 can be rewritten as:

$$c(\xi) u(\xi) + \int_\Gamma u q^* d\Gamma = \int_\Gamma q u^* d\Gamma \tag{3.9}$$

As it was done for elasticity, after discretization and integration the following matricial equation is generated:

$$[\boldsymbol{H}]\{\boldsymbol{u}\} = [\boldsymbol{G}]\{\boldsymbol{q}\} \tag{3.10}$$

with $[\boldsymbol{H}]$ being composed by integration over q^* plus $c(\xi)$ coefficients, and $[\boldsymbol{G}]$ contains results of integration over u^*. Vectors $\{\boldsymbol{u}\}$ and $\{\boldsymbol{q}\}$ represent the values of temperature and normal derivative at boundary nodes. After prescribing boundary conditions, columns of $[\boldsymbol{H}]$ and $[\boldsymbol{G}]$ are changed as it was explained for elasticity, generating the following system, solved for $\{\boldsymbol{x}\}$ which will contain boundary unknown values a priori.

$$[\boldsymbol{A}]\{\boldsymbol{x}\} = \{\boldsymbol{b}\} \tag{3.11}$$

Once the values at the boundary are calculated, Equation 3.9 is reused to calculate the temperature at points inside the domain region, just setting $c(\xi) = 1.0$. It turns into:

$$u(\xi) = \int_\Gamma q u^* d\Gamma - \int_\Gamma u q^* d\Gamma \tag{3.12}$$

No linear system is generated by Equation 3.12 since only $u(\xi)$ is unknown for each source point. For thermoelasticity, temperature evaluation is enough, so derivatives at internal points are not considered in this work.

3.3 Direct Domain Mapping

Anisotropic fundamental solutions for bidimensional potential problems are presented in Partridge *et al.* (1992). They are quite simple expressions but need some considerations for orthotropic cases since the Euclidean distance is weighted by conductivity properties, leading to nondegenerated expressions, leaving some singularity.

For three-dimensional problems, fundamental solutions are generally expressed employing transformations, like Fourier or Radon transforms (Marczak; Denda, 2011) or others (Clements; Budhi, 1999). Another approach is possible by rotating axes, rewriting the Boundary Integral Equation with respect to a rotated coordinate system, and transforming anisotropic problems into orthotropic ones (Banerjee; Lejeune, 1981), in which fundamental solutions are well established.

The technique proposed by Shiah and Tan (1997) applies a coordinate transformation over the geometry of an anisotropic problem, distorting it into an equivalent isotropic geometry. The coordinate system of this newly mapped plane remains the same, making it easy to adapt to isotropic existing codes. Figure 3.1 exemplifies DDM transformation for 2D geometry.

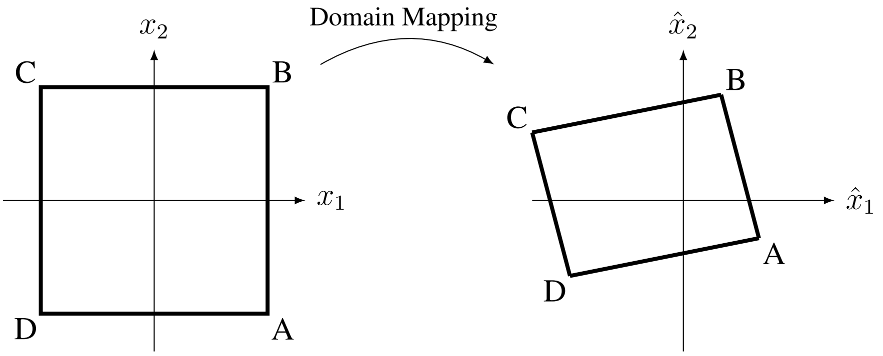

Figure 3.1 – Transforming real geometry (left) into mapped plane (right).

Once the mapped geometry is defined, it becomes an isotropic potential problem, being easily solved by the isotropic fundamental solution defined in Equations 3.6 and 3.7. All calculations are done considering the mapping domain and the results are returned to real geometry. Potential values are the same in both domains, but derivatives and fluxes need to be adjusted. The matrix transformation for geometry is given by (Shiah; Tan, 1997; Shiah; Tan, 2004):

$$[\boldsymbol{F}_{DDM}] = \begin{bmatrix} \sqrt{\Delta}/k_{11} & 0 & 0 \\ -k_{12}/k_{11} & 1 & 0 \\ \alpha & \beta & \gamma \end{bmatrix} \tag{3.13}$$

where

$$\Delta = k_{11}k_{22} - k_{12}^2 \tag{3.14}$$

$$\alpha = \frac{k_{12}k_{13} - k_{11}k_{23}}{\sqrt{\omega}} \tag{3.15}$$

$$\beta = \frac{k_{12}k_{23} - k_{22}k_{13}}{\sqrt{\omega}} \tag{3.16}$$

$$\gamma = \frac{\Delta}{\sqrt{\omega}} \tag{3.17}$$

$$\omega = k_{11}k_{33}\Delta - k_{11}k_{22}k_{13}^2 + 2k_{11}k_{12}k_{13}k_{23} - k_{11}^2k_{23}^2 \tag{3.18}$$

and k_{ij} are the components of the conductivity tensor. The transformation is done by:

$$\begin{Bmatrix} \hat{x}_1 \\ \hat{x}_2 \\ \hat{x}_3 \end{Bmatrix} = \begin{bmatrix} \sqrt{\Delta}/k_{11} & 0 & 0 \\ -k_{12}/k_{11} & 1 & 0 \\ \alpha & \beta & \gamma \end{bmatrix} \begin{Bmatrix} x_1 \\ x_2 \\ x_3 \end{Bmatrix} \tag{3.19}$$

After transforming the geometry, it is necessary to review the boundary conditions. Temperature is not affected, but the normal derivative has different values on the real and mapped domains. They are calculated by Equation 3.20.

$$\frac{du}{d\hat{n}} = \left(\frac{k_{11}}{\sqrt{\Delta}}\frac{\partial u}{\partial x_1} + \frac{k_{12}}{\sqrt{\Delta}}\frac{\partial u}{\partial x_2} - \frac{(k_{11}\alpha + k_{12}\beta)}{\gamma\sqrt{\Delta}}\frac{\partial u}{\partial x_3}\right)\hat{n}_1 + \left(\frac{\partial u}{\partial x_2} - \frac{\beta}{\gamma}\frac{\partial u}{\partial x_3}\right)\hat{n}_2 + \left(\frac{1}{\gamma}\frac{\partial u}{\partial x_3}\right)\hat{n}_3 \tag{3.20}$$

Expressions in parenthesis in Equation 3.20 are the coordinates of the normal vector of boundary conditions for the mapped domain. It can be observed that null values of flux for the real domain keep null values at the mapped domain.

To compute the potential values at internal nodes, Equation 3.12 is used with calculations done in the mapped domain.

3.4 Direct Domain Mapping for Subregions

The subregions method in the Boundary Elements requires continuity and compatibility conditions. For the potential problem, it means that coincident nodes of different regions at the interface must have equal temperature and the sum of their flux must be null. Mathematically,

$$u^{(1)} = u^{(2)} \tag{3.21}$$

$$q^{(1)} = -q^{(2)} \tag{3.22}$$

The superscripts indicate different regions. Remembering that the flux is calculated from normal derivative and considering an isotropic material, Equation 3.22 is written as

$$k^{(1)} \frac{\partial u^{(1)}}{\partial n^{(1)}} = -k^{(2)} \frac{\partial u^{(2)}}{\partial n^{(2)}} \tag{3.23}$$

with $k^{(i)}$ being the conduction coefficient of the i-th region.

When DDM is applied to multiple region material, the geometry will be mapped differently to each region and they will not coincide anymore, as shown in Figure 3.2. Then, the interfaces must be identified before geometry transformation on the real domain.

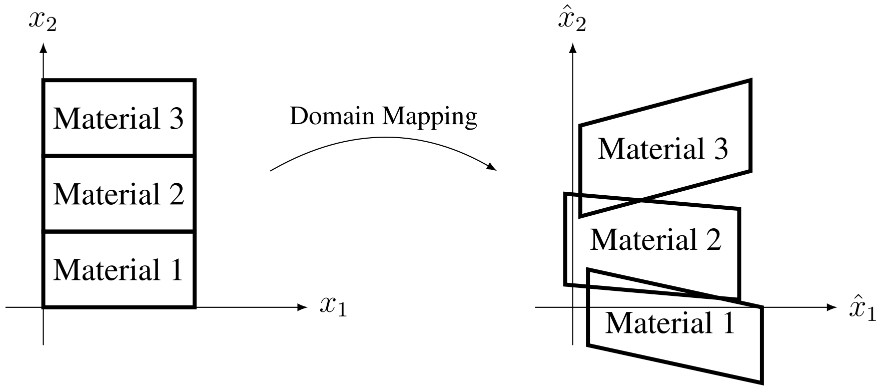

Figure 3.2 – Direct domain mapping of multiple anisotropic materials.

Since DDM does not affect the potential values, Equation 3.21 is still valid. For compatibility conditions, it is necessary to consider the mapping procedure using Equation 3.24 (Shiah *et al.*, 2006).

$$\left(\frac{\Delta^{(1)}}{\Omega^{(1)} k_{11}^{(1)}} \right) \frac{du^{(1)}}{d\hat{n}^{(1)}} = - \left(\frac{\Delta^{(2)}}{\Omega^{(2)} k_{11}^{(2)}} \right) \frac{du^{(2)}}{d\hat{n}^{(2)}} \tag{3.24}$$

with $\Delta^{(i)}$ given by Equation 3.14 and:

$$\Omega = \sqrt{\left(\hat{n}_1 \frac{\sqrt{\Delta}}{k_{11}} - \hat{n}_2 \frac{k_{12}}{k_{11}} + \hat{n}_3 \alpha \right)^2 + (\hat{n}_2 + \hat{n}_3 \beta)^2 + (\hat{n}_3 \gamma)^2} \tag{3.25}$$

Comparing Equations 3.23 and 3.24, the expression in parenthesis of the last one may be seen as an effective conduction coefficient for that direction and material. In other words, they play the role of an "equivalent conductive coefficient" of the isotropic case, allowing the calculation of the normal flux at a mapped domain using only mapped domain data.

Equation 3.24 is also valid for two-dimensional problems, by calculating the necessary coefficients considering null the third component of the outward normal vector. Another important consideration is that the third direction must be preserved, i.e., the mapping is not applied to it. This is obtained by writing tensor of Equation 3.13 as:

$$[\boldsymbol{F}_{DDM}] = \begin{bmatrix} \sqrt{\Delta}/k_{11} & 0 & 0 \\ -k_{12}/k_{11} & 1 & 0 \\ 0 & 0 & 1 \end{bmatrix} \tag{3.26}$$

It seems obvious that conductive properties k_{13} and k_{23} should be set as 0 making $\alpha = \beta = 0$ (see Equations 3.15 and 3.16). To obtain $\gamma = 1$, one needs, from Equation 3.17:

$$\Delta = \sqrt{\omega} \tag{3.27}$$

This results in:

$$k_{33} = k_{22} - \frac{k_{12}^2}{k_{11}} \tag{3.28}$$

It means that it is necessary to use a non-obvious value of k_{33} which is dependent on the properties at directions x_1 and x_2 to solve 2D anisotropic problems with a 3D formulation.

4 NUMERICAL EXAMPLES

4.1 Preliminary Considerations

This section presents numerical results in order to validate the proposed formulation developed throughout this work. Firstly, some potential problems are presented in order to validate the temperature solver implemented. Finally, thermoelastic problems are analyzed and the results are compared to the literature or with results obtained by the Finite Element Method.

For the problems with analytical solutions, the relative error for all nodes was calculated but it is presented the average relative error for various nodes of the geometry without boundary conditions prescribed (all nodes or selected ones). For the problems in which the reference was the results of the Finite Element Method, the term "difference" is used instead of "error". The difference in the nomenclature does not change the formulae of calculation.

Let y represent any physical variable of interest. Equation 4.1 is used to compute the relative error for each node, and Equation 4.2 computes the average relative error for various nodes. The value $max|y_{ref}|$ is the maximum absolute value of the physical variable, and it is used to avoid the division for numbers close to zero.

$$\epsilon = \frac{|y_{BESLE} - y_{ref}|}{max|y_{ref}|} \tag{4.1}$$

$$\bar{\epsilon} = \frac{1}{N}\sum_{i=1}^{N} \frac{|y_{BESLE} - y_{ref}|}{max|y_{ref}|} \tag{4.2}$$

where N is the number of points used in the analysis.

The BESLE results are exported to a **.vtk* file, a format in which Paraview software is able to read, plot, and manipulate the data. Paraview only plots the results at the geometrical nodes. So, BESLE interpolates the results calculated at the discontinuous nodes (physical) to the continuous nodes (geometrical).

Some BESLE results were compared with the Finite Element Method using the software ANSYS, Student version. Because of its mesh size limitation, it was not possible to create benchmark results with very refined meshes, being this the reason why the number of elements used at ANSYS was similar to the ones used at BESLE.

4.2 Potential validation

4.2.1 Isotropic cube

The first example is an isotropic cube with an edge of 1 unit length. The bottom face in Figure 4.1 has the temperature set $\theta = 0$ while its opposite face has temperature $\theta = 100$. All other faces are insulated, making this an unidimensional conduction problem with temperature solution $\theta = 100x_1$.

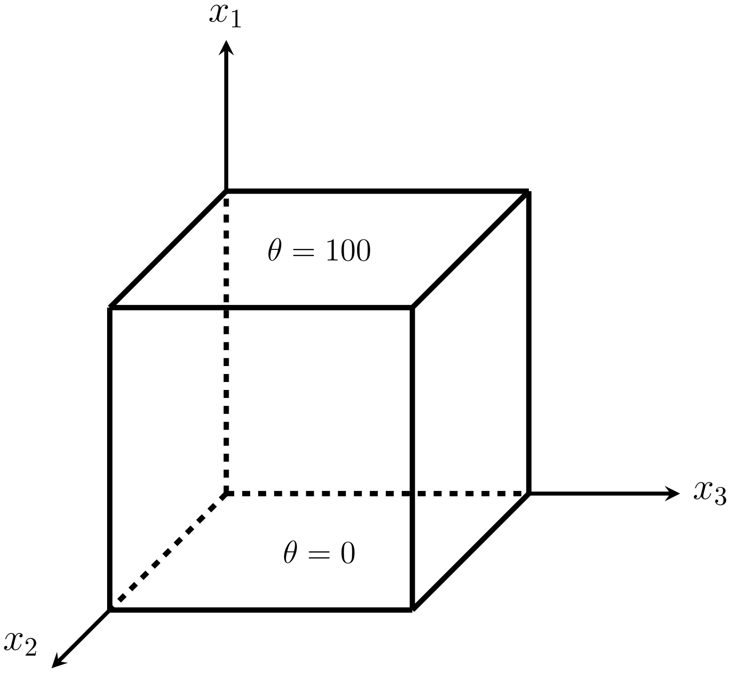

Figure 4.1 – Boundary conditions for the isotropic cube.

The average relative temperature error is calculated at each boundary node as well as the 512 domain points regularly spaced. Eleven different boundary meshes were tested (48, 108, 192, 300, 432, 588, 468, 972, 1200, 1452, and 1728 elements) and the average relative error of each mesh simulation was calculated and presented in Figure 4.2.

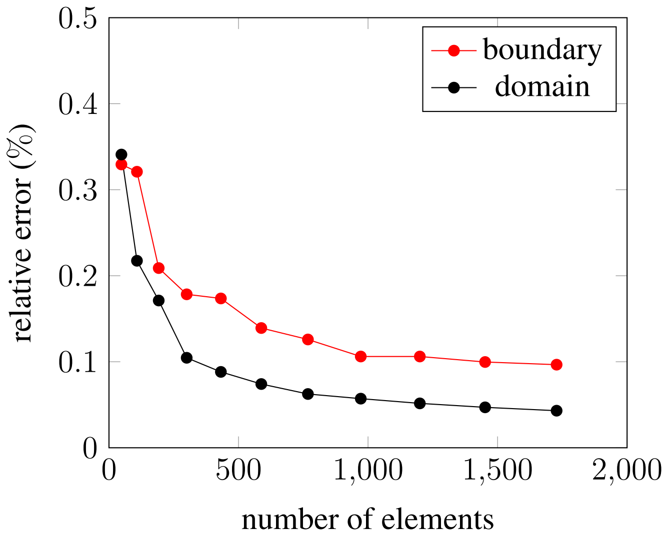

Figure 4.2 – Average relative temperature error for the isotropic cube at boundary and internal points.

Results show good agreement with the analytical solution and the accuracy increases with mesh refinement. As expected, domain values are better than boundary ones due to the reuse of integral formulation (Ramos, 2015).

4.2.2 Isotropic multiple region

Multiregion isotropic implementation is verified with the problem shown in Figure 4.3. Left region is composed of a material of conductivity $k^{(1)} = 1$ while right region has conductivity $k^{(2)} = 2$ (superscripts denotes region). The regions have the same size, with the temperature at the left face $\theta = 0$ while the right face is set $\theta = 100$. All other faces are insulated.

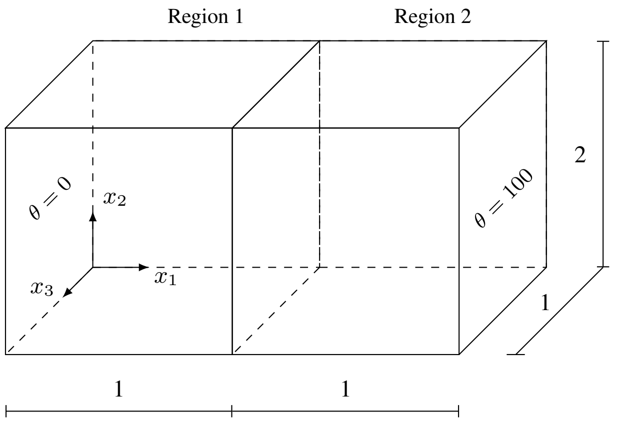

Figure 4.3 – The isotropic multiple region problem.

The analytical solution to this problem is (Gao, 2003):

$$T = \frac{200x_1}{3} \text{ , for } 0 \leq x_1 \leq 1 \tag{4.3}$$

$$T = \frac{100(x_1+1)}{3} \text{ , for } 1 \leq x_1 \leq 2 \tag{4.4}$$

It was solved using 192 elements and 64 internal points regularly spaced for each region. Figure 4.4 plots the results obtained for boundary nodes at line $(x_1, 0, 0)$ and internal nodes at $(x_1, 0.25, 0.125)$. All results fit the analytical solution.

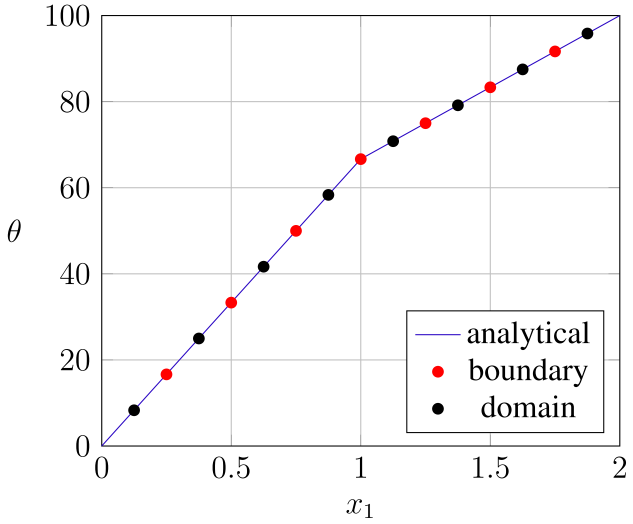

Figure 4.4 – Calculated temperature at boundary and domain nodes.

Considering all nodes of this problem, the maximum relative error for boundary nodal and internal points are given in Table 4.1, demonstrating that isotropic multi-region implementation is working correctly.

Table 4.1 – Maximum relative error for isotropic subregion solution.

Region	Boundary	Domain
1	0.293%	0.068%
2	0.106%	0.036%

4.2.3 Anisotropic material

An anisotropic thermal problem proposed and solved by Kögl and Gaul (2003) is shown in Figure 4.5. Face 1 has temperature $\theta = 0$ K, face 2 has $\theta = 100$ K and the other faces are insulated. The thermal conductivity tensor is given in Equation 4.5. This problem was solved in ANSYS using 1400 quadratic rectangular elements of size 5 mm to become the reference solution, as shown in Figure 4.6. ANSYS solution is also given at it.

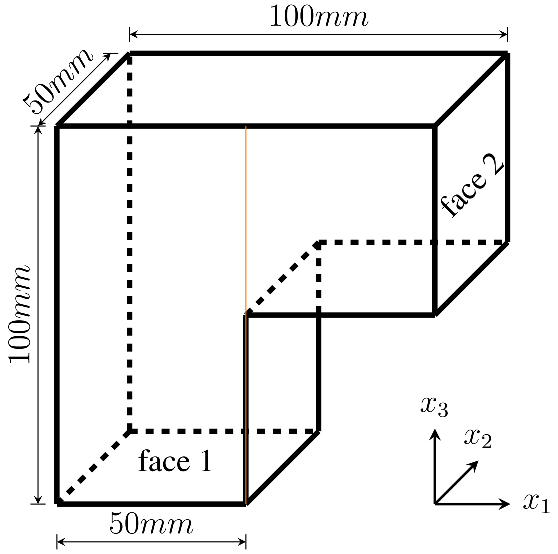

Figure 4.5 – Anisotropic potential problem.

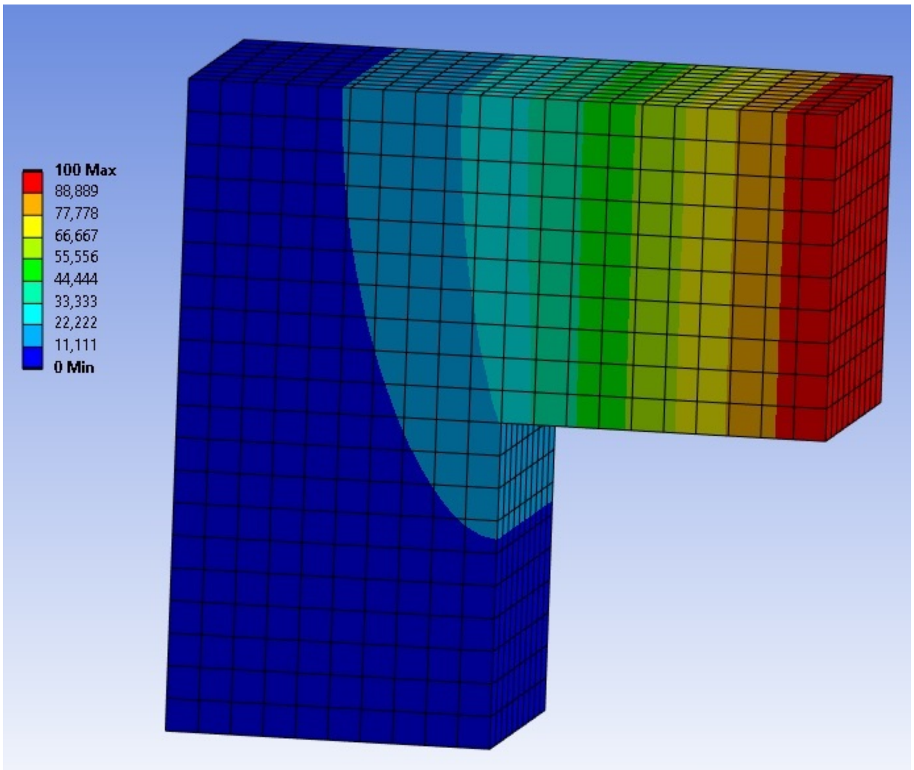

Figure 4.6 – ANSYS mesh and temperature solution.

$$\boldsymbol{\kappa} = \begin{bmatrix} 5.2 & 0 & 0 \\ 0 & 7.6 & 0 \\ 0 & 0 & 38.3 \end{bmatrix} \tag{4.5}$$

The boundary conditions and the material properties make the temperature field independent of the x_2 direction. Meshes with 28, 112, 448, 700, and 2800 boundary elements were used with 224 internal points set equally spaced 10 mm from each other and from the boundary, so the coordinates x_1 and x_3 match the boundary nodes. Relative differences to ANSYS results for boundary and domain nodes are plotted in Figure 4.7.

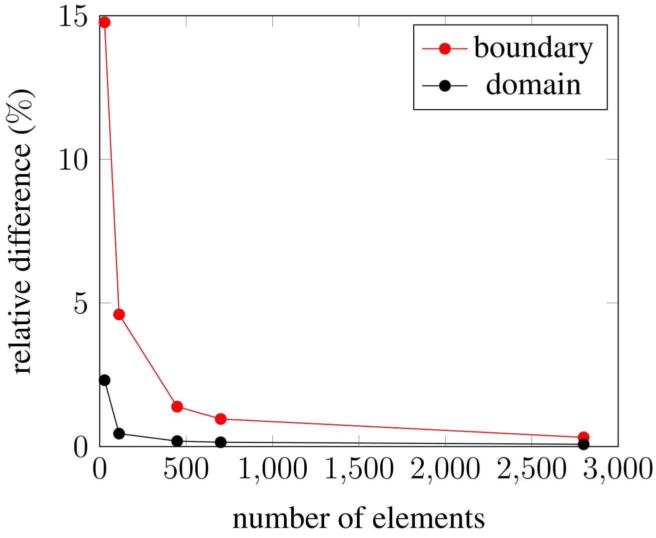

Figure 4.7 – Relative temperature difference from BESLE to ANSYS.

Figure 4.8 shows temperature results along line $(50, 0, x_3)$ for all meshes. The subtitle shows the number of elements used, while reference values from ANSYS are plotted in a continuous line. It is possible to see that only the values of the most coarse mesh are far off ANSYS' results. All other meshes converge to the reference.

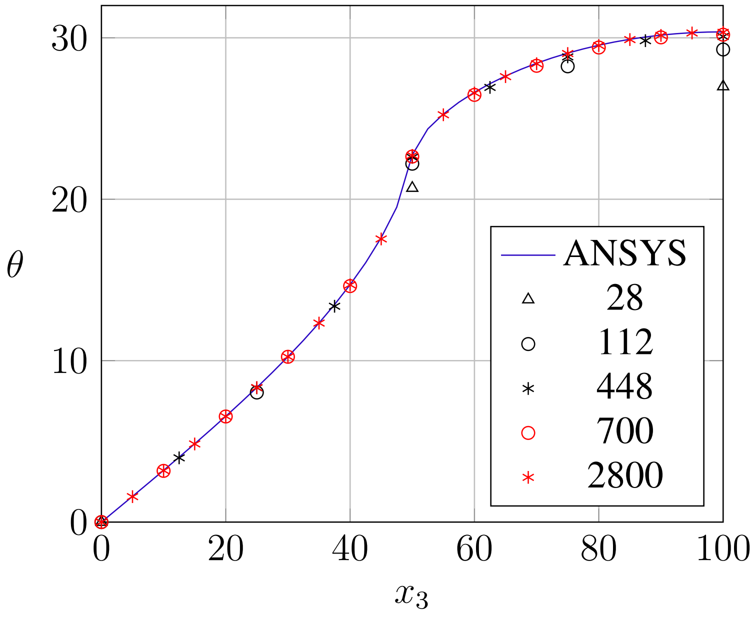

Figure 4.8 – Temperature along line $(50, 0, x_3)$ for different mesh sizes and ANSYS reference.

4.2.4 Seepage flow in anisotropic multiple region

The bidimensional dam presented in Figure 4.9 was solved by Brebbia and Chang (1979). It has two different regions, both with anisotropic permeability properties and subjected to a hydraulic pressure of 20 m of column water upstream and 5 m downstream.

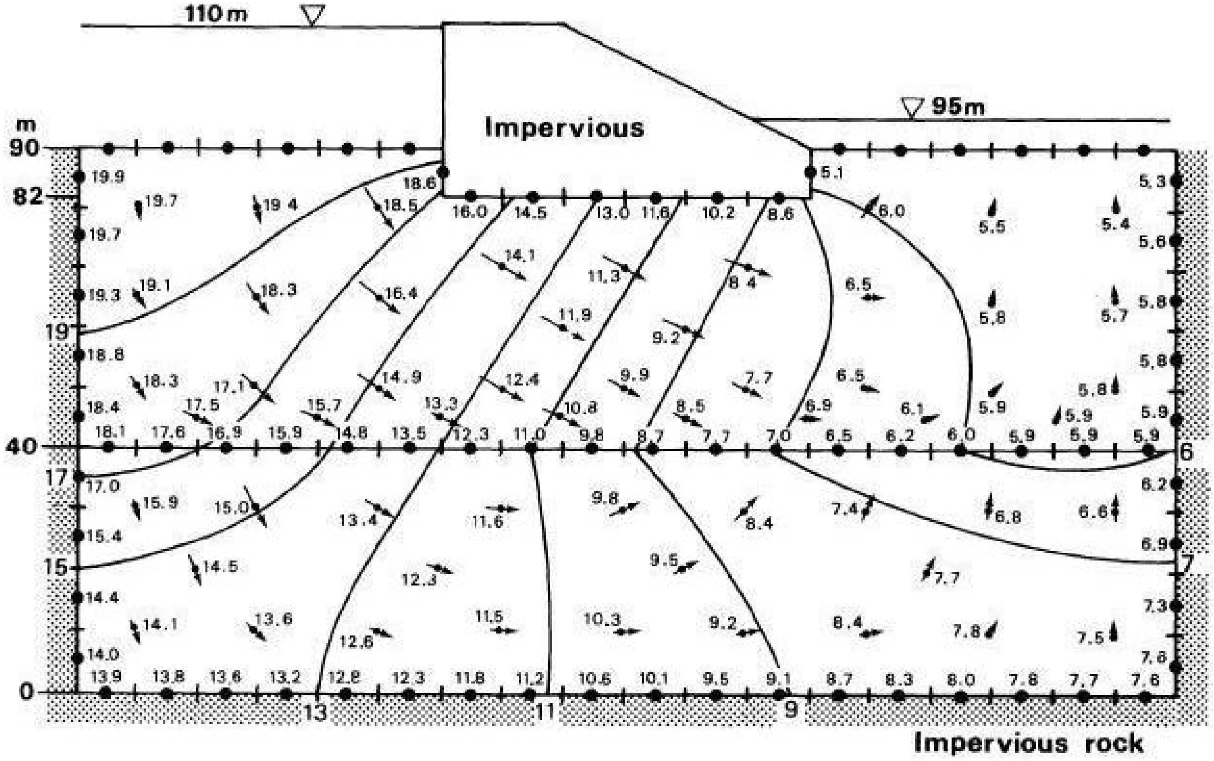

Figure 4.9 – Bidimensional anisotropic dam and potential at specific nodes. Extracted from: Brebbia and Chang (1979).

The above region has coefficients of permeability $k_{11} = 4 \times 10^{-5}$ m/s and $k_{22} = 1 \times 10^{-5}$ m/s rotated $45°$ counterclockwise. The bottom region has properties $k_{11} = 0.25 \times 10^{-5}$ m/s and $k_{22} = 0.075 \times 10^{-5}$ m/s aligned with principal axes. After rotating the properties of the above region and applying the Equation 3.28, the permeability tensor used for the superior region becomes:

$$\boldsymbol{\kappa}^{(SUP)} = \begin{bmatrix} 2.5 \times 10^{-5} & 1.5 \times 10^{-5} & 0 \\ 1.5 \times 10^{-5} & 2.5 \times 10^{-5} & 0 \\ 0 & 0 & 1.6 \times 10^{-5} \end{bmatrix} m/s \tag{4.6}$$

And for the inferior region:

$$\boldsymbol{\kappa}^{(INF)} = \begin{bmatrix} 2.5 \times 10^{-6} & 0 & 0 \\ 0 & 7.5 \times 10^{-7} & 0 \\ 0 & 0 & 7.5 \times 10^{-7} \end{bmatrix} m/s \tag{4.7}$$

Brebbia and Chang (1979) obtained the results presented in Figure 4.9 using constant Boundary Elements, so results are at the middle of the element. BESLE plots potential results at geometrical nodes, then, for better boundary values comparison, BESLE results were interpolated to match the nodal points position of the reference results, and calculated values are given in Figure 4.10. The continuous lines represent the reference results while the triangles are the values calculated by BESLE and colors differentiate the various boundaries and the interface. For internal points, the comparison is given in Figure 4.11, with the different colored lines representing the x_2 coordinate of the nodes. Once again, continuous lines are the reference solution while triangles mean the BESLE results. For boundary nodes and domain points, calculated and reference values are close to each other, demonstrating the coherency of Equation 3.26 and validating the DDM code implemented.

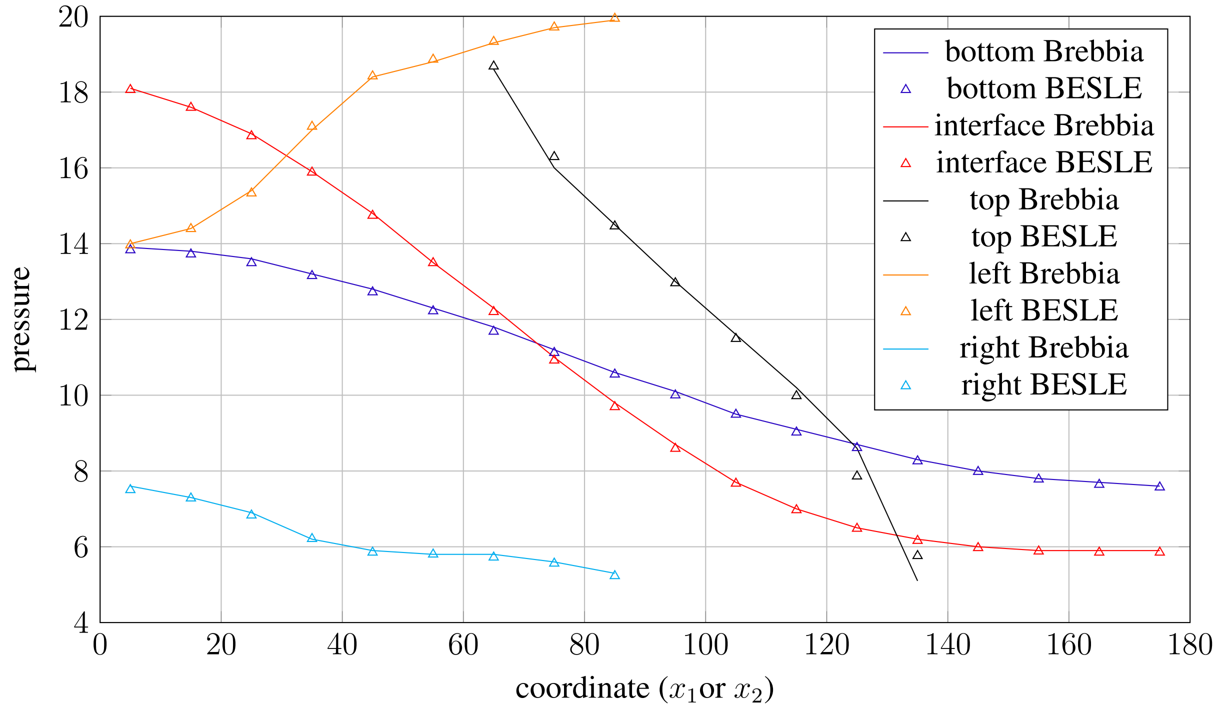

Figure 4.10 – BESLE pressure solution for nodes at the boundary and interface.

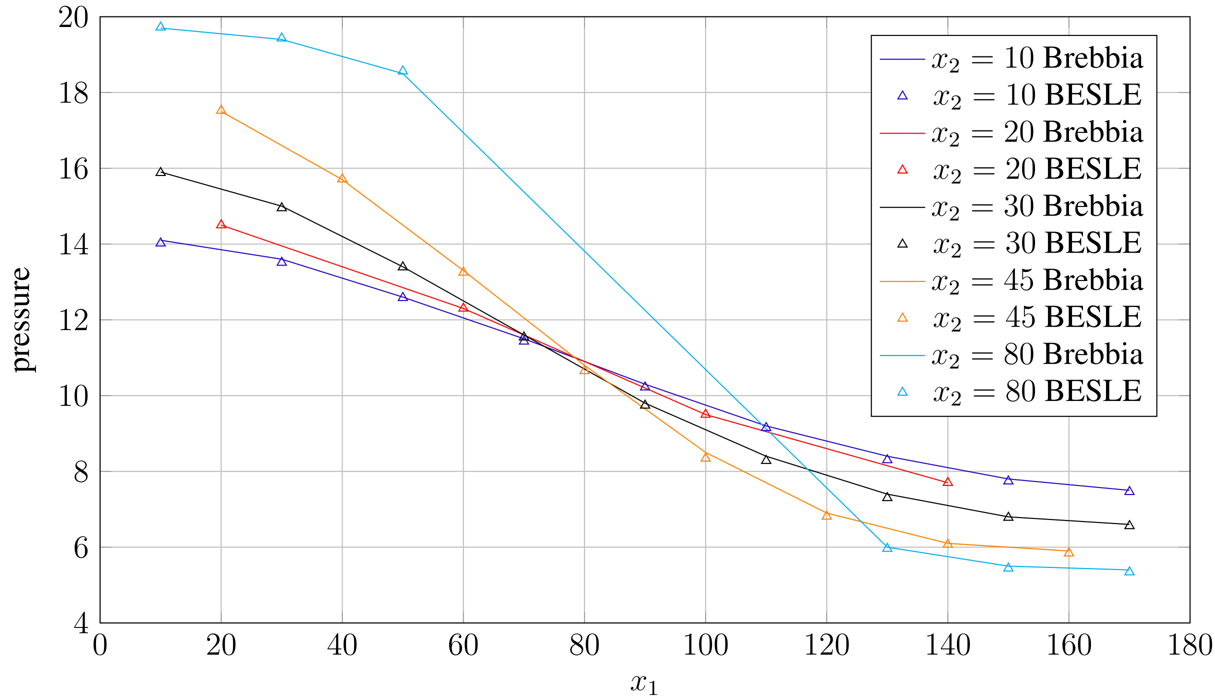

Figure 4.11 – BESLE pressure solution for selected domain points.

4.3 Thermoelastic problems

4.3.1 Isothermal deformation

The first thermoelastic problem is an isotropic cube of unit dimensions and a constant temperature of $\theta = 100$ at the entire body. This uniform temperature dismisses the use of the Dual Reciprocity Method since $\theta_{,j} = 0$, making null the volume integral. Figure 4.12 shows that face 1 is at the bottom and is normal to x_1 direction, face 2 is behind the cube and is normal to x_2 direction, and face 3 is at the left of the cube and is normal to x_3 direction. The displacement at these faces is restricted only in their normal direction, allowing them to slip over the plane each face lies within.

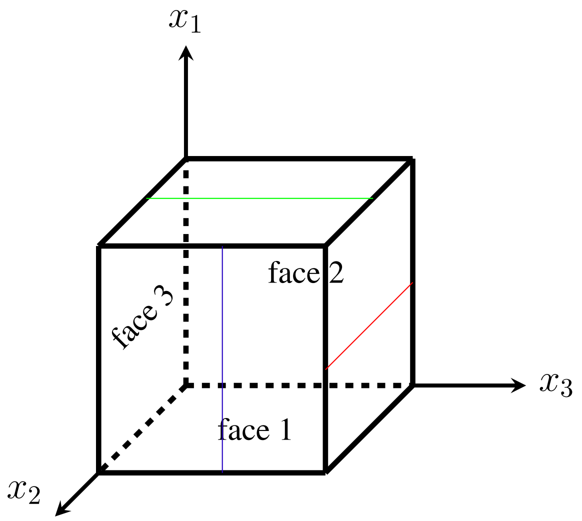

Figure 4.12 – Isothermal cube and boundary conditions. Colored lines are used for displacements values comparison.

These boundary conditions create a regular dilation problem, with the deformation becoming equal in all directions. The displacement at the *i*-th direction of any point of the body is given by:

$$u_i = \alpha\theta x_i \tag{4.8}$$

The expansion coefficient used for this problem is $\alpha = 2.0 \times 10^{-5}$. Then, the displacement is:

$$u_i = 0.002x_i \tag{4.9}$$

The mesh of this problem was defined using 11x11 divisions at each face, generating 1452 elements equally sized. The displacement u_1 for some nodes is given in Figure 4.13, and the great accuracy of the results can be seen. The same can be observed in Figures 4.14 and 4.15, with the results of the displacements u_2 and u_3, respectively, for selected nodes.

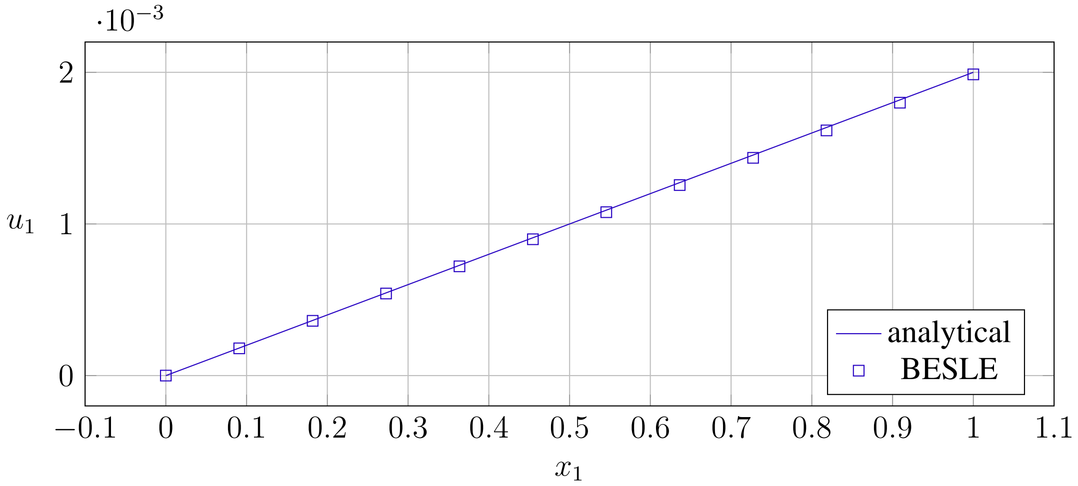

Figure 4.13 – Displacements u_1 for the nodes located along the line $(x_1, 1.0, 0.5455)$.

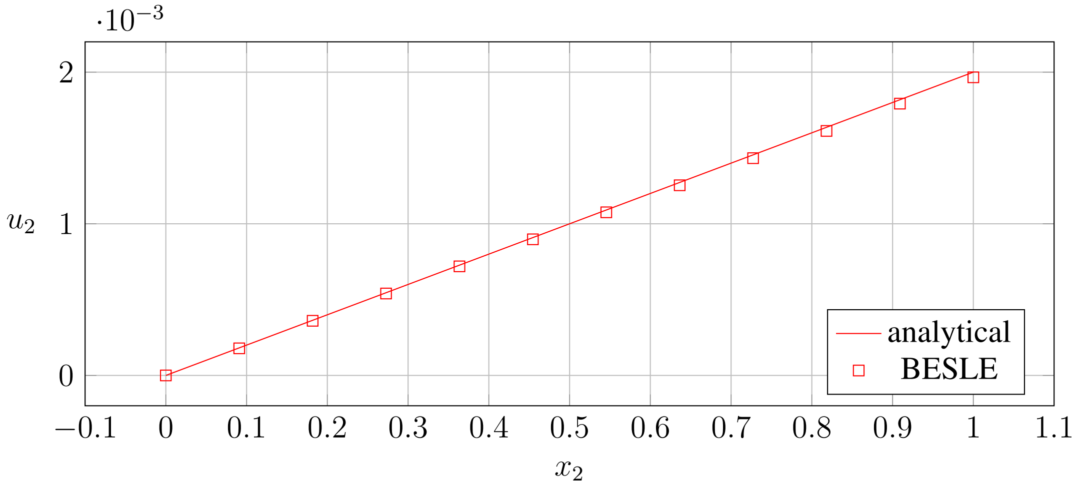

Figure 4.14 – Displacements u_2 for the nodes located along the line $(0.4546, x_2, 1.0)$.

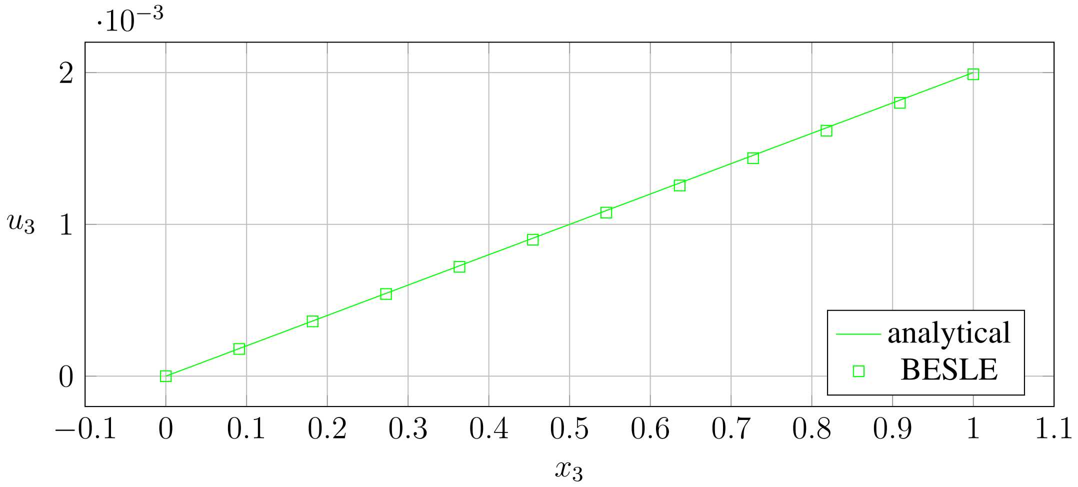

Figure 4.15 – Displacements u_3 for the nodes located along the line $(1.0, 0.4546, x_3)$.

4.3.2 Isothermal stresses

The cube of Section 4.3.1 is now under different boundary conditions: all the faces have displacement restricted at the normal direction. This means that the expansion will not deform the cube, but will only generate thermal stresses.

The thermal expansion coefficient is the same as the previous problem ($\alpha = 2.0 \times 10^{-5}$), as well as the temperature ($\theta = 100$) and the mesh refinement. The elasticity modulus used is $E = 210 \times 10^9$ and the coefficient of Poisson is $\nu = 0.35$.

Since there is no deformation, the stress can be calculated by the Equation 2.1, given by:

$$\sigma_{ij} = -\gamma_{ij}\theta = -C_{ijkl}\alpha_{kl}\theta \tag{4.10}$$

Applying the isotropic material properties values, one has:

$$\sigma_{ij} = -1.400 \times 10^6 \delta_{ij} \tag{4.11}$$

where δ_{ij} is the Kroenecker delta, which means that there are only principal stresses. The Figures 4.16 to 4.18 present the stress results obtained by BESLE from all nodes of the cube, organized by their identification index (ID). The results are close to the Equation 4.11. It is noted that the number of nodes is less than the number of elements because the results of Paraview are placed at the geometrical nodes.

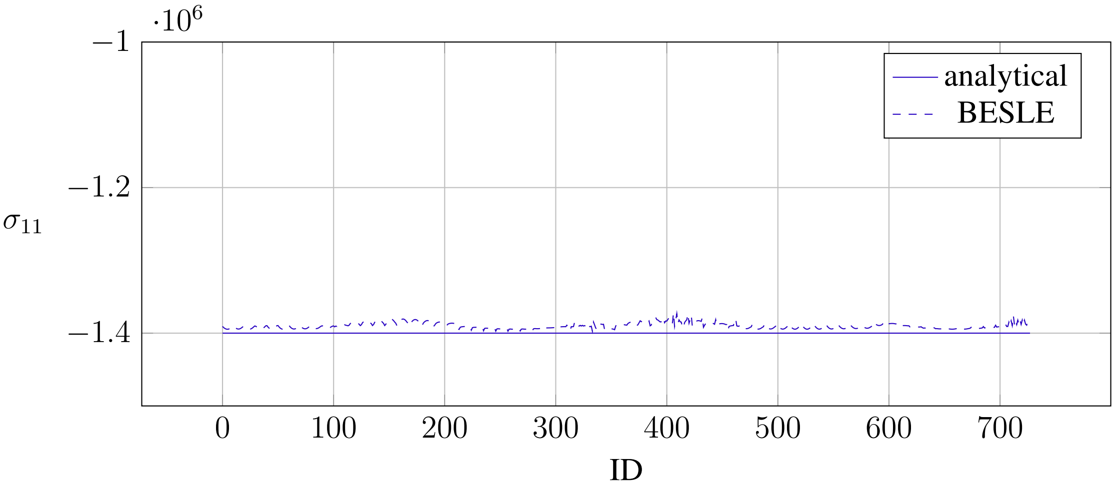

Figure 4.16 – Stress σ_{11} for all nodes of the fully restricted cube

.

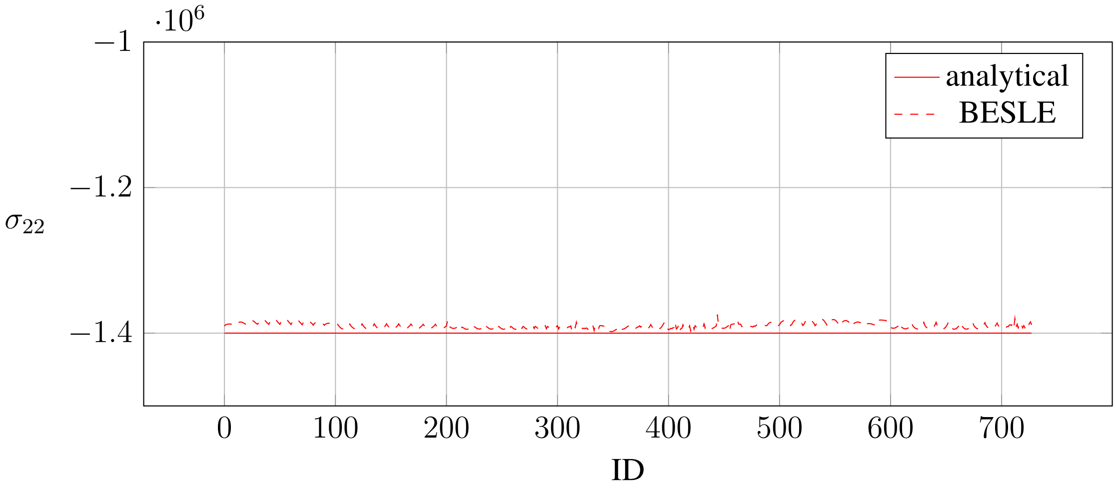

Figure 4.17 – Stress σ_{22} for all nodes of the fully restricted cube.

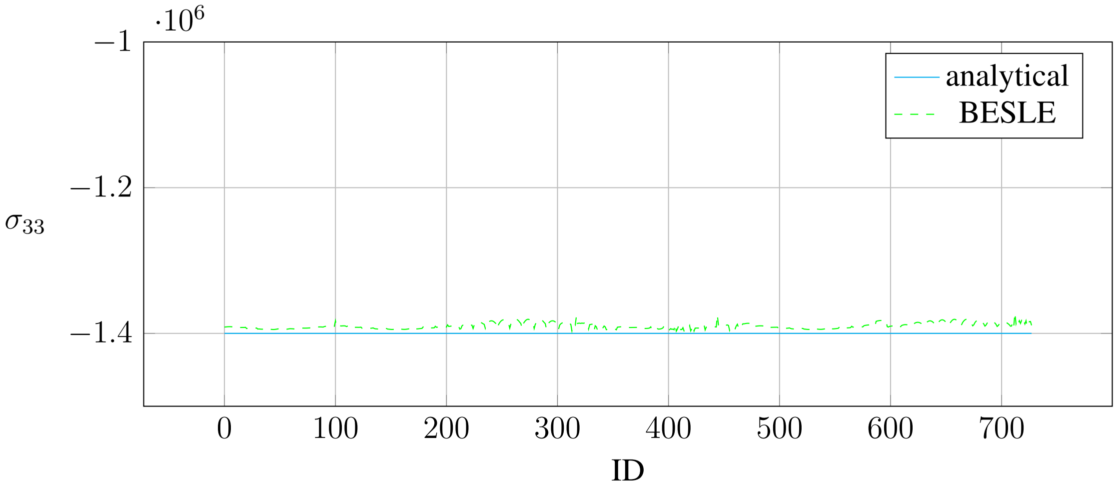

Figure 4.18 – Stress σ_{33} for all nodes of the fully restricted cube.

4.3.3 Isotropic thermal deformation

Figure 4.19 shows a 2D model of an isotropic beam under plane stress with material properties and boundary conditions. It is subjected only to quadratic thermal loading given by Equation 4.12. The beam has dimensions of 2 meters in the x_1 direction and 1 meter in the x_2 direction. For 3D simulation, a width of 1 meter was considered.

$$\theta(x_2) = 40x_2^2 - 60x_2 \tag{4.12}$$

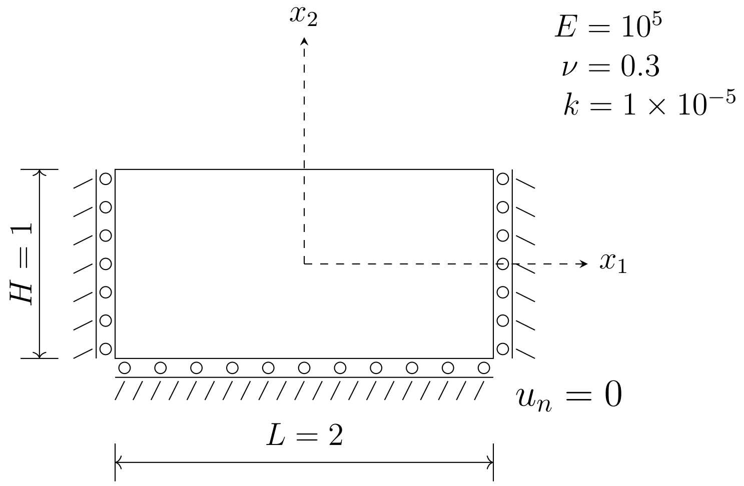

Figure 4.19 – BEM model of a beam subjected to thermal loading.

Analytical solutions for displacements u_2, deformations ϵ_{22} and stresses σ_{11} and σ_{33} are given in Equations 4.13 to 4.15 (Gao, 2003). The average relative error for displacements u_2 is calculated using meshes of 80, 180, 320, 500, 720, 980, 1280, 1620, and 2000 elements combined with 0, 1, 3, 20, 63, 144, 275, 468, 735, 1088, 1539, 2100, and 2783 internal points for temperature interpolation in Equation 2.145. Mesh size and distance between interpolation points are regular, i.e., boundary elements are all of the same size, and the distance among domain points is always the same.

$$u_2(x_2) = \left(\frac{1+\nu}{1-\nu}\right) k \left[\frac{40}{3}x_2^3 - 30x_2^2 + \frac{55}{6}\right] \tag{4.13}$$

$$\epsilon_{22}(x_2) = \left(\frac{1+\nu}{1-\nu}\right) k \left[40x_2^2 - 60x_2\right] \tag{4.14}$$

$$\sigma_{11}(x_2) = \sigma_{33}(x_2) = \left(\frac{-Ek}{1-\nu}\right) k \left[40x_2^2 - 60x_2\right] \tag{4.15}$$

Figure 4.20 shows the average relative error for displacements u_2. Each data series is identified by the number of elements and the abscissa indicates the number of internal points used at each simulation, with the first point meaning that no domain point was used.

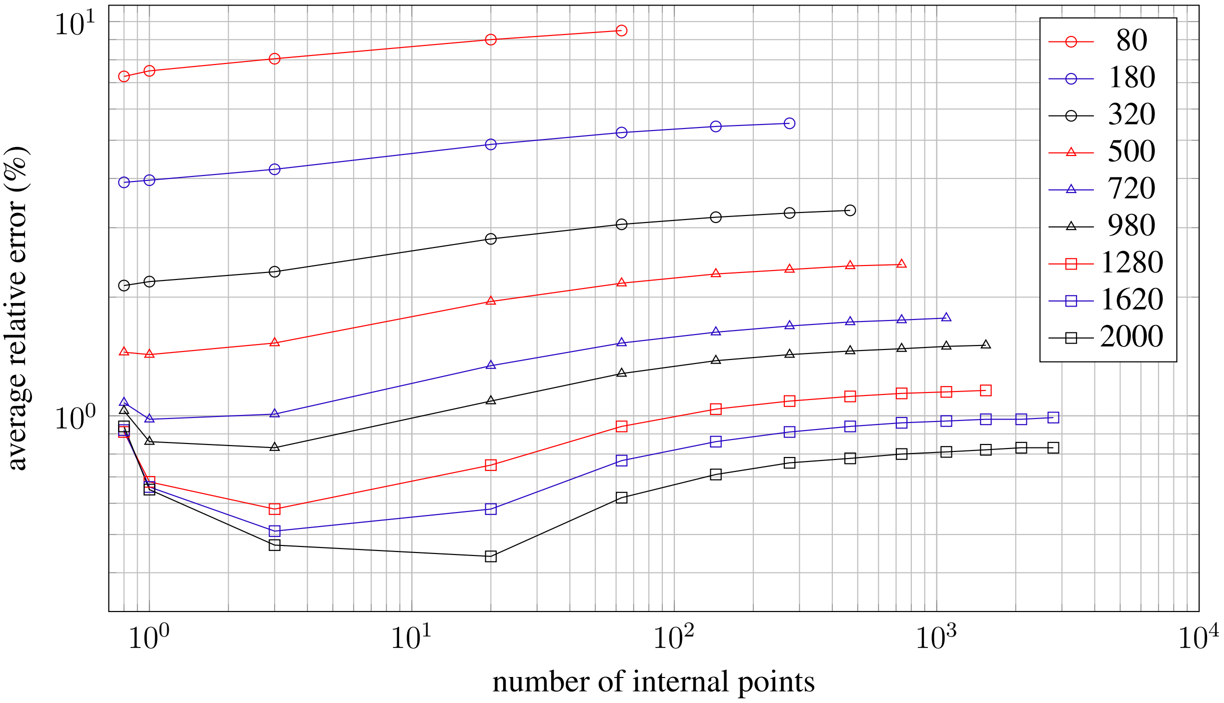

Figure 4.20 – Average relative error for displacement u_2 of isotropic beam calculated by BESLE.

Figure 4.20 shows that the accuracy of the results increased with the refinement of the mesh without using internal points, but the three most refined meshes had similar results: 0.91%, 0.92%, and 0.94%, respectively. The use of internal points only improved the results for the refined meshes, but continuously adding internal points reaches an optimal accuracy and then it decreases. This phenomenon is called saturation, also known as stagnation error, when the results fail to converge with increasing the number of points used for interpolation (Pooladi; Larsson, 2023). Moreover, all meshes show asymptotic increasing error as the number of internal points increases.

Stresses and strains only depend on the results of displacements and tractions. For this reason, results of stresses and strains at Figures 4.21 and 4.22 were obtained with the mesh of 2000 elements using 20 internal points, the simulation with the best accuracy. The procedure of Section 2.8 produced results with small relative errors although they are a little above the average at the edges. It is worth remembering that Equation 4.15 shows that analytical solutions for σ_{11} and σ_{33} are the same.

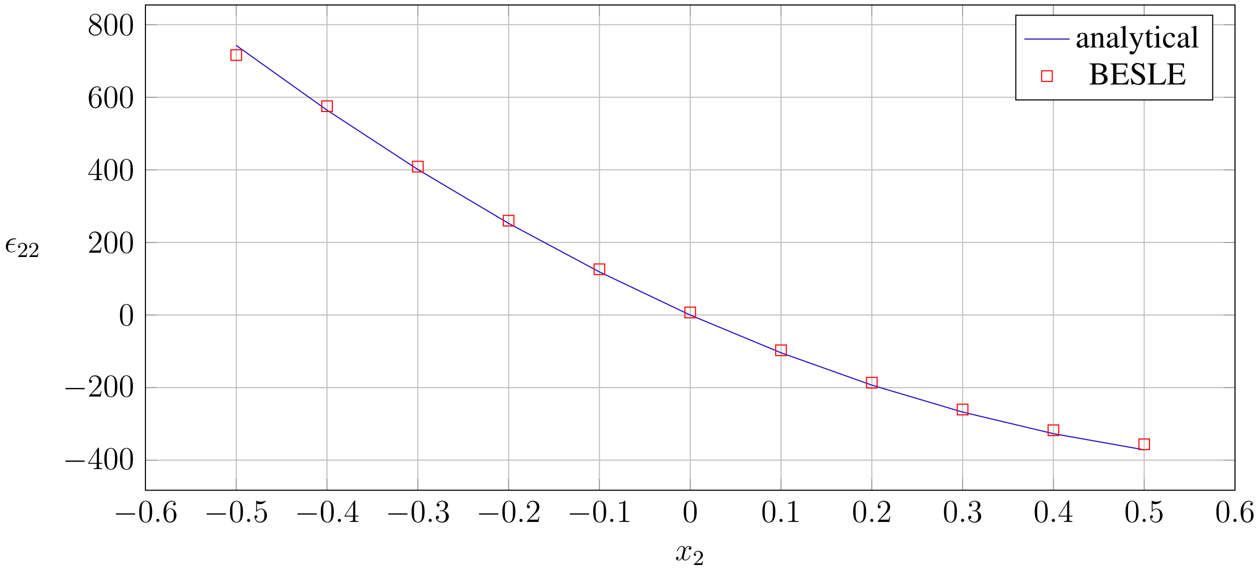

Figure 4.21 – Boundary strains ϵ_{22} ($\times 10^{-6}$) calculated at $(0.5, x_2, 0.5)$.

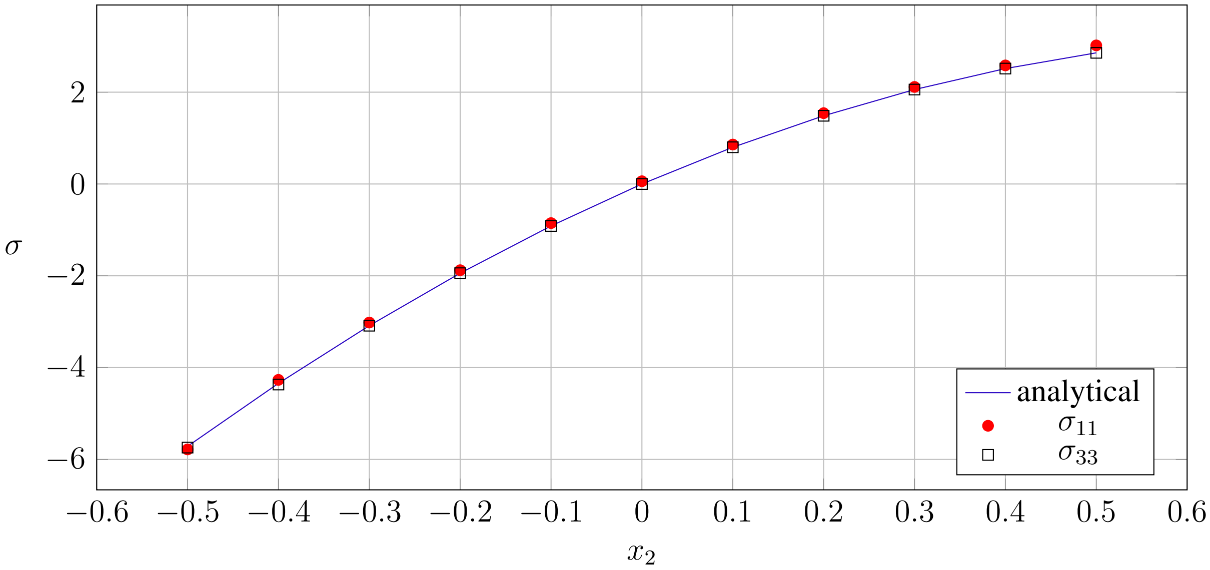

Figure 4.22 – Boundary stresses σ_{11} and σ_{33} calculated at $(0.5, x_2, 0.5)$.

4.3.4 Orthotropic thermal deformation

This example is similar to the one of Section 4.2.1, with the same geometry (cube edge is 1 m) and thermal conditions are the same. As shown in Figure 4.23, the face with null temperature is constrained in all directions while all the other faces are free. Orthotropic conductivity, elasticity, and expansion tensors are given in Equations 4.16, 4.17, and 4.18, respectively.

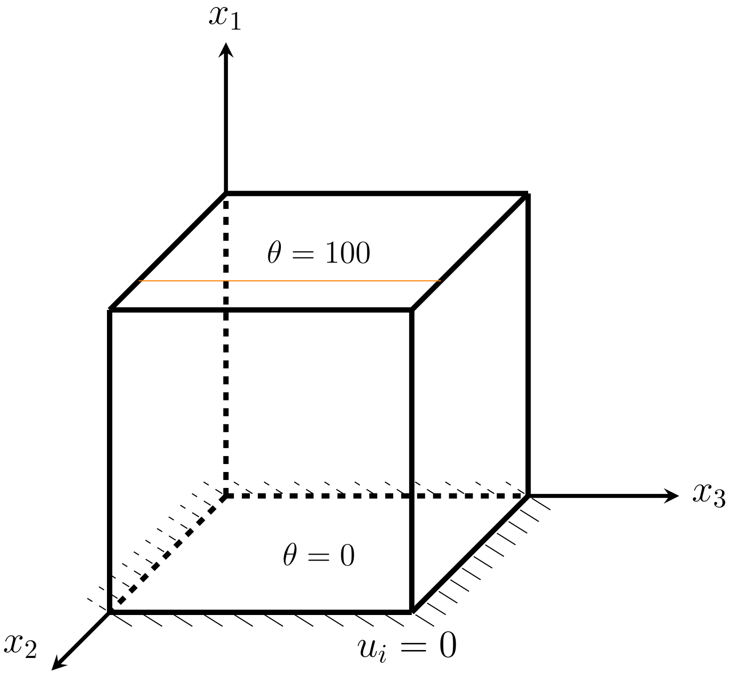

Figure 4.23 – Orthotropic cube and boundary conditions. The orange line is used for stress results.

$$\boldsymbol{\kappa} = \begin{bmatrix} 1.0 & 0 & 0 \\ 0 & 2.0 & 0 \\ 0 & 0 & 3.0 \end{bmatrix} W/mK \tag{4.16}$$

$$\mathbf{C} = \begin{bmatrix} 1334.5 & 738.8 & 619 & 0 & 0 & 0 \\ 738.8 & 1701.2 & 646.9 & 0 & 0 & 0 \\ 619 & 646.9 & 1147.4 & 0 & 0 & 0 \\ 0 & 0 & 0 & 800 & 0 & 0 \\ 0 & 0 & 0 & 0 & 1200 & 0 \\ 0 & 0 & 0 & 0 & 0 & 1000 \end{bmatrix} Pa \tag{4.17}$$

$$\boldsymbol{\alpha} = \begin{bmatrix} 2.0 & 0 & 0 \\ 0 & 2.5 & 0 \\ 0 & 0 & 3.0 \end{bmatrix} \times 10^{-5} K^{-1} \tag{4.18}$$

This problem was solved at ANSYS using 864 quadratic rectangular elements of size 0.8333 as a basis for comparison. Figure 4.24 presents ANSYS' mesh and u_1 displacement results. As for the problem in Section 4.3.3, many numerical experiments were done combining different numbers of elements and internal points, and the relative difference of BESLE and ANSYS results for displacements at all free nodes for the three directions was used to verify the accuracy of the solutions. Only the relative difference for displacements u_1 is presented because the results for u_2 and u_3 have no significative difference. BESLE results were obtained using regular meshes of 48, 108, 192, 432, 768, 972, and 1758 elements combined with the use of 0, 1, 8, 27, 64, 125, 216, 343, 512, 729, 1000, 1331, 1728, and 2197 internal points for temperature interpolation.

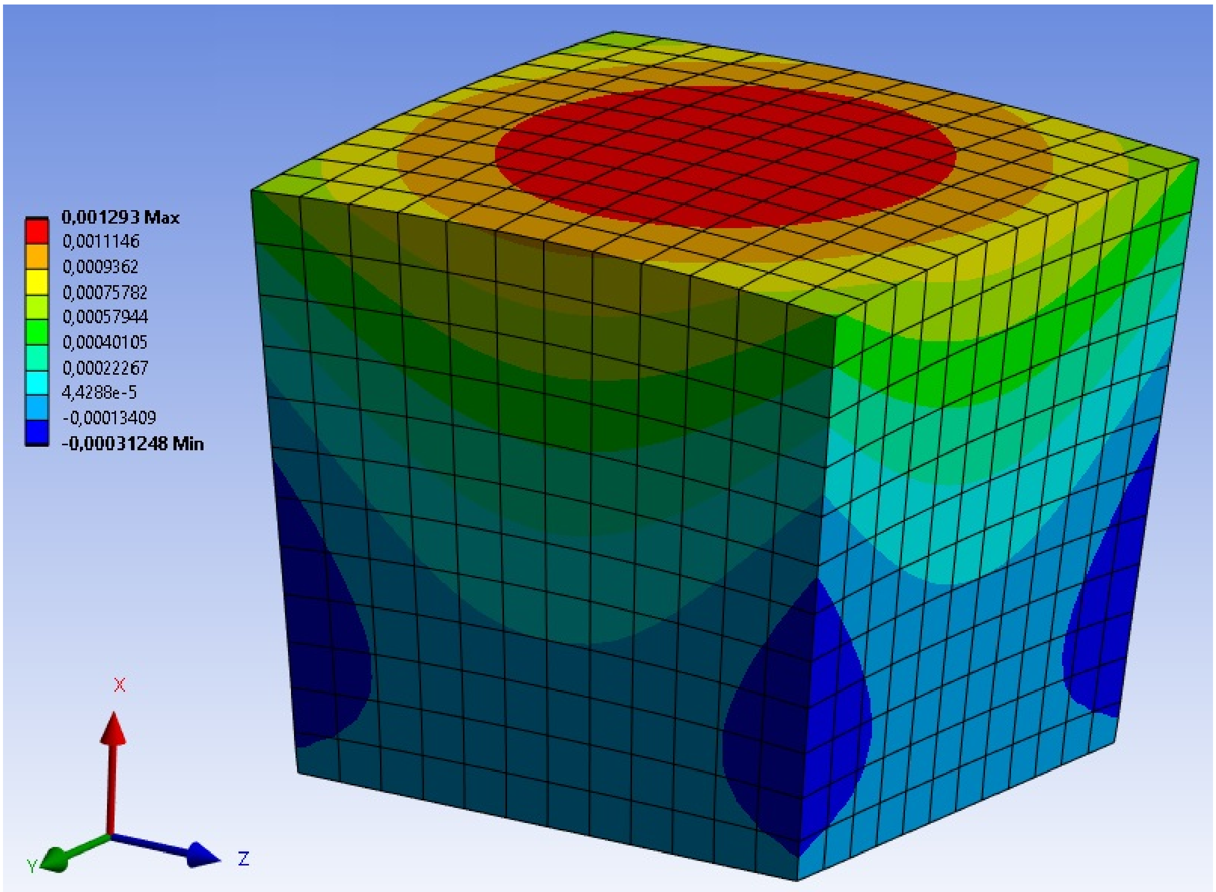

Figure 4.24 – ANSYS mesh and u_1 displacement results for the orthotropic cube. Coordinates X, Y and Z means u_1, u_2, and u_3 respectively.

Figure 4.25 presents the average relative difference from ANSYS for displacements u_1 calculated by BESLE. As for the isotropic example, mesh refinement produced continuous improvement in the results, but here, the use of internal points made the BESLE results converge to the ANSYS values. An asymptotic behavior can be seen with increasing the amount of internal points, demonstrating stability in the results.

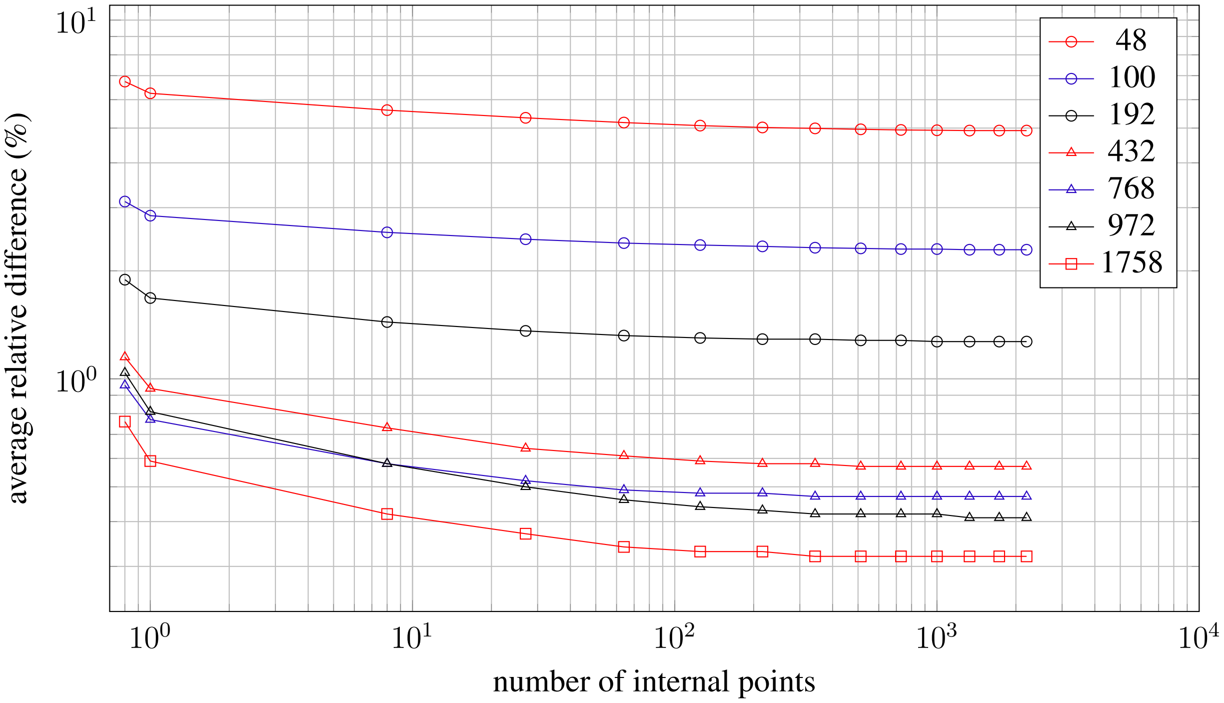

Figure 4.25 – Average relative difference from ANSYS for displacements u_1 calculated by BESLE.

Figures 4.26 to 4.28 present results of normal stresses obtained at line $(x_1, 1.0, 0.75)$, which is the orange line of Figure 4.23. BESLE results have good agreement with ANSYS presenting some differences at the edges. It can be seen that stresses σ_{yy} calculated by ANSYS oscillate around zero for $0.833 < x_1 < 0.333$ while BESLE results fit exactly zero, and stresses σ_{zz} calculated by BESLE are smoother than ANSYS solutions for $0.0 < x_1 < 0.250$. Considering the regular surface and thermal conditions, it seems that BESLE solutions are more representative than ANSYS in these regions.

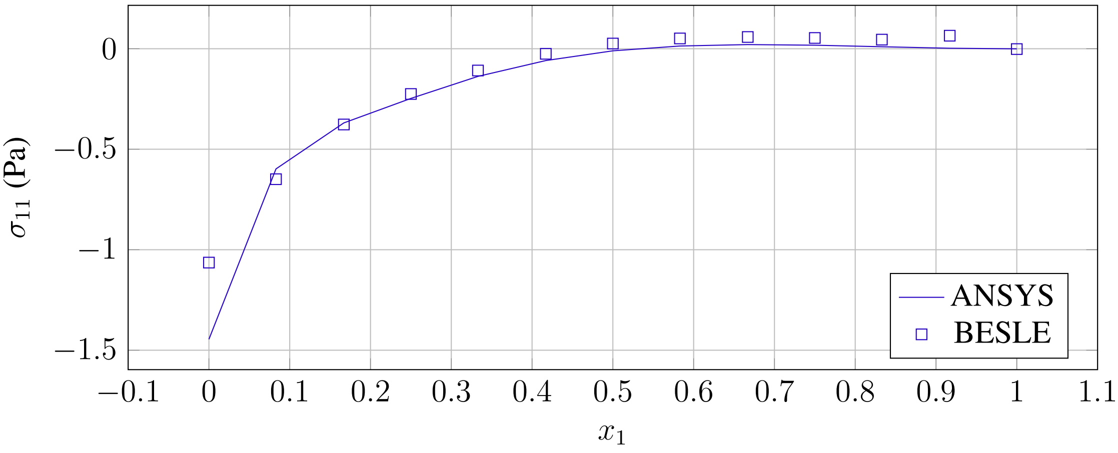

Figure 4.26 – Stresses σ_{11} at line $(x_1, 1.0, 0.75)$.

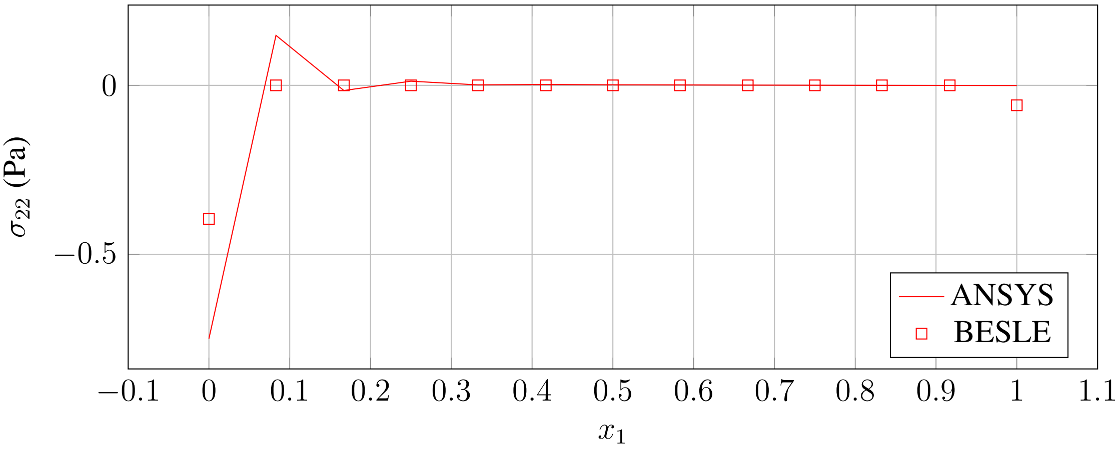

Figure 4.27 – Stresses σ_{22} at line $(x_1, 1.0, 0.75)$.

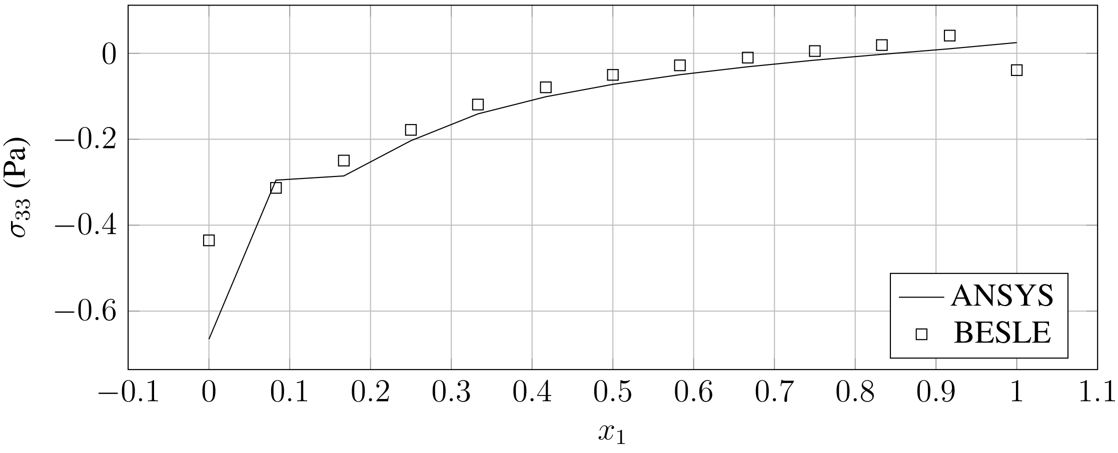

Figure 4.28 – Stresses σ_{33} at line $(x_1, 1.0, 0.75)$.

4.3.5 Anisotropic thermal deformation

This problem is the continuation of Section 4.2.3, with the geometry being repeated in Figure 4.29 for convenience. Faces 1 and 2 are constrained in all directions and the others are free. Elasticity tensor and mechanical temperature coefficient are given by Equations 4.19 and 4.20 respectively.

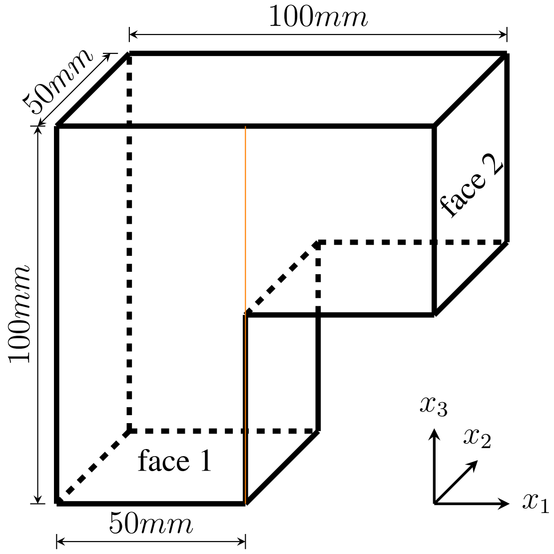

Figure 4.29 – Anisotropic thermoelasticity example. The orange line is used for displacement results.

$$\mathbf{C} = \begin{bmatrix} 430.1 & 130.4 & 18.2 & 0 & 0 & 201.3 \\ 130.4 & 116.7 & 21.0 & 0 & 0 & 70.1 \\ 18.2 & 21.0 & 73.6 & 0 & 0 & 2.4 \\ 0 & 0 & 0 & 19.8 & -8.0 & 0 \\ 0 & 0 & 0 & -8.0 & 29.1 & 0 \\ 201.3 & 70.1 & 2.4 & 0 & 0 & 147.3 \end{bmatrix} GPa \tag{4.19}$$

$$\gamma = \begin{bmatrix} 1.01 & 2.00 & 0 \\ 2.00 & 1.48 & 0 \\ 0 & 0 & 7.52 \end{bmatrix} \times 10^6 N/Km^2 \tag{4.20}$$

Kögl and Gaul (2003) compared linear 4-node and quadratic 8-node BEM results with 99 internal nodes against linear 8-node and quadratic 20-node FEM results generated with ANSYS, presenting only displacements u_3 along nodal points placed at coordinates $(50, 0, x_3)$. For both methods, 350 elements of size 10 mm were used with 99 internal points for the BEM, shown in Figure 4.30. All the results they obtained are quite similar and quadratic FEM was chosen as reference to compare the results obtained by BESLE. Once again, several simulations were done with BESLE, using meshes of 28, 112, 448, 700, and 2800 elements of regular size, combined with 0, 3, 32, 99, 224, 438, 720, 1127, 1664, 2474, 3200, 4235, 5472, and 6929 internal points. Figure 4.31 shows the relative difference for displacements u_3 calculated by BESLE at the points over the orange line $(50, 0, x_3)$ of Figure 4.29.

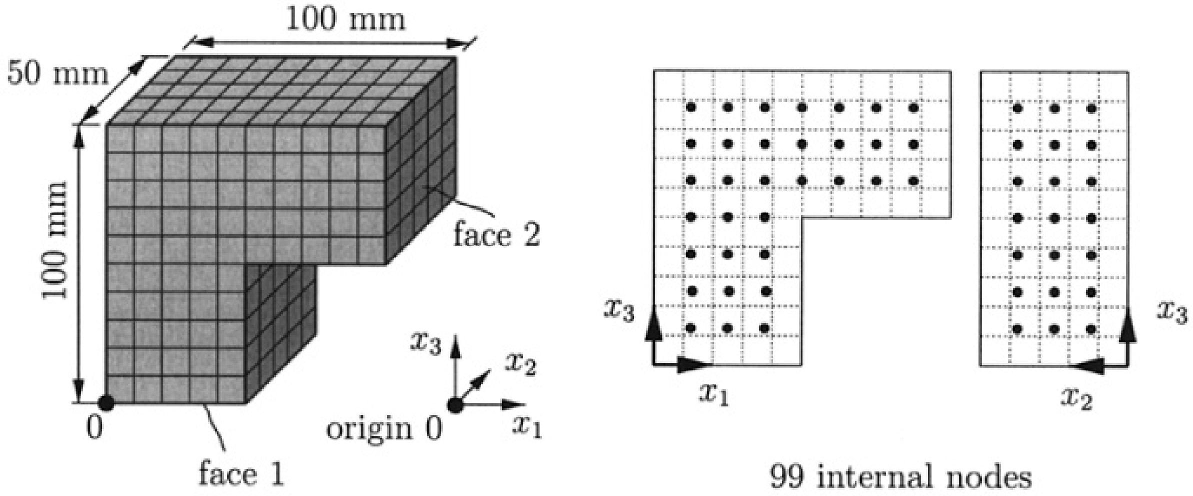

Figure 4.30 – Mesh and internal points used by Kögl and Gaul (2003). Extracted from: Kögl and Gaul (2003).

This time, a very different behavior is noted. The simulation using 28 elements and no internal points reached an average relative difference of 54%, completely nonrepresentative of the solution. Moreover, the refining of the mesh made this difference increase, reaching the value of 135% for the most refined mesh. As internal points were added, the results became better for each mesh until it reached a minimum. The amount of internal points used to achieve the stagnation error increases together with the number of elements of the mesh. Also, the accuracy results obtained just before saturation are better as the mesh refinement increases. The stagnation was not observed for the meshes of 700 and 2800 elements with the first one presenting slightly better results with a huge amount of internal points.

In a few words, mesh refinement together with a great number of internal points was necessary to achieve results representative of the real solution.

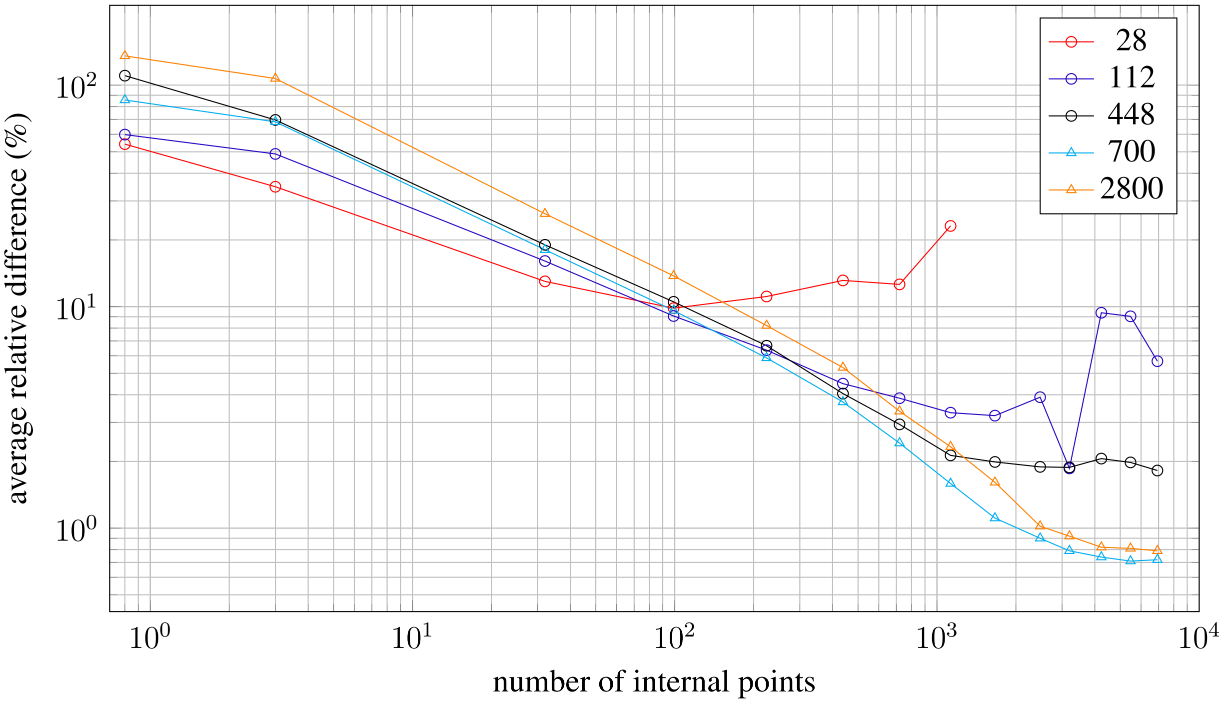

Figure 4.31 – Average relative difference from ANSYS for displacements u_3 calculated by BESLE at the orange line $(50, 0, x_3)$.

The necessity of internal points to obtain good results in this example is in opposition to the examples in Sections 4.3.3 and 4.3.4. A possible cause for that may be the thermal field. Figure 4.32 shows equipotential lines for these three problems, with the smaller temperatures of each one being represented by the blue color, while the higher temperatures are represented by the red color. All of them are divided by isotermals that represent one-tenth of the temperature range of each problem. It can be seen that the lines are regularly spaced for the first two problems, while the third one presents an irregular distribution of the temperature: the blue zone and the region delimited by the first isothermal are much bigger than the other regions delimited by the other isothermals. In other words, a great portion of the domain has a low gradient of the potential field, and another small portion has a high gradient. It seems that this thermal field and its derivatives were not well represented by using only boundary nodes.

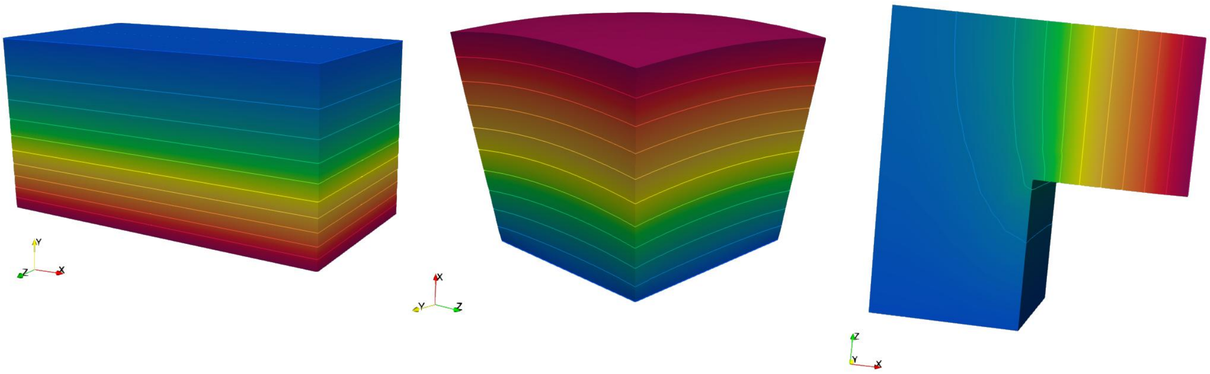

Figure 4.32 – Temperature field and isothermals for the problems: left, isotropic beam; center, orthotropic cube; right, anisotropic "L" shape.

4.4 Radial Basis Functions experiments

The examples solved in the previous section employed the interpolation function for the temperature used by Gaul *et al.* (2003), given in Equation 2.84, but the authors did not comment on the reasons for their choice. Also, the displacement results obtained for the anisotropic problem encouraged to search for conditions that could lead to better results.

Considering the notes in Section 2.4, some piecewise smooth RBF were chosen to verify the effect of the interpolation function in accuracy results for displacements and they are listed in Table 4.2, along with their first derivative. All of them were added by one for completeness (Karur; Ramachandran, 1994).

No infinitely smooth RBF was choosen to be experimented in this work because of the strong influence that the ϵ parameter have. As it was explained at Section 2.4, to obtain good interpolation it is necessary to use an optimal ϵ value or near it, meaning that an optimization problem needs to be solved first, and then, continue to solve the thermoelasticity problem. The search of this minimun is out of the scope of this thesis, so tests with these functions will not be done here.

The numerical tests in this section only compare the results for displacements, since stresses and strains are post-processing and dependent on the quality of displacement results.

The results obtained by function F1 are in Section 4.3 and are the basis of comparison. The graphical results obtained for the displacements of the orthotropic cube using functions F2 and F4 are presented in Figure 4.33, showing a deformed geometry completely incompatible with the real solution. Moreover, the displacements obtained using functions F2

Table 4.2 – Selected RBFs for experimental tests.

Function identification	RBF (ψ^q)	First derivative ($\psi^q_{,j}$)
F1	$1 + r^2 + r^3$	$(2 + 3r)r_j$
F2	$1 + r^2$	$2r_j$
F3	$1 + r^3$	$3rr_j$
F4	$1 + r^4$	$4r^2 r_j$
F5	$1 + r^5$	$5r^3 r_j$
F6	$1 + r^2 \ln(r + 1)$	$\left[2\ln(r + 1) + \frac{r}{r+1}\right] r_j$
F7	$1 + r^3 \ln(r + 1)$	$\left[3r\ln(r + 1) + \frac{r^2}{r+1}\right] r_j$

and F4 have order of 10^6 and 10^{28} respectively. Clearly, these functions are inappropriate to thermoelasticity, which is in accordance with the literature concerning DRM applications that only prescribe odd coefficients for this type of functions (Bayona, 2019), and for this reason, the use of high order even coefficients was abandoned.

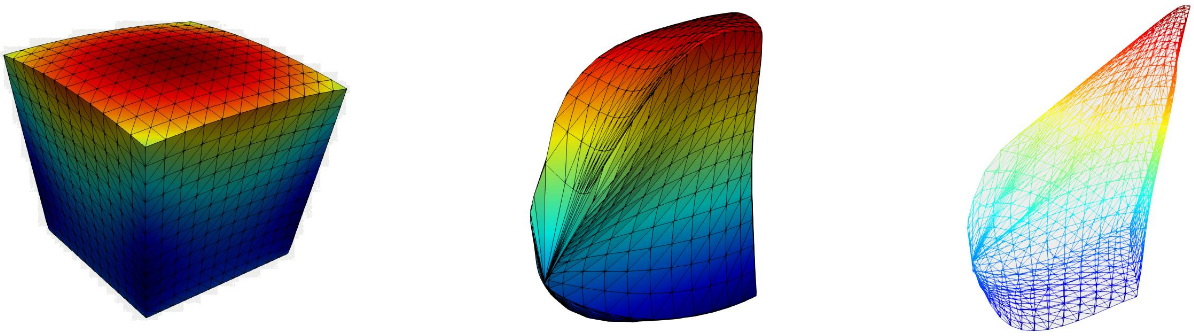

Figure 4.33 – Deformed geometry obtained for orthotropic cube using RBF F1 (left), F2 (center) and F4 (right).

4.4.1 Function F3

The function F3 is obtained from function F1 by extracting the r^2 term in an attempt to improve the accuracy. The results obtained for isotropic, orthotropic, and anisotropic problems are given in Figures 4.34, 4.35 and 4.36, respectively. When these results are compared with the ones obtained using the function F1, the results vary by only 0.01% for the isotropic and the anisotropic examples, meaning no significative difference. For the orthotropic problem, function F3 presented better performance with no internal points and, as they are added, the results become of the same accuracy.

The inclusion of the term r^2 in F1 to produce a more complete RBF neither benefits nor harms the accuracy, but includes a little more calculations, so, function F3 can be used instead of function F1.

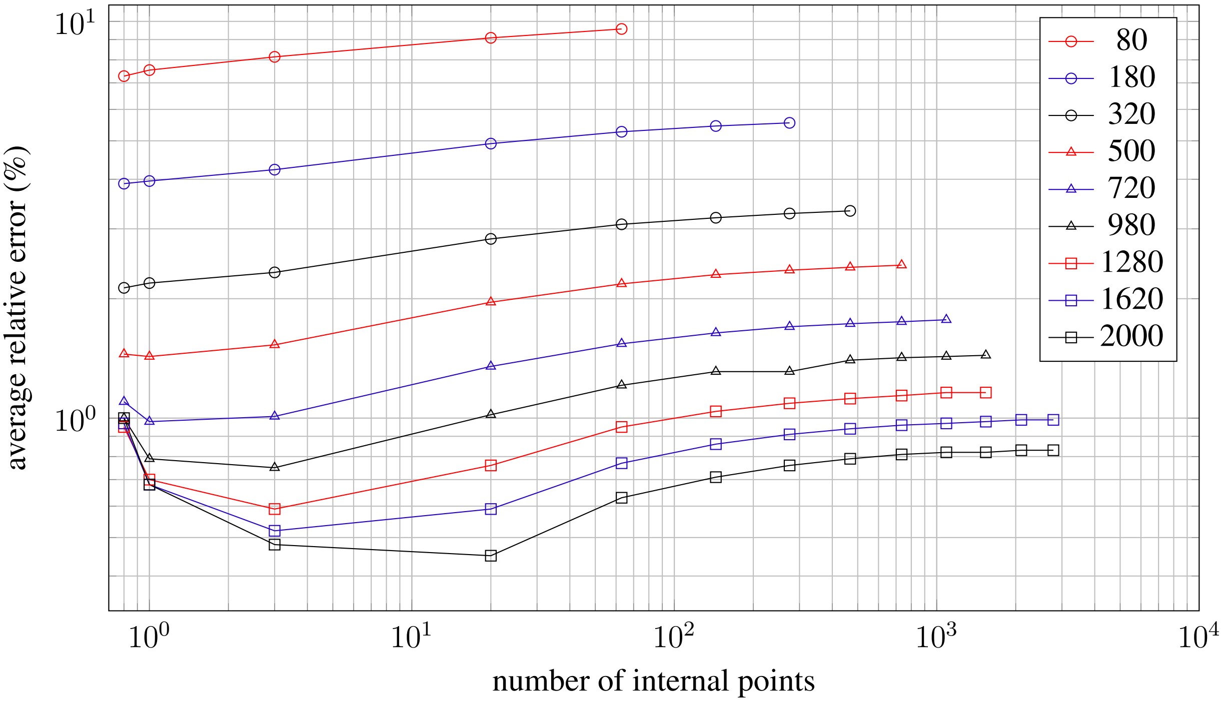

Figure 4.34 – Average relative error for displacement u_2 of the isotropic beam calculated by BESLE using function F3.

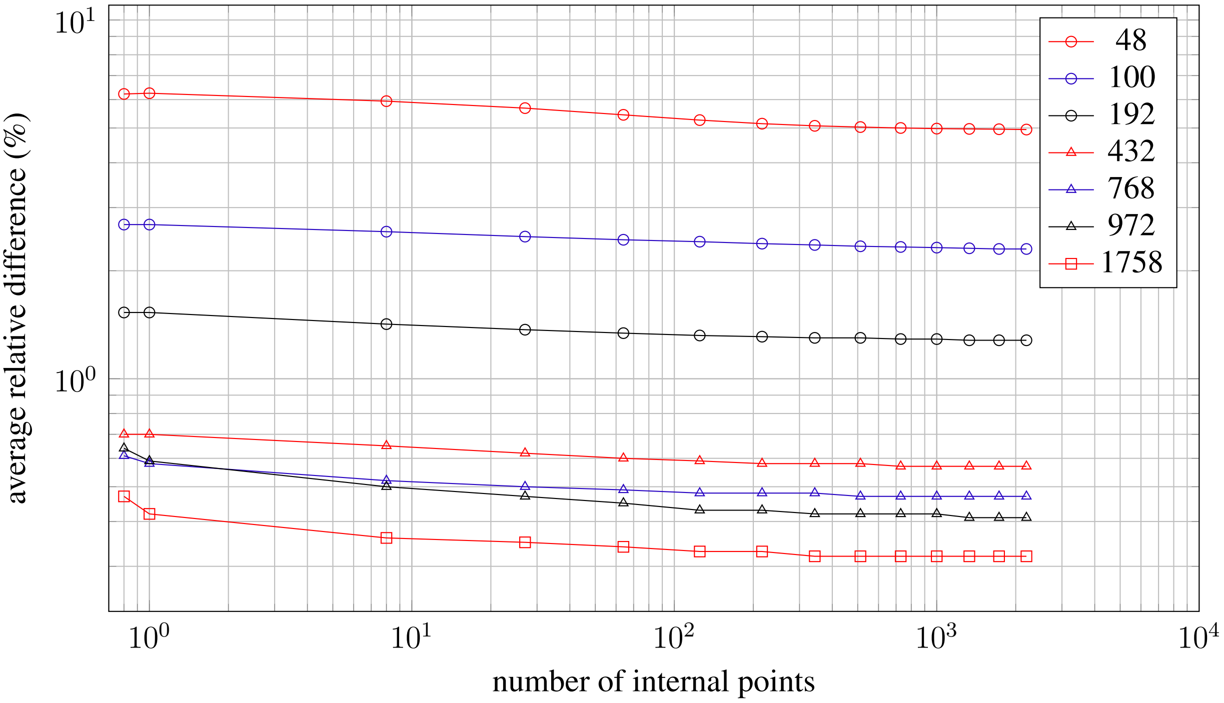

Figure 4.35 – Average relative difference from ANSYS for displacements u_1 of the orthotropic cube calculated by BESLE using function F3.

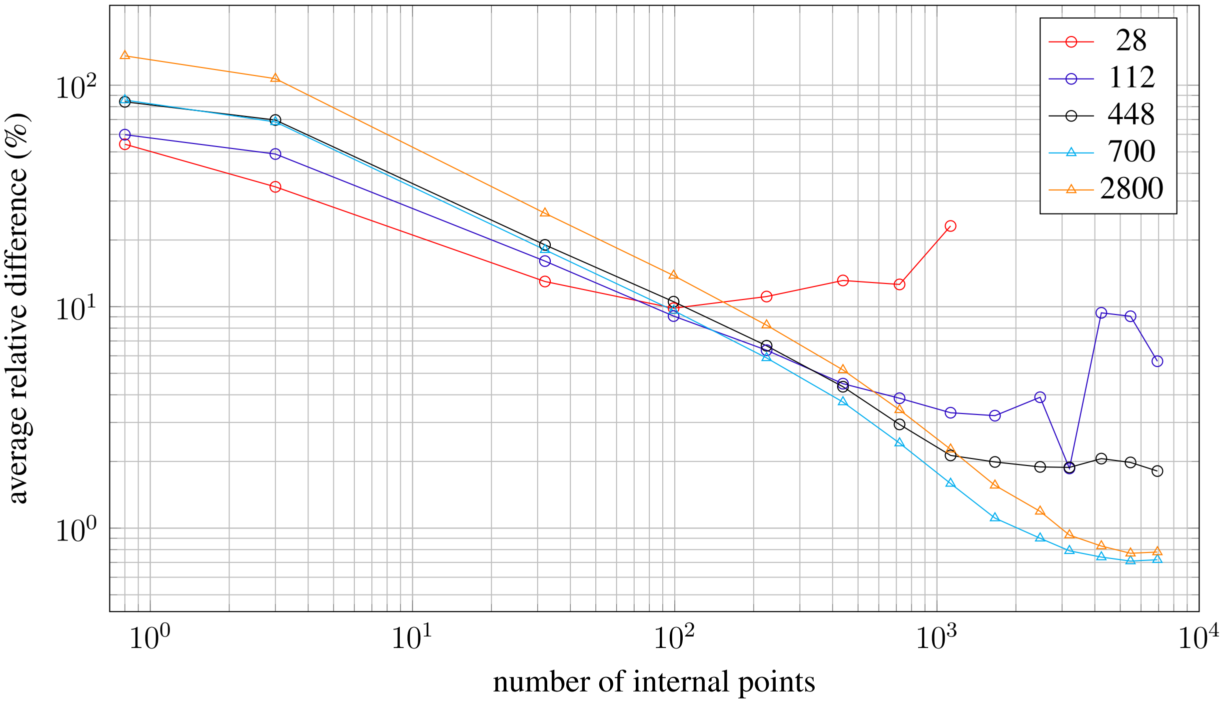

Figure 4.36 – Average relative difference from ANSYS for displacements u_3 at the orange line $(50, 0, x_3)$ of the anisotropic example calculated by BESLE using function F3.

4.4.2 Function F5

This function is an attempt to use high-order functions for temperature interpolation. Figure 4.37 shows the average relative error for displacement results calculated by BESLE for the isotropic problem. The meshes from 80 to 980 elements had the same behavior as the function F1. The mesh of 1280 elements had oscillatory accuracy that increased with the number of internal points. The two most refined meshes presented bad accuracy and the use of internal points did not guarantee good results. They are a consequence of the saturation that appeared with the mesh refinement and the great number of internal points used for the mesh with 1280 elements.

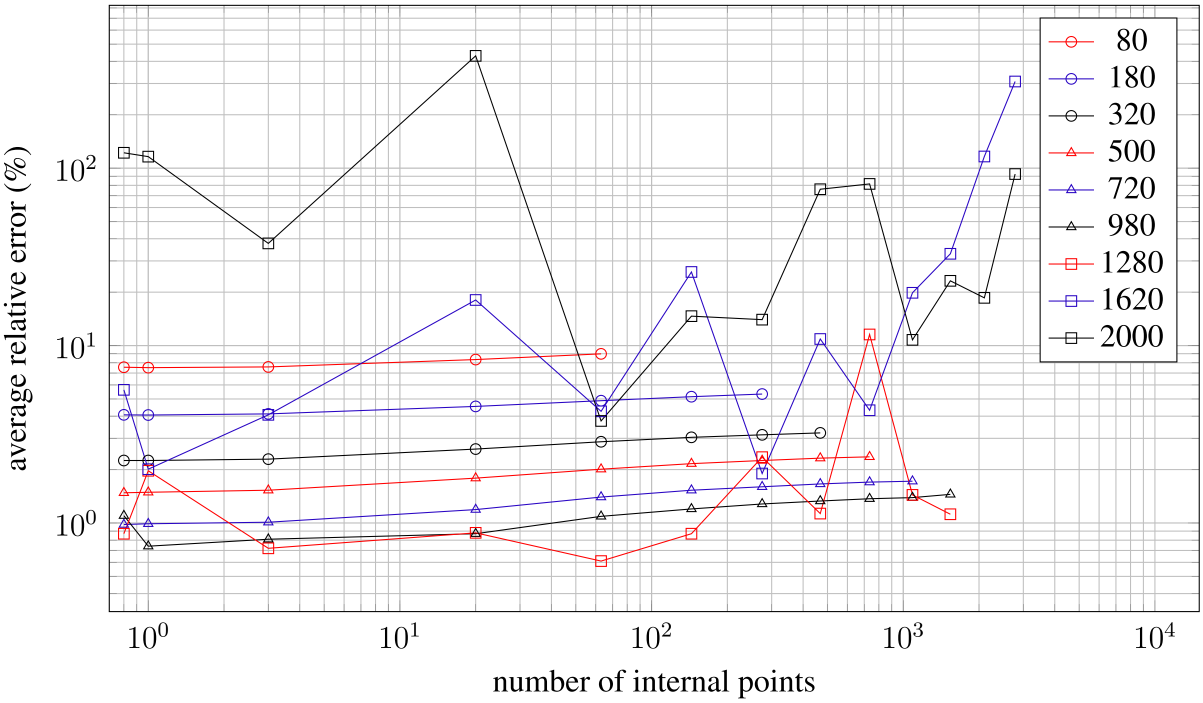

Figure 4.37 – Average relative error for displacement u_2 of the isotropic beam calculated by BESLE using function F5.

The average relative difference from ANSYS displacement results for orthotropic and anisotropic problems given in Figures 4.38 and 4.39 reiterate the isotropic results and support that this function is more vulnerable to stagnation errors than function F1. For this reason, this function should not be used in thermoelasticity.

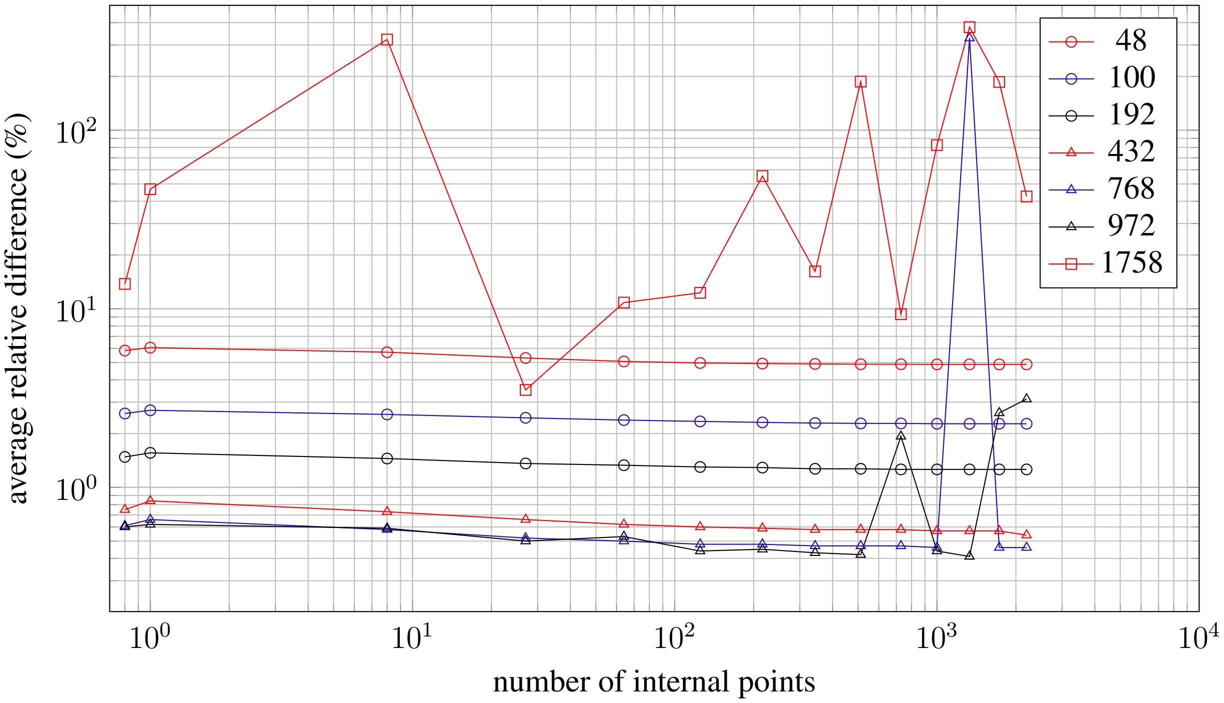

Figure 4.38 – Average relative difference from ANSYS for displacements u_1 calculated by BESLE using function F5.

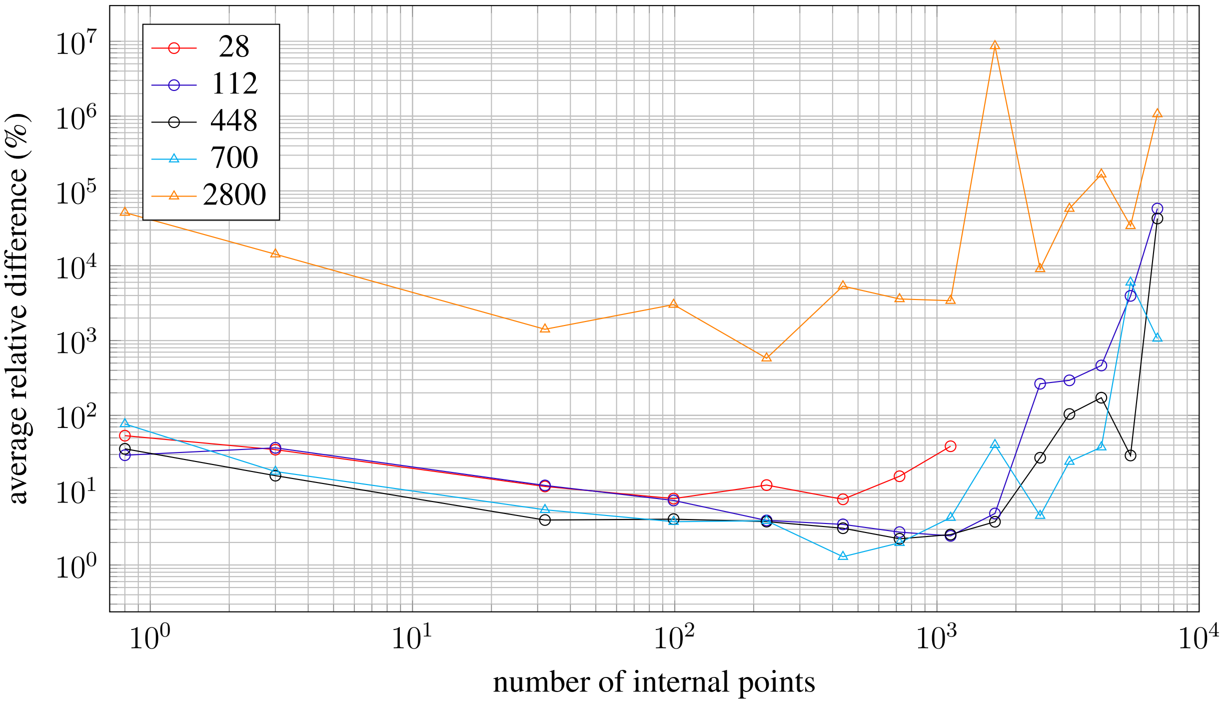

Figure 4.39 – Average relative difference from ANSYS for displacements u_3 at the orange line $(50, 0, x_3)$ of the anisotropic example calculated by BESLE using function F5.

4.4.3 Function F6

The results of this proposed function presented some differences from the ones obtained using function F1. Figure 4.40 shows the average relative error for the isotropic problem. For the refined meshes without internal points, function F6 achieved the minimum error of 0.61% against 0.92% for function F1. Both functions presented the same asymptotic behavior with the increasing number of internal points used and their accuracy is similar to each other with the use of a great number of internal points.

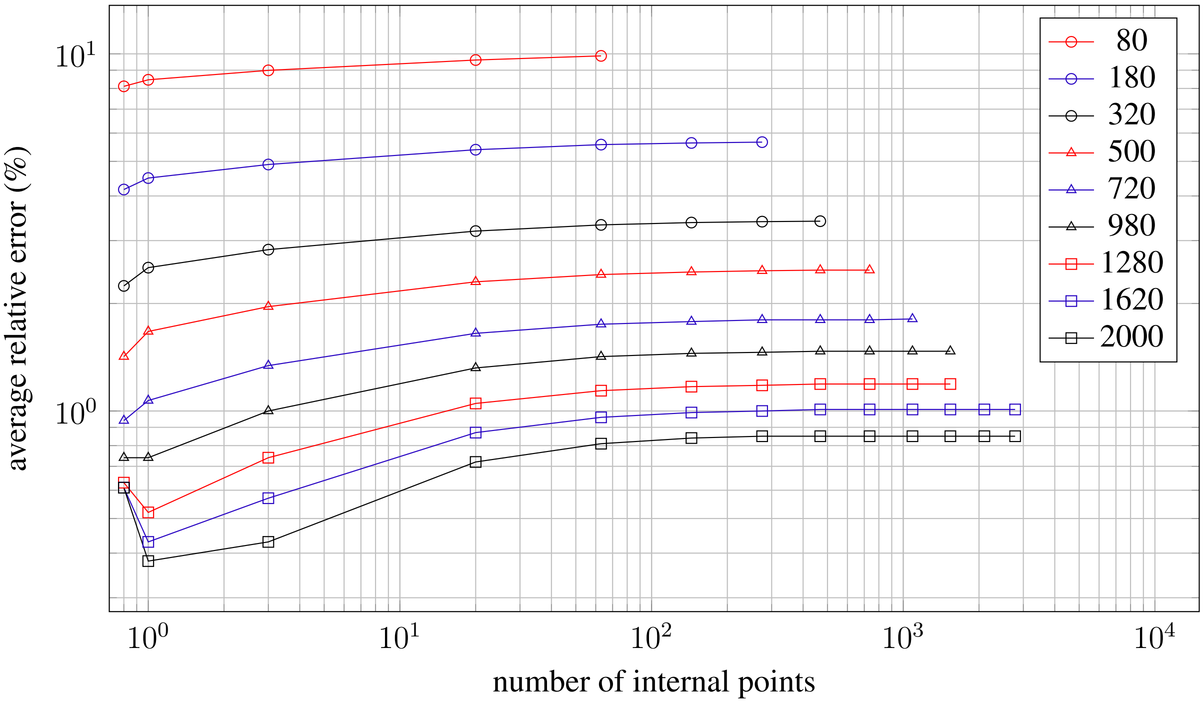

Figure 4.40 – Average relative error for displacement u_2 of the isotropic beam calculated by BESLE using function F6.

Figure 4.41 shows the relative difference from ANSYS for displacements for the orthotropic problem. It can be seen that the use of internal points did not produce significant improvement in the results. As the refinement increases, the results of function F6 keep improving with an average difference of 0.35% using 1758 elements with no internal points, better than function F1 which obtained 0.76%.

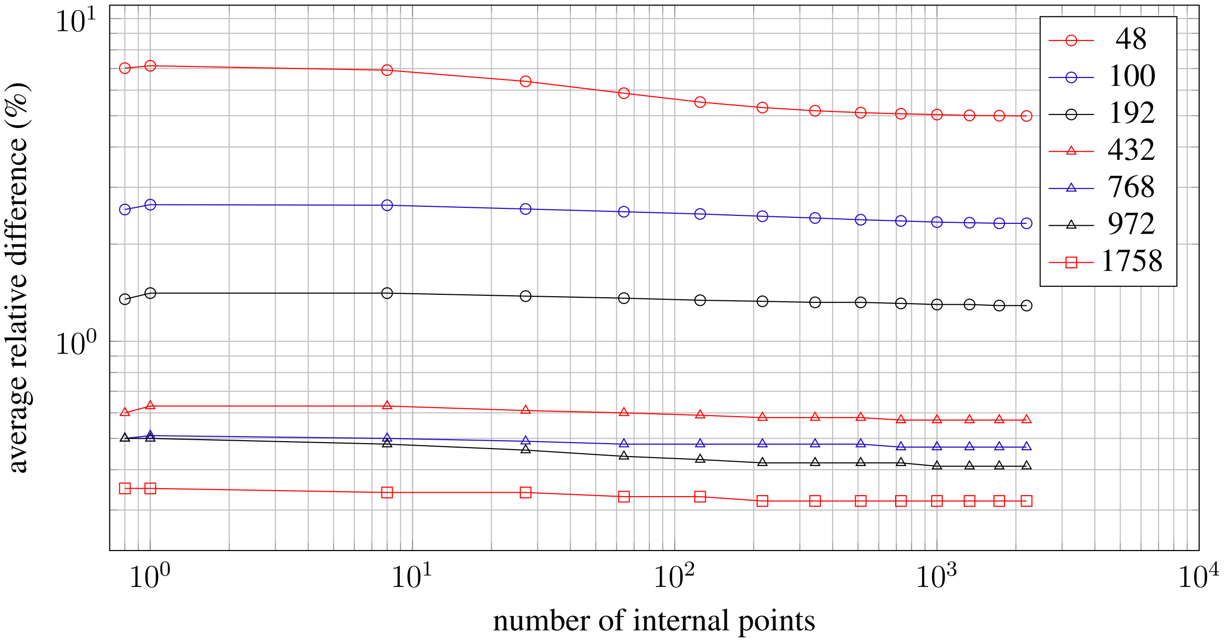

Figure 4.41 – Average relative difference from ANSYS for displacements u_1 calculated by BESLE using function F6.

For the anisotropic problem, the relative difference from ANSYS for displacements presented in Figure 4.42 shows no relevant difference from function F1. Accuracy levels, saturation, and stabilization of results are very similar to each other.

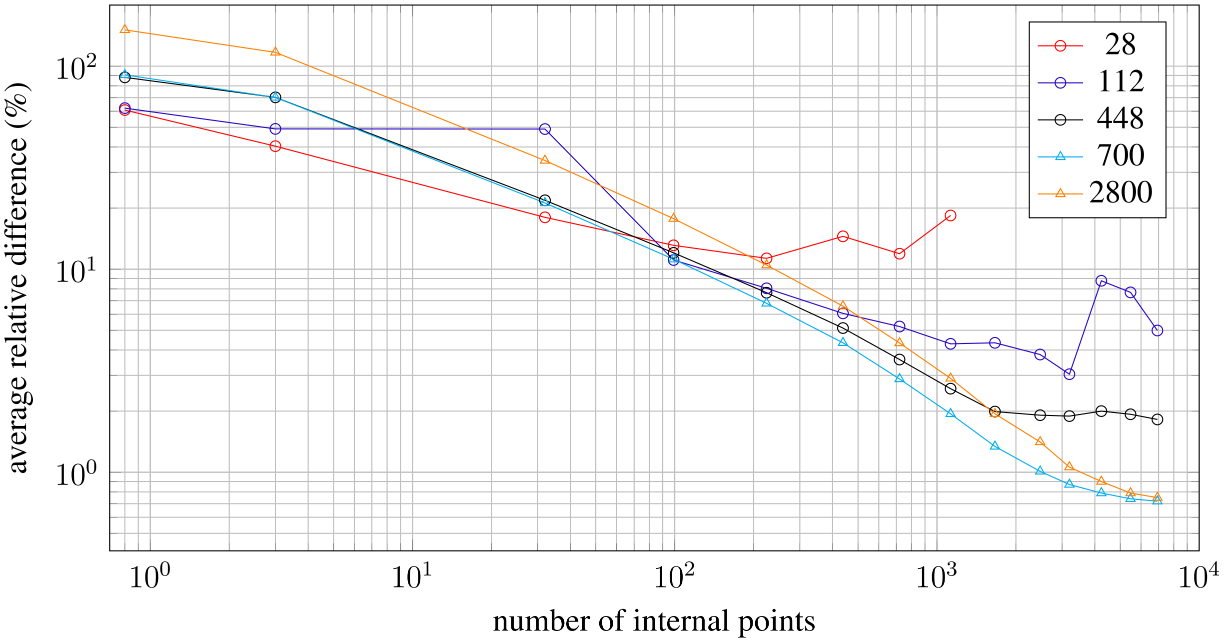

Figure 4.42 – Average relative difference from ANSYS for displacements u_3 at the orange line $(50, 0, x_3)$ of the anisotropic example calculated by BESLE using function F6.

4.4.4 Function F7

Function F7 is a higher order function than F6 and presented saturation like function F5. For the isotropic problem, the saturation effect appears at the mesh of 1280 elements when using 1088 internal points, as it can be seen by the average relative errors for displacements plotted in Figure 4.43, although the function F5 had saturated using less internal points with the same degree of mesh refinement (see Figure 4.37). Moreover, the mesh with 1620 elements was able to produce satisfactory results until the use of 64 internal points, while function F5 never demonstrated accuracy at this mesh. For the mesh of 2000 elements, both functions (F5 and F7) obtained results far from the reference.

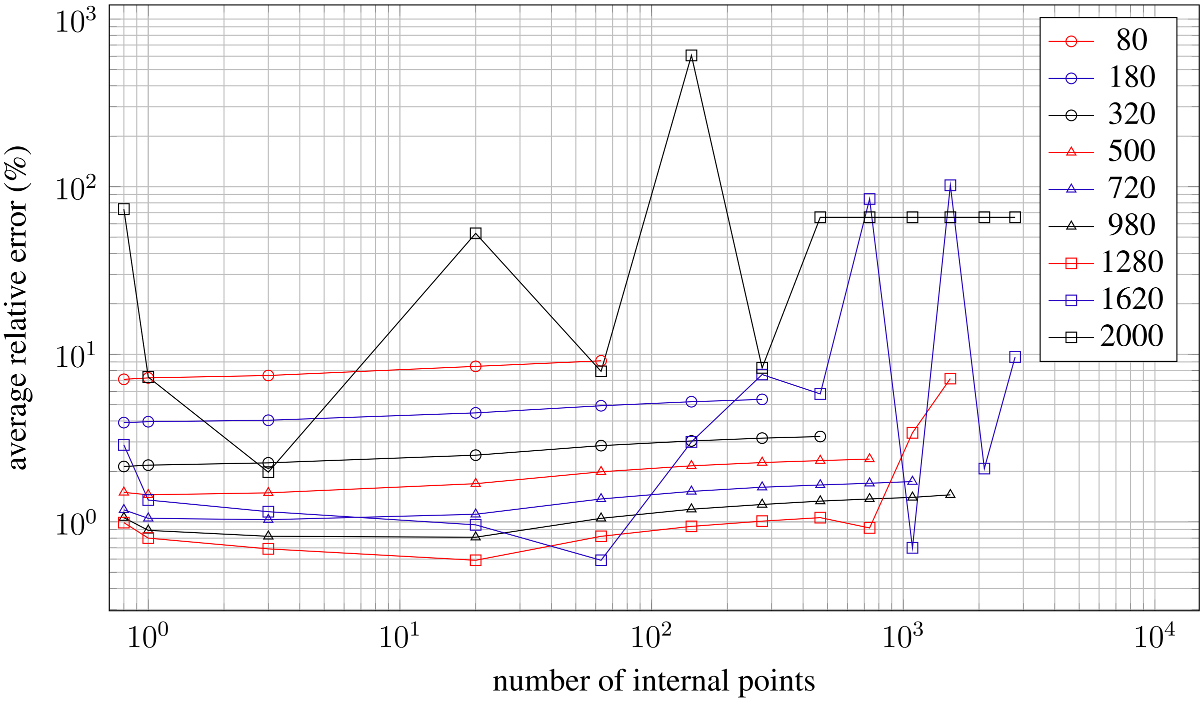

Figure 4.43 – Average relative error for displacement u_2 of the isotropic beam calculated by BESLE using function F7.

The saturation effect for the orthotropic cube only appears at the most refined mesh (1758 elements) for the function F7, demonstrated by the average relative difference for displacements shown in Figure 4.44. For function F5, the meshes of 768 and 972 also saturated (see Figure 4.38).

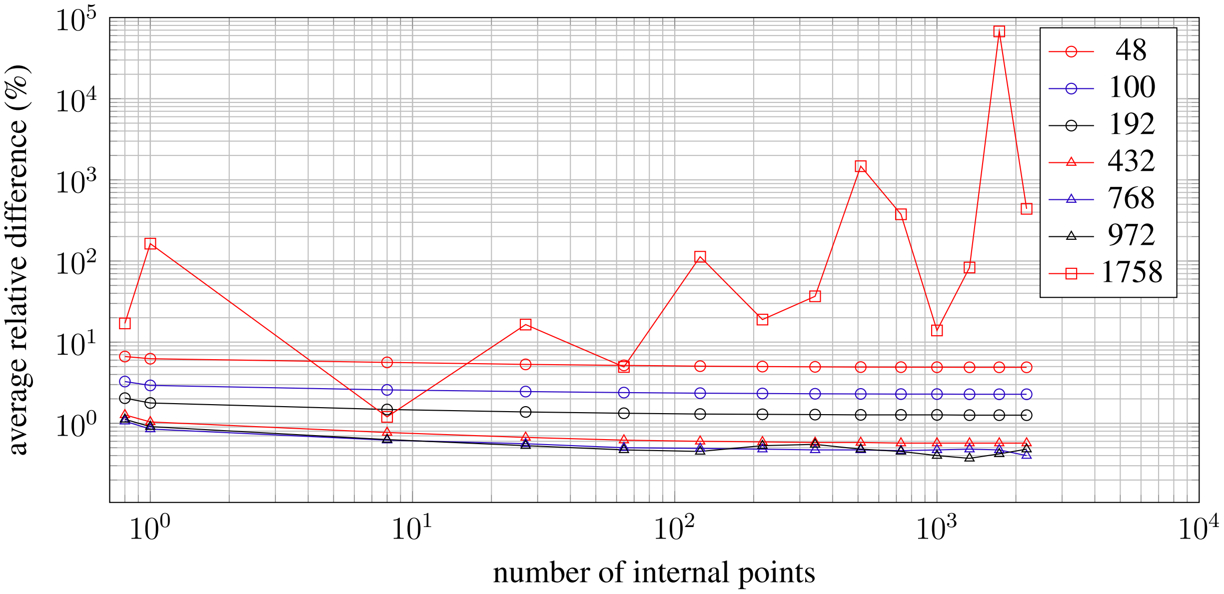

Figure 4.44 – Average relative difference from ANSYS for displacements u_1 calculated by BESLE using function F7.

The average relative difference results for the anisotropic problem using function F7 (Figure 4.45) are quite similar to the results of the function F6, but the mesh of 2800 elements saturated and lost accuracy when using 5472 internal points or more. It also performed better than function F5, which never had satisfactory accuracy (see Figure 4.39).

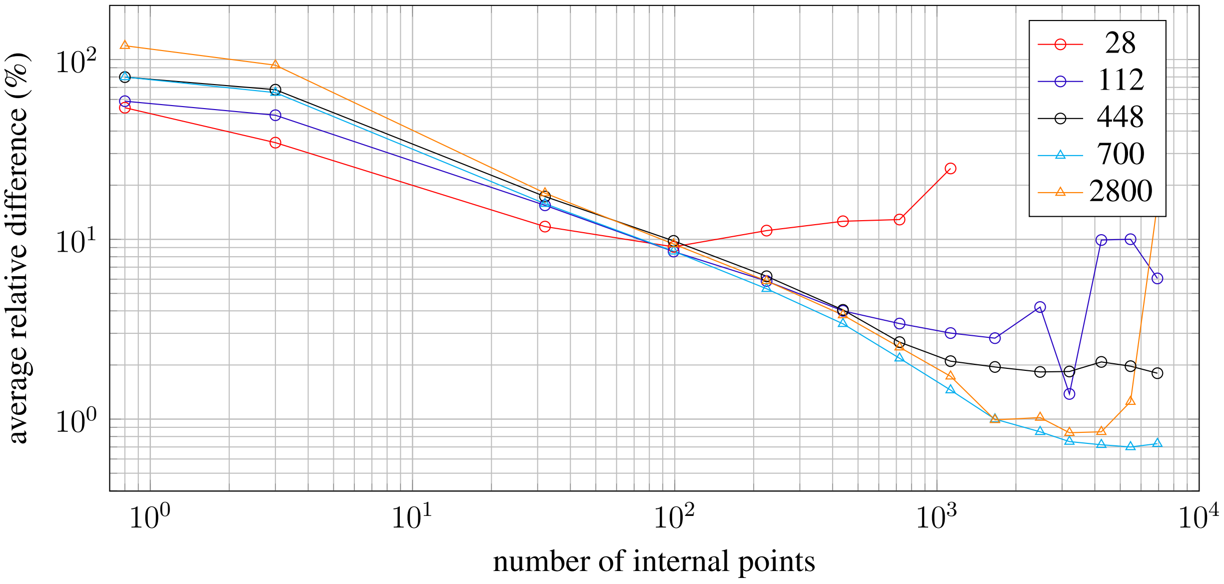

Figure 4.45 – Average relative difference from ANSYS for displacements u_3 at the orange line $(50, 0, x_3)$ of the anisotropic example calculated by BESLE using function F7.

4.5 Discussion of RBF test results

The results of Section 4.4 clearly show that the temperature interpolation function plays an important role in the final result. The combination of the mesh and the interpolation function used may induce the saturation and consequently, loss of accuracy or stagnation of the convergence of the solution, making the continuous mesh refinement inefficient to improve the overall quality of the results.

Saturation may arise with mesh refinement, followed or not by a reduction of the distance of the internal points used for temperature interpolation, depending on the problem. The first explanation for this phenomenon could be the approximation of internal points to the boundary, in a similar way that the calculation of values at internal points using the BIE tends not to produce good results if the points are close to the boundary, due to the singularity or quasi-singularity generated by the integral equations.

However, Figure 4.36 shows that the occurrence of saturation due to the increase in the number of internal points (and consequently reduction in the distance between them) is delayed at the anisotropic problem by the mesh refinement. Furthermore, Figure 4.43 shows that, depending on the interpolation function chosen, saturation can occur without internal points, simply by refining the mesh.

Some authors, like Karur and Ramachandran (1994), point out the poor conditioning of the interpolation matrix as a probable cause for the appearance of saturation, although this is not a consensus. Studies about the causes of saturation are outside the scope of this work, although the results allow us to affirm that the reduction of the distance of the interpolation points (by mesh refinement or increasing the number of internal points) increases the possibility of occurring the saturation, especially to high-order functions, which proved to be more susceptible to it.

A possible explanation for that may be understood by Figure 4.46 which shows the tested RBF F3 (red), F5 (blue), F6 (green), and F7 (orange). It can be seen that as r grows from zero, red and green lines (lower order functions) detach from $\phi = 1$ around $r = 0.2$, faster than blue and orange lines (higher-order functions) that need values of $r = 0.4$. It means that the calculated values of the interpolation function may be very similar for interpolation points near each other, and consequently, the values of different lines of the matrix $[\boldsymbol{E}]$ of Equation 2.142 become similar, what can make its determinant become close to zero and create numerical problems to calculate the inverse matrix used at Equation 2.146.

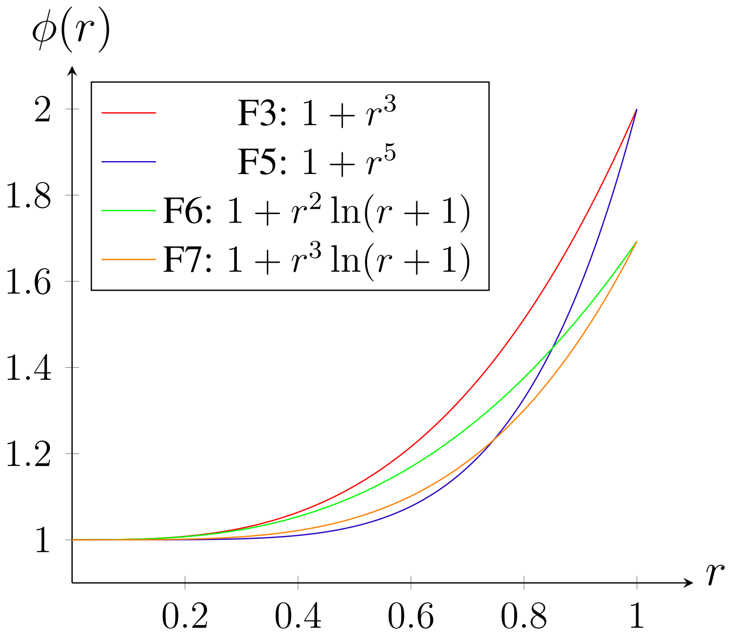

Figure 4.46 – Anisotropic thin plate.

Another consequence is that the low-order functions F3 and F6 may also saturate, but they require meshes much more refined. In other words, they are stronger against saturation, which was verified through the numerical experiments done.

4.6 Anisotropic Thin Plate

The thin plate of Figure 4.47 is a problem analyzed in Shiah and Tan (2016b), dimensioned with $L = 8$, and the origin of the cartesian coordinates placed at the center of the plate.

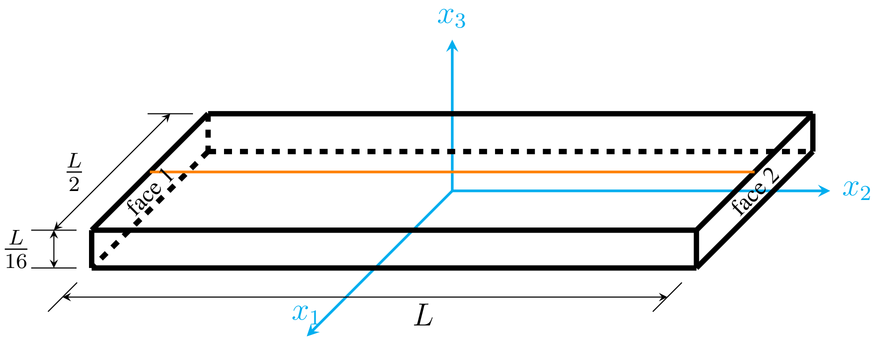

Figure 4.47 – Anisotropic thin plate.

Face 1 was set $\theta = 0$ ºC while face 2 was set $\theta = 100$ ºC, and both of them are fully restricted for displacements. All of the other faces are insulated and free. The material used is alumina Al_2O_3, with elasticity stiffness tensor given by Equation 4.21.

$$\mathbf{C} = \begin{bmatrix} 465 & 124 & 117 & 101 & 0 & 0 \\ 124 & 0 & 0 & 0 & 0 & 0 \\ 117 & 0 & 563 & 0 & 0 & 0 \\ 101 & 0 & 0 & 233 & 0 & 0 \\ 0 & 0 & 0 & 0 & 0 & 0 \\ 0 & 0 & 0 & 0 & 0 & 0 \end{bmatrix} GPa \tag{4.21}$$

The conductivity and the expansion tensors are given respectively by Equations 4.22 and 4.23.

$$\boldsymbol{\kappa} = \begin{bmatrix} 18 & 0 & 0 \\ 0 & 10 & 0 \\ 0 & 0 & 25 \end{bmatrix} W/m^oC \tag{4.22}$$

$$\boldsymbol{\alpha} = \begin{bmatrix} 8.1 & 0 & 0 \\ 0 & 5.4 & 0 \\ 0 & 0 & 9.2 \end{bmatrix} \times 10^{-6}\ ^oC^{-1} \tag{4.23}$$

The principal axes for the materials properties were rotated with respect to the x_3-, x_1-, and x_2- axis by 60º, 45º and 30º counterclockwise, respectively and in succession, creating a generally anisotropic analysis. Then, the material properties are rotated to match the cartesian coordinates, given by Equations 4.24 to 4.26.

$$\mathbf{C} = \begin{bmatrix} 620.616 & 53.593 & 87.202 & 39.992 & -18.414 & -58.115 \\ 53.593 & 513.175 & 140.699 & 73.644 & 6.364 & 65.699 \\ 87.202 & 140.699 & 512.227 & -106.569 & 55.535 & 1.423 \\ 39.992 & 73.644 & -106.569 & 214.376 & 8.301 & 39.574 \\ -18.414 & 6.364 & 55.535 & 8.301 & 202.085 & 45.390 \\ -58.115 & 65.699 & 1.423 & 39.574 & 45.390 & 143.531 \end{bmatrix} GPa \tag{4.24}$$

$$\boldsymbol{\kappa} = \begin{bmatrix} 19.262 & 2.425 & 6.809 \\ 2.425 & 17.113 & -1.456 \\ 6.809 & -1.456 & 16.625 \end{bmatrix} W/m^oC \tag{4.25}$$

$$\boldsymbol{\alpha} = \begin{bmatrix} 7.75731 & 0.69343 & 1.69477 \\ 0.69343 & 7.78019 & -0.58957 \\ 1.69477 & -0.58957 & 7.16250 \end{bmatrix} \times 10^{-6}\ ^oC^{-1} \tag{4.26}$$

Shiah and Tan (2016b) used the Finite Element Method results obtained by ANSYS with 83,780 elements of SOLID226 type (quadratic 20-node cube element) as a reference for the results. They also solved using 352 quadratic rectangular Boundary Elements (ANSYS and BEM meshes are shown in Figure 4.48), and obtained good agreement between the two methods. It is worth observing that Shiah and Tan (2016b) used the Direct Domain Mapping to solve the volume integral of the Boundary Integral Equation, and the same fundamental solution for elasticity used in this thesis.

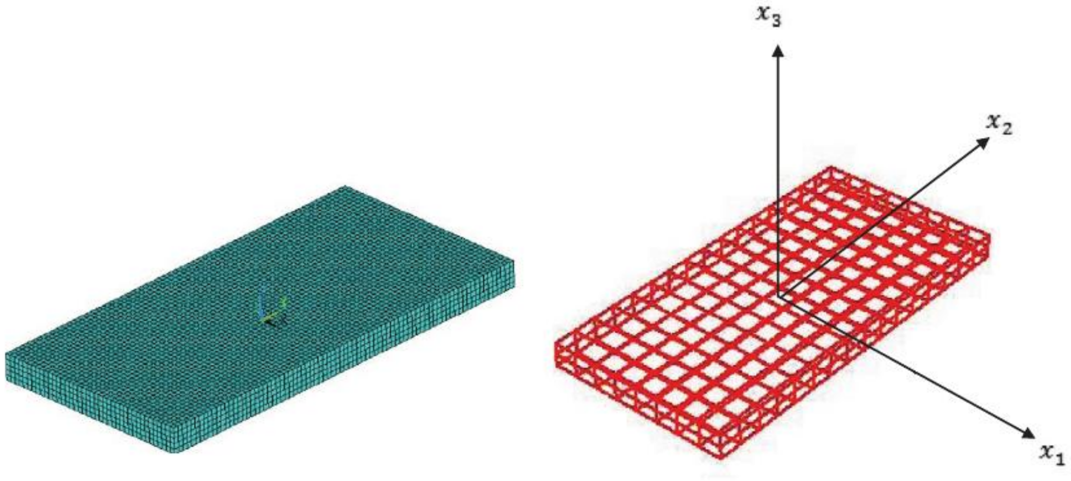

Figure 4.48 – ANSYS FEM (left) and BEM (right) meshes used by Shiah and Tan (2016b). Adapted from: (Shiah; Tan, 2016b).

The results compared were the normalized total displacements $\bar{u}_0$ (Equation 4.27) and the normalized von Mises stress $\bar{\sigma}_0$ (Equation 4.28) along the line $(0, x_2, 0.25)$, or else, the top face.

$$\bar{u}_0 = \frac{u_0}{L\alpha_{11}\Delta\theta} \tag{4.27}$$

$$\bar{\sigma}_0 = \frac{\sigma_0}{C_{11}\alpha_{11}\Delta\theta} \tag{4.28}$$

where L is the plate lenght at x_2 direction, $\Delta\theta = 100^oC$, and

$$u_o = \sqrt{u_1^2 + u_2^2 + u_3^2} \tag{4.29}$$

The analysis with BESLE was performed by using the same mesh size used by the BEM code of Shiah and Tan (2016b), but linear triangle elements instead, which increased the total number of elements to 704. It was analyzed the results obtained using Radial Basis Functions F3 and F6, combined with some internal points. From Figures 4.49 to 4.52, the continuous and the dashed lines are the reference results obtained by Shiah and Tan (2016b) using ANSYS FEM and BEM respectively, and they are almost indistinguishable. The other entries in the legend indicate the RBF used (F3 or F6) and the number of internal points (IP) used at each experiment.

Figure 4.49 shows that the normalized displacements obtained using the functions F3 and F6 without internal points are close to the reference results, while the ones obtained using internal points are detached from the reference. Moreover, increasing the number of internal points increased the loss of accuracy, an indication that saturation appeared. Since boundary nodes are interpolation points, any internal point at the thin plate is so close to boundary nodes that induces saturation and loss of accuracy at displacement results.

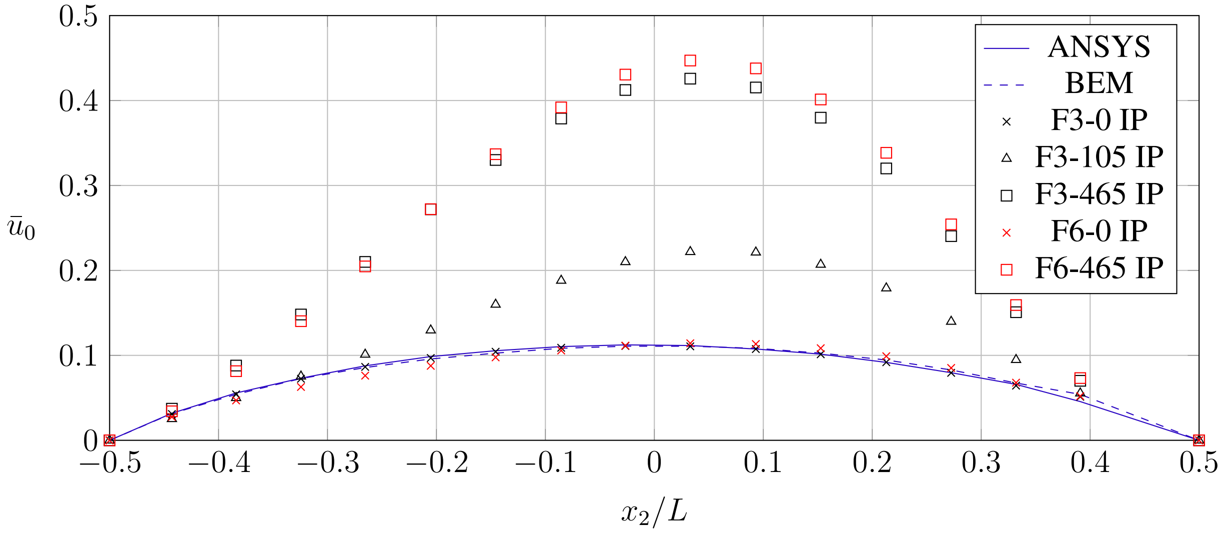

Figure 4.49 – Resultant normalized displacement along the orange line $(0, x_2, 0.25)$.

For the results without internal points, function F3 followed very well the reference results, while function F6 stepped away from them. This can be better viewed in Figure 4.50.

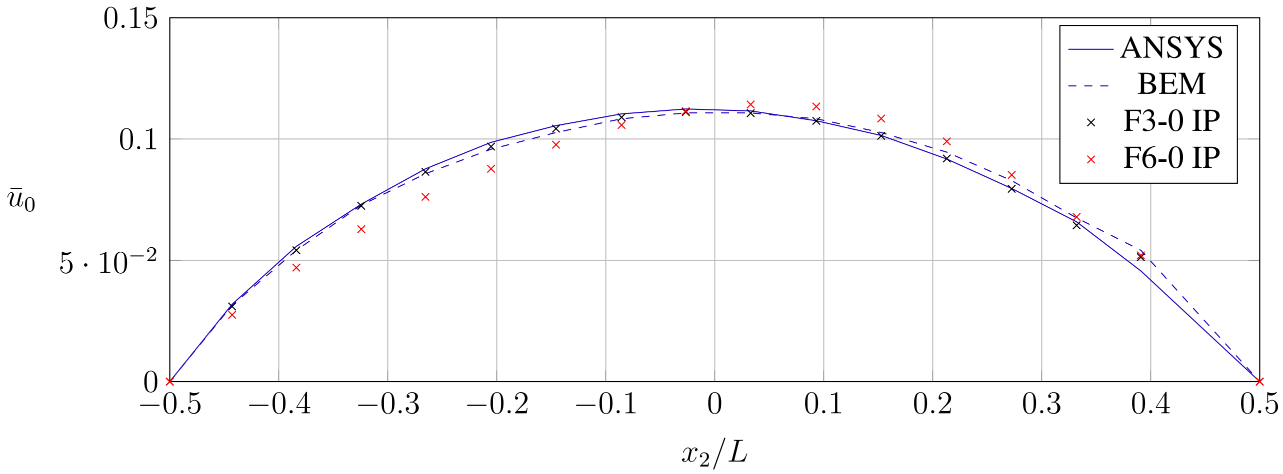

Figure 4.50 – Resultant normalized displacement along the orange line $(0, x_2, 0.25)$.

The normalized von Mises stresses are presented in Figure 4.51. Since the stresses are dependent on the quality of the displacement results, the stresses calculated by BESLE at the simulations using internal points were far off the reference, while the analysis without internal points showed good agreement. It is worth noting that Shiah and Tan (2016b) did not present results for the stresses at the fixed ends ($x_2/L = -0.5$ and $x_2/L = 0.5$) and no reason for this was given.

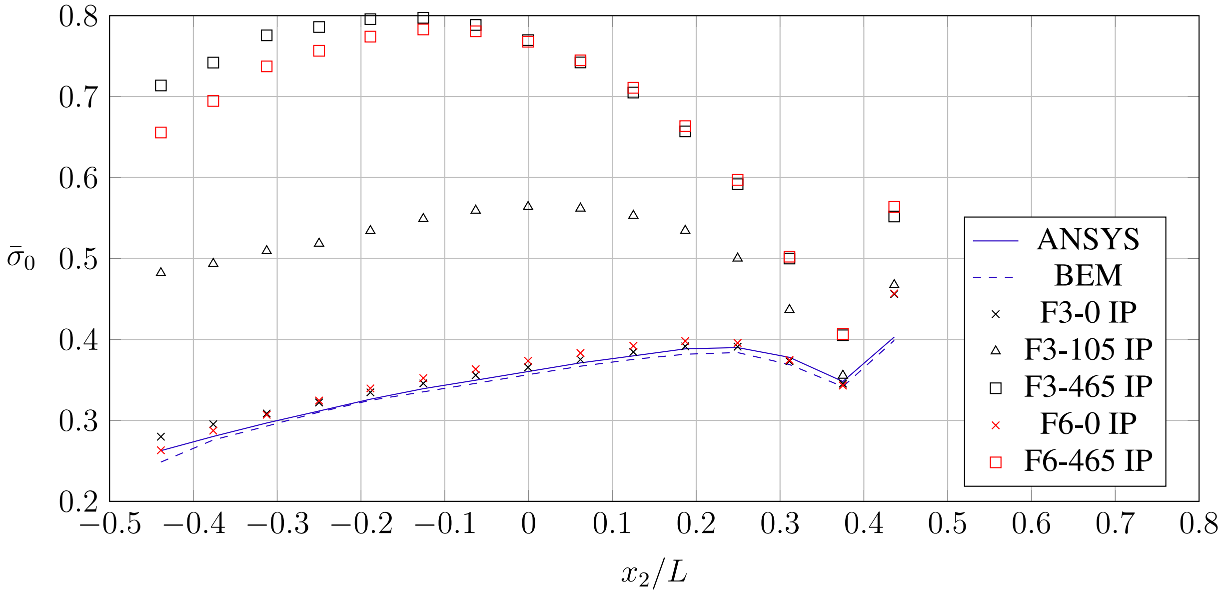

Figure 4.51 – Normalized von Mises stress along the orange line $(0, x_2, 0.25)$.

As it was done for the displacements, only the results obtained without using internal points are presented in Figure 4.52. It can be seen that the small difference in the calculated displacements between the functions F3 and F6 produced a small difference in the stresses, more favorable to the function F3.

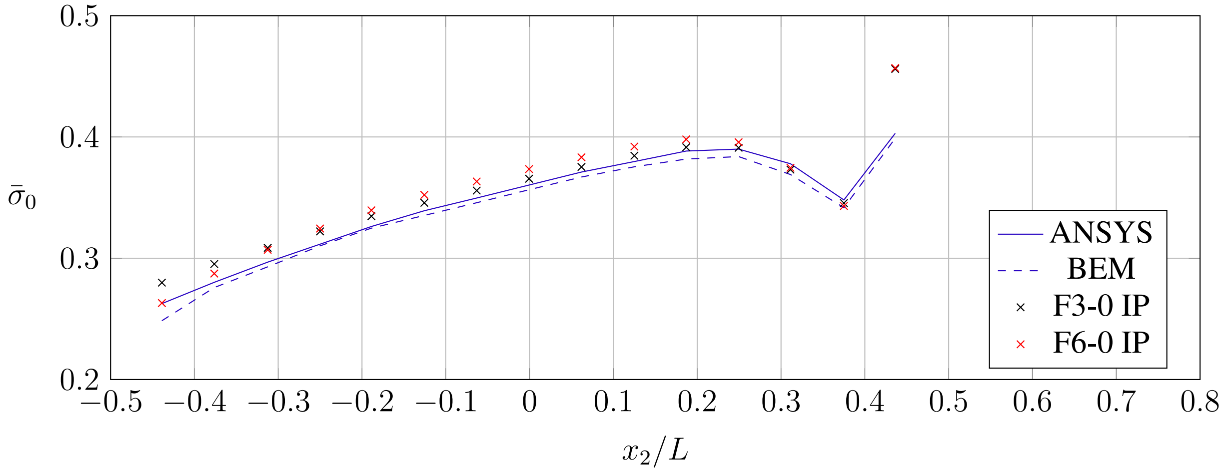

Figure 4.52 – Normalized von Mises stress along the orange line $(0, x_2, 0.25)$.

4.7 Subregions effect

The results of Section 4.3.5 demonstrated that the use of internal points may be necessary in some cases to achieve good results. Nevertheless, BESLE does not have a tool to compute internal points automatically for any geometry, so it is necessary to calculate them manually, and then, BESLE only reads them.

The use of internal points allows better interpolation of the thermal field and the interfaces of the subregions may do this rule. There are some advantages of doing this: first, BESLE is ready to deal with subregions; second, despite of increasing the number of elements, a source point is integrated only over the elements of its subregion, i.e, the integration is done over a smaller number of elements, reducing the time to compute the matrices $[\boldsymbol{H}]$ and $[\boldsymbol{G}]$; third, the subregions formulation produces a sparse linear system to be solved, and BESLE linear system solver takes advantage of this characteristic, speeding up the solution; fourth, since null values are not stored, the usage of memory is also reduced, allowing to deal with very refined meshes with the same hardware.

The dashed lines of Figure 4.53 demonstrate the different subregions created for the problem of Section 4.3.5, and the names to identify them are on the same Figure. The size of the elements is the same as the simple region using 700 elements, used for time simulation comparison.

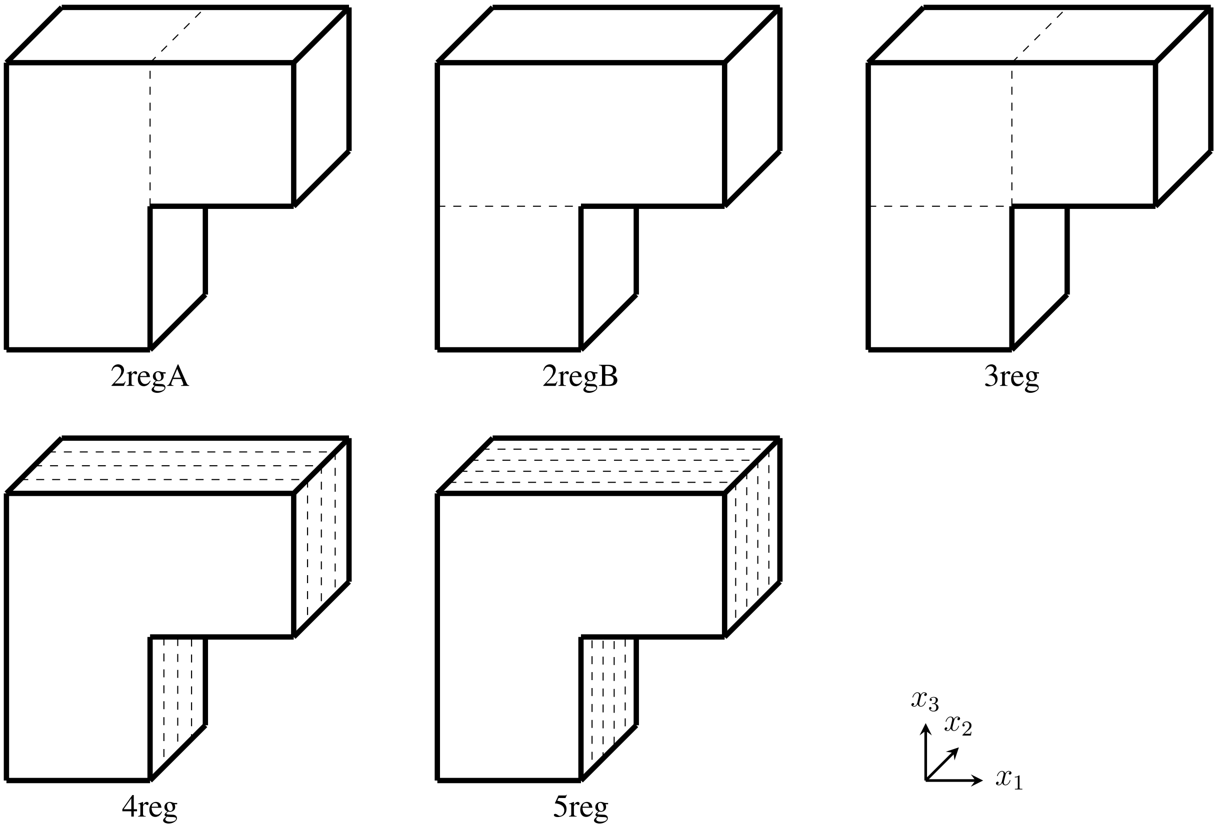
2regA 2regB 3reg 4reg 5reg

Figure 4.53 – The various subregions divisions of the anisotropic problem. Dashed lines mean interfaces.

The Figure 4.54 presents the displacements u_3 calculated at the line $(50, 0, x_3)$. The blue line is the quadratic Finite Element reference, while the marked points are the results obtained from the various subregions divisions plus the one region, all without internal points and using the interpolation function F3 of Table 4.2. It can be seen that all results using subregions are better than the simple regions, but the division using 3 regions was unable to represent the solution. All other subregions divisions are close to the FEM solution.

The interpolation function F6 was also used, but since no significant difference was obtained, the results are not presented.

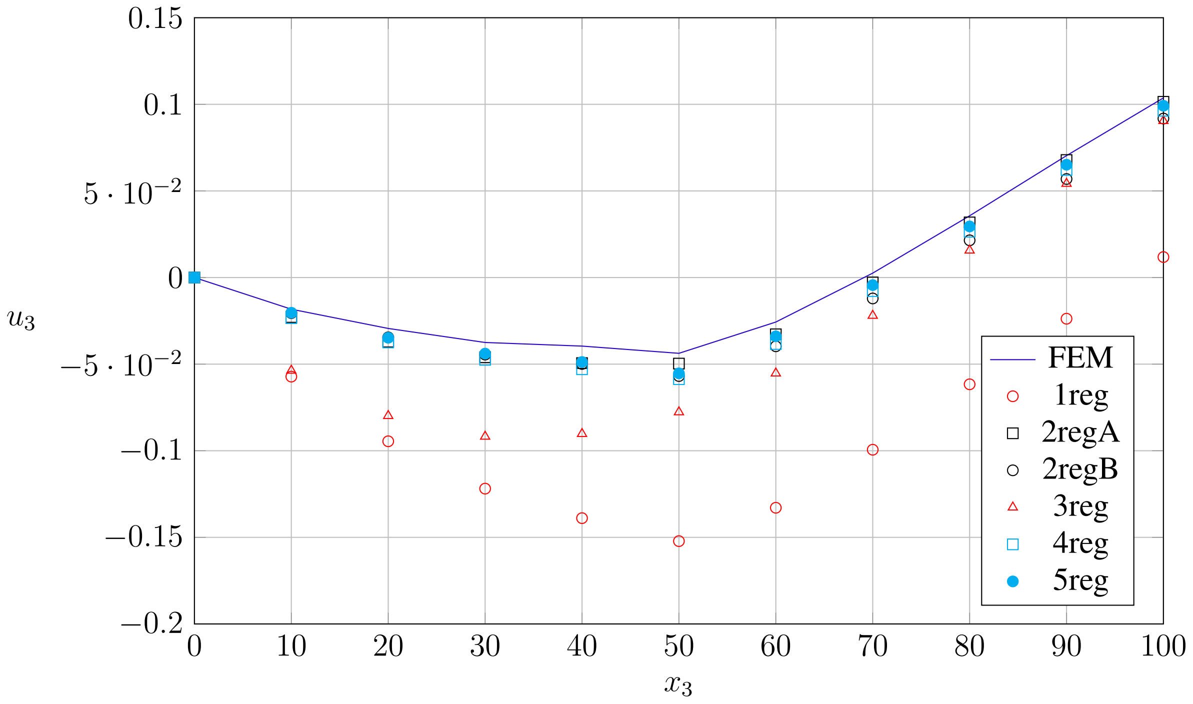

Figure 4.54 – Displacements u_3 calculated at the line $(50, 0, x_3)$ for different subregions divisions.

The simulations were performed at the Dell Workstation OptiPlex 7071 Tower, equipped with an Intel@Core i9-9900 processor of 3.1 GHz, presenting 8 cores and 2 threads by core in a total of 16 CPU, 128 GB of RAM memory, and NVIDIA GeForce RTX 2080. Table 4.3 presents the time spent in seconds by each analysis. The division into 2 regions has different numbers of elements at each one, while all other divisions have the same amount. The subdivisions into 4 and 5 elements, as it was done, made the total time increase compared with the single region solution. For 2 and 3 regions, the total time decreased. The total time of the simulation depends on the combination of the number of regions and the number of elements at each one, and if not done properly it can increase the total time simulation.

Table 4.3 – Number of elements and total time simulation for different subdivisions.

Simulation	Total number of elements	Elements per region	Time spent (s)
1reg	700	700	372
2regA	800	300 / 500	249
2regB	800	500 / 300	249
3reg	900	300	193
4reg	1520	380	418
5reg	1900	380	531

Figure 4.54 and Table 4.3 show clearly that solution accuracy and time are depen-

dent on how the subregions are created. In order to elucidate this matter, the subregions division was also applied at the orthotropic cube of Section 4.3.4 as shown in Figure 4.55. The elements have the same size as the mesh of a single region with 1728 elements.

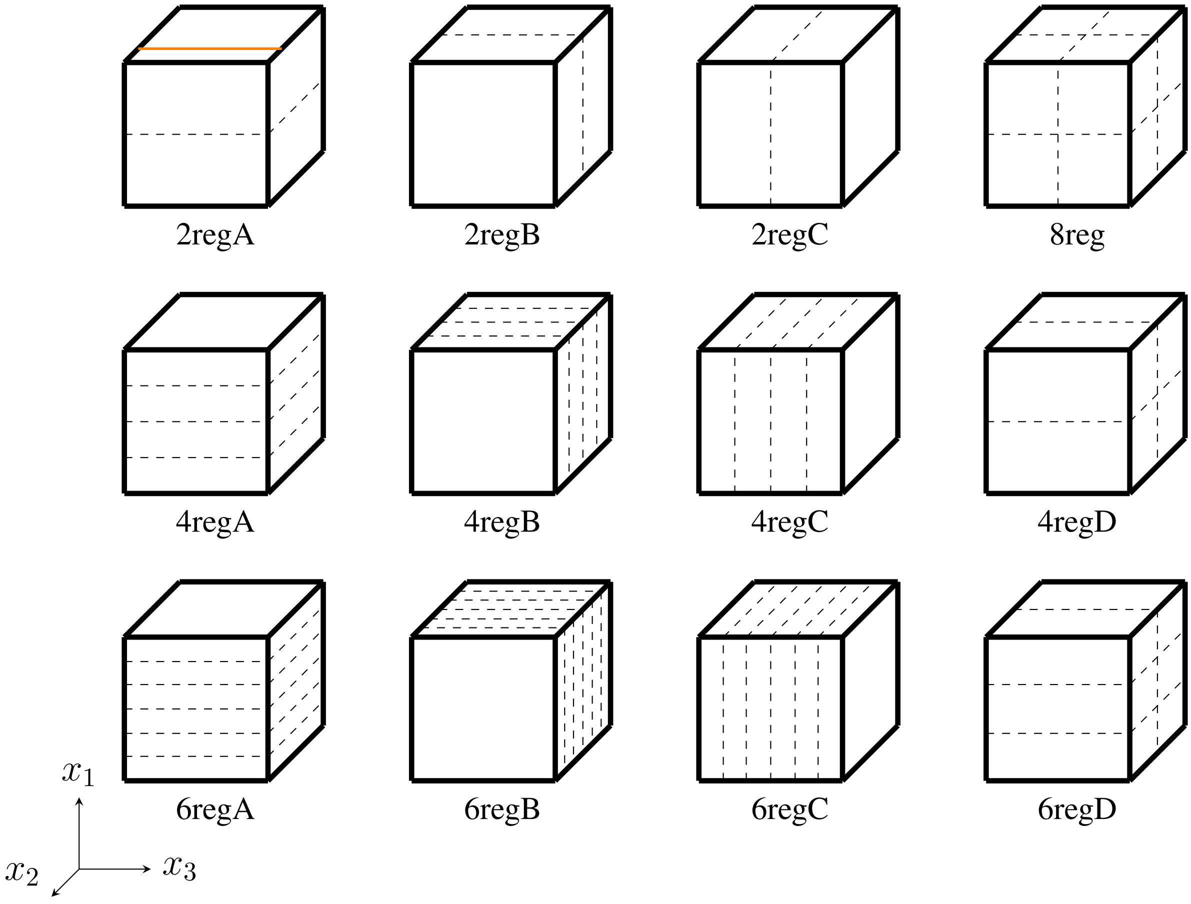

Figure 4.55 – The various subregions divisions of the orthotropic cube.

The displacements u_1, u_2, and u_3 calculated along the line $(x_1, 1, 0.75)$ were compared to the ANSYS results, and the average relative difference for each subregion is given in Table 4.4. Also, each geometry was tested with interpolation functions F3 and F6 of Table 4.2. All results were obtained without using internal points.

The results for a single region are the closest to the ANSYS solution. When the region is sliced along x_1 direction (simulations 2regA, 4regA, and 6regA), the accuracy of displacements u_1 decreases significantly. Moreover, function F6, which performed better for a single region, performed worse with subregions. The accuracy of displacements u_2 and u_3 also decreased, less than u_1.

The same behavior can be noted for displacements u_2 when the divisions are done along the x_2 direction, concerning the loss in accuracy (simulations 2regB, 4regB, and 6regB).

As the number of regions increases, the difference in the results also increases, faster for function F6. The results obtained for u_1 displacements using F6 with these simulations became quite worse.

For divisions created along x_3 direction, displacements u_3 were affected negatively (simulation 2regC, 4regC, and 6regC), with increasing loss of accuracy as more regions were defined, with the function F6 presenting more sensibility than F3, with reflexes to the displacements u_1.

The simulation 4regD consists of dividing the cube along directions x_1 and x_2, with one division at each one. The loss in accuracy is more pronounced for displacements u_1 and u_2, but this time the function F3 performed worse than F6. The simulation 6regD differs from 4regD by adding one more division to the x_1 direction, and surprisingly, the results recovered lots of accuracy.

The simulation 8reg was the result of making one division at each of the cartesian directions, and the results demonstrate not much loss of accuracy, being more pronounced at direction x_3.

Table 4.4 – Average relative difference to ANSYS displacements calculated along the orange line $(x_1, 1, 0.75)$ of Figure 4.55 for various subregions divisions. Values in percentage.

Simulation	u_1		u_2		u_3	
	F3	F6	F3	F6	F3	F6
1reg	0.61	0.43	0.84	0.78	0.65	0.58
2regA	4.21	4.80	1.07	1.14	2.50	2.53
2regB	1.99	2.95	7.13	8.56	2.10	2.09
2regC	1.30	1.05	1.16	1.15	8.98	12.74
4regA	5.31	8.98	0.89	1.07	2.52	2.68
4regB	4.63	13.10	9.93	20.95	2.20	2.13
4regC	0.98	5.00	0.76	0.92	15.57	36.17
6regA	4.99	13.87	0.79	1.04	2.48	2.79
6regB	3.70	25.36	8.50	35.65	2.29	2.18
6regC	0.77	10.68	0.76	0.95	13.46	63.84
4regD	8.62	5.76	11.38	6.11	3.41	2.69
6regD	2.24	2.25	2.20	1.45	2.42	2.40
8reg	3.81	3.50	1.61	1.24	5.49	4.73

The results obtained with subregions were all less accurate than the ones obtained with a single region. The use of subregions introduces fictitious boundaries inside the domain, with unknown displacements and tractions values, which are approximated by linear shape functions. By doing this, another source of error that doesn’t exist at the single region mesh is added to the equations, reducing the accuracy of the results. Maybe, better results could be obtained by using shape functions of higher order.

In the meanwhile, the subregions should not be used, being a limitation to this formulation using the Dual Reciprocity Method, since bodies composed of different materials require the use of subregions methodology.

5 CONCLUSIONS

In this thesis, uncoupled thermoelastic formulation for static problems was implemented in BESLE code, a Boundary Element software for elastic and elastodynamic analysis, that uses the fundamental solution based on Barnett-Lothe tensor and Double Fourier series, being able to deal with isotropic or general anisotropic material. The thermoelasticity implementation is ready to work with known temperature fields dependent on the cartesian coordinates or potential field computed by the implemented formulation.

The BEM solver for potential problems was successfully implemented using the classical 3D isotropic fundamental solution and Direct Domain Mapping (DDM), as well as the evaluation of the temperature at points inside the domain. Some examples were used to validate the potential solution, including one anisotropic bidimensional with subregions, demonstrating that the three-dimensional formulation is adequate to solve 2D problems.

The thermoelastic formulation included a volume integral at the Boundary Integral Equation solved by the Dual Reciprocity Method which required the use of two Radial Basis Functions: one for the particular solution of the elasticity, and another to interpolate the gradient of the thermal field. The last one was obtained by using the RBF to interpolate the temperature field, calculating the coefficients of interpolation, and then, deriving it with respect to the cartesian coordinates. This methodology was suitable to solve some problems using only boundary nodes except for thermal fields with strong variations, in which the use of internal points for temperature interpolation was mandatory to achieve satisfactory results.

The stresses and strains at the boundary were evaluated using the shape functions, including the thermoelasticity effects at the formulation presented by Kane (1994). This formulation avoids the calculation of integrals and singularity effects and the results obtained were very good, despite some small edge effects which are a consequence of the use of linear elements.

Different zero-parameter RBF were used for temperature interpolation and they presented an important influence on the accuracy of the results. The use of high-order functions demonstrated sensibility to saturation effect when reducing the element size or reducing the distance of internal points, losing the capacity to deliver a representative solution, and therefore their use must be avoided. The reference function F1 presented the same results as the function

F3, so the last one can be used instead of F1 since fewer calculations are done. Moreover, the cubic RBF (F3) and the proposed modified thin plate spline (F6) were the only non-zero parameter functions tested reliably to be used as temperature interpolation functions, but the last one should be avoided for thin plate problems.

Although they might not be necessary, the use of internal points for temperature interpolation has the potential to increase the accuracy of the solution, which depends on the mesh refinement. The results demonstrated that as the mesh is refined, the number of internal points to achieve the minimum error also increases. On the other hand, for thin geometries the boundary interpolation nodes are so close enough that adding internal points induces saturation and loss of accuracy, and therefore they should not be used.

The subregions method was applied as an attempt to use the interfaces as internal points, taking advantage of the subregions procedure to generate sparse matrices and reduce the computing time. The time spent is dependent on how the subregions are created, and may even increase the total solution time. Moreover, despite the increase in accuracy of the results at some conditions, this was not a general behavior, and the subregions division reduced the accuracy at conditions in which they were unnecessary.

In short, the simulation conditions that guarantee reliable solutions consist of using the cubic RBF and a reasonable mesh refinement combined with a great number of internal points, despite the drawback of increasing the computational cost, except for the thin plate problems, in which the use of internal points is undesirable.

5.1 Future works

The results of the Dual Reciprocity Method demonstrated great dependence on the RBF used for the interpolation of the gradient of temperature. So, deep investigations for the different Radial Basis Functions should be performed, like considering the number of conditioning of the interpolation matrix, the use of augmented polynomial RBF, RBF with shape parameter and methods to evaluate the optimal shape parameter, the use of RBF-FD technique, and the procedure presented by Mai-Duy and Tran-Cong (2003) named Indirect Radial Basis Function Network, which consists in proposing the functions to interpolate the derivatives, and then, integrating to find the function that interpolates the potential field.

The DRM applied to thermoelasticity as proposed by Gao (2003) requires the use of two RBF, meaning that two interpolation matrices will need to be inverted, which can be of high computational cost. Then, other methods for evaluating the domain integral can be investigated, like Radial Integration and Direct Interpolation Boundary Element Methods, and maybe, less computational cost, better accuracy, and fewer considerations about the reliability of the functions can be achieved.

Moreover, the two RBF required (particular solution for elasticity and temperature interpolation) may present some kind of resonance, so, the fact that both functions are cubic may not be a coincidence, like the Galerkin Method for the Weighted Residual Method, which uses the same functions for approximation and weighting. Then, different combinations of these two functions can be studied.

The subregions technique is not reliable at this point, but it has the potential to generate accurate results. The use of shape functions of high order for the interpolation of the variable fields at the elements may be performed, combined or not with the considerations just made for the Radial Basis Functions.

Finally, the code implementations were done at BESLE amplifying the type of problems that this software can solve. This new version will be published to be available to the community, as well as new documentation explaining the changes and the use of the free and open-source Blender software as a possibility to generate the meshes, allowing a non-user of BESLE become able to make simulations by his own.

BIBLIOGRAPHY

Aliabadi, F. M. H. **The Boundary Element Method**: Applications in solids and structures. Chichester: Wiley, 2002. v. 2.

Banerjee, P. K. **The Boundary Element Methods in Engineering**. London: McGrall Hill, 1994.

Banerjee, P. K.; Lejeune, A. **Boundary Element Methods in Engineering Science**. Maidenhead: McGraw-Hill, 1981.

Bayona, V. An insight into rbf-fd approximations augmented with polynomials. **Computers and Mathematics with Applications**, v. 77, p. 2337–2353, 2019.

Bebendorf, M. Approximation of boundary element matrices. **Numerische Mathematik**, v. 86, p. 565–589, 2000.

Brebbia, C. A.; Chang, O. V. Boundary elements applied to seepage problems in zoned anisotropic soils. **Advances in Engineering Software**, v. 1, p. 95–105, 1979.

Brebbia, C. A.; Dominguez, J. **Boundary Elements:**: An introductory course. Southampton: WIT Press, 1992.

Brebbia, C. A.; Nardini, D. Dynamic analysis in solid mechanics by an alternative boundary element procedure. **Soil Dynamics and Earthquake Engineering**, v. 65, p. 147–164, 1983.

Clements, D. L.; Budhi, W. S. A boundary element method for the solution of a class of steady-state problems for anisotropic media. **Journal of Heat Transfer**, v. 121, p. 462–465, 1999.

Cravo, A. G. S. **Análise de Problemas de Anisotropia 3D com Sub Regiões Utilizando o Método dos Elementos de Contorno**. 63 p. Dissertação (Mestrado) — Unicamp, Campinas (SP), 2008.

Cruse, T. A.; Swedlow, J. L. **Interactive program for analysis and design problems in advanced composites**. Ohio, 1971. Technical Report AFML-TR-71-268.

Deb, A.; D P Henry, J. Alternate bem formulations for 2- and 3-d anisotropic thermoelasticity. **International Journal of Solids and Structures**, v. 27, p. 1721–1738, 1991.

Dumir, P. C.; Mehta, A. K. Boundary element solution for elastic orthotropic half-space problems. **Computers & Structures**, v. 26, p. 431–438, 1987.

Flyer, N.; Barnett, G. A.; Wicker, L. Enhancing finite differences with radial basis functions: Experiments on the navier-stokes equations. **Journal of Computational Physics**, v. 316, p. 39–62, 2016b.

Flyer, N.; Fornberg, B.; Bayona, V.; Barnett, G. A. On the role of polynomials in rbf-fd approximations: I. interpolation and accuracy. **Journal of Computational Physics**, v. 321, p. 21–38, 2016a.

Galvis, A. F.; Prada, D. M.; Moura, L. S.; Zavaglia, C.; Foster, J. M.; Sollero, P.; Wrobel, L. C. Besle: Boundary element software for 3d linear elasticity. **Computer Physics Communications**, v. 265, p. 108009, 2021.

Gao, X.-W. The radial integration method for evaluation of domain integrals with boundary-only discretization. **Engineering Analysis with Boundary Elements**, v. 26, p. 905–916, 2002.

Gao, X.-W. Boundary element analysis in thermoelasticity with and without internal cells. **International Journal for Numerical Methods in Engineering**, v. 57, p. 975–990, 2003.

Gaul, L.; Kögl, M.; Wagner, M. **Boundary Element Methods for Engineers and Scientists**: An introductory course with advanced topics. New York: Springer, 2003.

Goldberg, M. A.; Chen, C. S.; Bowman, H. Some recent results and proposals for the use of radial basis functions in the bem. **Engineering Analysis of Boundary Elements**, v. 23, p. 285–296, 1999.

Goldberg, M. A.; Chen, C. S.; Bowman, H.; Power, H. Some comments on the use of radial basis functions in the dual reciprocity method. **Computational Mechanics**, v. 21, p. 141–148, 1998.

Goldberg, M. A.; Chen, C. S.; Karur, S. R. Improved multiquadric approximation for partial differential equations. **Engineering Analysis of Boundary Elements**, v. 18, p. 9–17, 1996.

Green, A. E. A note on stress systems in aelotropic materials. **Philosophical Magazine**, v. 31, p. 416–418, 1943.

Green, A. E.; Zerna, W. **Theoretical Elasticity**. 2. ed. Oxford: Clarendon Press, 1968.

D P Henry, J.; Banerjee, P. K. A new boundary element formulation for two- and three-dimensional thermoelasticity using particular integrals. **International Journal for Numerical Methods in Engineering**, v. 26, p. 2061–2077, 1988.

Kane, J. H. **Boundary Element Analysis in Engineering Continuum Mechanics**. New Jersey: Prentice Hall, 1994.

Karur, S. R.; Ramachandran, P. A. Radial basis functions approximation in the dual reciprocity method. **Mathematical and Computer Modelling**, v. 20, p. 59–70, 1994.

Katsikadelis, J. T. **Boundary Elements**: Theory and applications. Oxford: Elsevier, 2002.

Kögl, M.; Gaul, L. A boundary element method for anisotropic coupled thermoelasticity. **Archive of Applied Mechanics**, v. 73, p. 377–398, 2003.

Lee, V.-G. Explicit expression of derivatives of elastic green's functions for general anisotropic materials. **Mechanics Research Communications**, v. 30, n. 3, p. 241–249, 2003.

Lee, V.-G. Derivatives of the three-dimensional green's functions for anisotropic materials. **International Journal of Solids and Structures**, v. 46, n. 18-19, p. 3471–3479, 2009.

Lekhnitskii, S. G. **Theory of Elasticity of an Anisotropic Elastic Body**. San Francisco: Holden-Day, 1963.

Lifshitz, I. M.; Rozenzweig, L. N. Construction of the green tensor for the fundamental equation of elasticity theory in the case of unbounded elastically anisotropic medium. **Zh. Eksp. Teor. Fiz.**, v. 17, p. 783–791, 1947.

Liu, Y. **Fast Multipole Boundary Element Method**: Theory and applications in engineering. Cambridge: Cambridge University Press, 2009.

Loeffler, C. F.; L. Cruz Átila; Bulcão, A. Direct use of radial basis interpolation functions for modelling source terms with the boundary element method. **Engineering Analysis with Boundary Elements**, v. 50, p. 97–108, 2015.

Loloi, M. Boundary integral equation solution of three-dimensional elastostatic prooblems in transversely isotropic solids using closed-form displacement fundamental solutions. **International Journal of Numerical Methods in Engineering**, v. 48, p. 823–843, 2000.

Mai-Duy, N.; Tran-Cong, T. Approximation of function and its derivatives using radial basis functions networks. **Applied Mathematical Modelling**, v. 27, p. 197–220, 2003.

Marczak, R. J.; Denda, M. New derivations of the fundamental solution for heat conduction problems in three-dimensional general anisotropic media. **International Journal of Heat and Mass Transfer**, v. 54, p. 3605–3612, 2011.

Matsumoto, T.; Guzik, A.; Tanaka, M. A boundary element method for analysis of thermoelastic deformations in materials with temperature dependent properties. **International Journal for Numerical Methods in Engineering**, v. 64, p. 1432–1458, 2005.

Noritomi, P. Y. **Desenvolvimento de uma metodologia para análise de bioengenharia em ossos compactos com remodelagem superficial pelo Método dos Elementos de Contorno 3D em meios transversalmente isotrópicos**. Tese (PhD Thesis) — Unicamp, Campinas, 2005.

Pan, E.; Amadei, B. A 3-d boundary element formulation of anisotropic elasticity with gravity. **Applied Mathematical Modelling**, v. 20, p. 114–120, 1995.

Pan, Y. C.; Chou, T. W. Point force solutio for an infinite transversely isotropic solid. **Journal of Applied Mechanics**, v. 43, p. 608–612, 1976.

Partridge, P. W.; Brebbia, C.; Wrobel, L. **The Dual Reciprocity Boundary Element Method**. Southampton: Computational Mechanics Publications, 1992.

Phan, A. V.; Gray, L. J.; Kaplan, T. On the residue calculus of evaluation of the 3-d anisotropic elastic green's function. **Communications in Numerical Methods in Engineering**, v. 20, p. 335–341, 2004.

Pooladi, F.; Larsson, E. Stabilized interpolation using radial basis functions augmented with selected readial polynomials. **Journal of Computational and Applied Mathematics**, v. 437, p. 115482, 2023.

Ramos, V. E. d. S. **Aplicação Recursiva do Método dos Elementos de Contorno em Problemas de Poisson**. 61 p. Dissertação (Mestrado) — Universidade Federal do Espírito Santo, Vitória (ES), 2015.

Rizzo, F. J.; Shippy, D. J. A method for stress determination in plane anisotropic elastic bodies. **Journal of Composite Materials**, v. 4, p. 36–61, 1970.

Rizzo, F. J.; Shippy, D. J. An advanced boundary integral equation method for three-dimensional thermoelasticity. **International Journal for Numerical Methods in Engineering**, v. 11, p. 1753–1768, 1977.

Rodríguez, A. F. G. **Multiscale Modeling of Dynamic Failure in 3D Polycrystalline Materials using BEM and MD**. Tese (PhD Thesis) — Unicamp, Campinas, 2019.

Sales, M. A.; Gray, L. J. Evaluation of the anisotropic green's function and its derivatives. **Computers & Structures**, v. 69, p. 247–254, 1998.

Schclar, N. A.; Partridge, P. W. 3d anisotropic elasticity with bem using isotropic fundamental solution. **Engineering Analysis with Boundary Elements**, v. 11, p. 137–144, 1993.

Shiah, Y.; Tan, C.; Lee, R. Internal point solutions for displacements and stresses in 3d anisotropic elastic solids using the boundary element method. **Computer Modeling in Engineering and Sciences**, v. 69, n. 2, p. 167–197, 2010.

Shiah, Y. C.; Hwang, P.; Yang, R. Heat conduction in multiply adjoined anisotropic media with embedded point heat sources. **Journal of Heat Transfer**, v. 128, p. 207–214, 2006.

Shiah, Y. C.; Tan, C. L. Bem treatment of two-dimensional anisotropic field problems by direct domain mapping. **Engineering Analysis with Boundary Elements**, v. 20, p. 347–351, 1997.

Shiah, Y. C.; Tan, C. L. Bem treatment of three-dimensional anisotropic field problems by direct domain mapping. **Engineering Analysis with Boundary Elements**, v. 28, p. 43–52, 2004.

Shiah, Y. C.; Tan, C. L. Boundary element method for thermoelastic analysis of three-dimensional transversely isotropic solids. **International Journal of Solids and Structures**, v. 49, p. 2924–2933, 2012.

Shiah, Y. C.; Tan, C. L. The boundary integral equation for 3d general anisotropic thermoelasticity. **Computer Modelling in Engineering & Sciences**, v. 102, p. 425–447, 2014.

Shiah, Y. C.; Tan, C. L. Boundary element analysis of interior thermoelasitc stresses in three-dimensional generally anisotropic bodies. **Journal of Mechanics**, v. 32, p. 725–735, 2016.

Shiah, Y. C.; Tan, C. L. Thermoelastic analysis of 3d generally anisotropic bodies by the boundary element method. **European Journal of Computational Mechanics**, v. 25, p. 91–108, 2016.

Shiah, Y. C.; Tan, C. L.; Lee, V. G. Evaluation of explicit-form fundamental solutions for displacements and stresses in 3d anisotropic elastic solids. **Computer Modeling in Engineeging & Sciences**, v. 34, p. 205–226, 2008.

Shiah, Y. C.; Tan, C. L.; Wang, C. Y. Efficient computation of the green's function and its derivatives for three-dimensional anisotropic elasticity in bem analysis. **Engineering Analysis with Boundary Elements**, v. 36, p. 1746–1755, 2012.

Sollero, P.; Aliabadi, M. H. Fracture mechanics analysis of anisotropic plates by the boundary element method. **International Journal of Fracture**, v. 64, p. 269–284, 1993.

Souza, C. A. O. de. **Modelagem Numérica por elementos de Contorno 3D de Juntas Coladas em estruturas Aeronáuticas de Material Compósito**. Tese (PhD Thesis) — Unicamp, Campinas, 2009.

Tan, C. L.; Shiah, Y. C.; Lin, C. W. Stress analysis of 3d generally anisotropic elastic solids using the boundary element method. **Computer Modeling in Engineeging & Sciences**, v. 41, p. 195–214, 2009.

Tan, C. L.; Shiah, Y. C.; Wang, C. Boundary element elastic stress analysis of 3d generally anisotropic solids using fundamental solutions based on fourier series. **International Journal of Solids and Structures**, v. 50, n. 16-17, p. 2701–2711, 2013.

Ting, T. C. T.; Lee, V.-G. The three-dimensional elastostatic green's function for general anisotropic linear elastic solids. **The Quarterly Journal of Mechanics and Applied Mathematics**, v. 50, n. 3, p. 407–426, 1997.

Tolstykh, A. I.; Shirobokov, D. A. On using radial basis functions in a "finite difference mode" with applications to elasticity problems. **International Journal of Solids and Structures**, v. 50, p. 2701–2711, 2003.

Tonon, F.; Pan, E.; Amadei, B. Green's functions and boundary element method formulation for 3d anisotropic media. **Computers & Structures**, v. 79, p. 469–482, 2001.

Távara, L.; Ortiz, J. E.; Mantic, V.; París, F. Unique real-variable expressions of displacement and traction fundamental solutions covering all transversely isotropic elastic materials for 3d bem. **International Journal for Numerical Methods in Engineering**, v. 74, p. 776–798, 2007.

Ubero-Martínez, I.; Rodríguez-Tembleque, L.; Cifuentes-Rodríguez, J.; Vallepuga-Espinosa, J. 3d thermoelastic solids under non-linear interface thermal and orthotropic frictional contact conditions. **International Journal for Numerical Methods in Engineering**, Hoboken, USA, v. 123, n. 11, p. 2631–2659, 2022.

Vogel, S. M.; Rizzo, F. J. An integral equation formulation of three dimensional anisotropic elastostatic boundary value problems. **Journal of Elasticity**, v. 3, p. 203–216, 1973.

Wang, C. Y. Elastic fields produced by a point source in solids of general anisotropy. **Journal of Engineering Mathematics**, v. 32, p. 41–52, 1997.

Wang, C. Y.; Denda, M. 3d bem for general anisotropic elasticity. **International Journal of Solids and Structures**, v. 44, p. 7073–7091, 2007.

Wilson, R. B.; Cruse, T. A. Efficient implementation of anisotropic three dimensional boundary-integral equation stress analysis. **International Journal for Numerical Methods in Engineering**, v. 12, p. 1383–1397, 1978.